Experimental Techniques and Image Reconstruction for Magnetic Resonance Imaging with Inhomogeneous Fields

A THESIS
SUBMITTED TO THE FACULTY OF THE GRADUATE SCHOOL
OF THE UNIVERSITY OF MINNESOTA
BY

Michael Fritz Mullen

IN PARTIAL FULFILLMENT OF THE REQUIREMENTS
FOR THE DEGREE OF
DOCTOR OF PHILOSOPHY

Advisor: Michael Garwood
Co-advisor: Geoffrey Ghose

August 2019

Acknowledgements

Having had no prior experience in magnetic resonance, medical imaging, or anything remotely clinical, I met with Dr. Michael Garwood in the summer of 2015 to discuss joining his lab to develop novel magnetic resonance imaging (MRI) technology. Since then, Dr. Garwood has instilled in me a profound excitement and interest in the field, its applications, and clinical impact. Through his example, I have grown substantially as a scientist, greatly expanded my scientific understanding, while continuing to become more adept at scientific inquiry in general. There are not enough thanks to express my gratitude to Dr. Garwood for his mentorship during my time as a Ph. D. student in his lab.

The research environment at the Center for Magnetic Resonance Research (CMRR) at the University of Minnesota has been incredible during my stay here. I would like to thank Drs. Hattie Ring, Jinjin Zhang, and (then-graduate students) Drs. Bradley Weegman, Samual Einstein, and Albert Jang for welcoming me into the group upon my arrival. Their guidance and patience during my formative time in the lab was invaluable to my introduction to magnetic resonance. I am grateful to Dr. Ring for broadening my perspectives regarding applications of MRI and for her guidance on our quantitative T_2 mapping work, together with Dr. Garwood.

I thank Drs. Steen Moeller and Jarvis Haupt for taking the time to enlighten me with many of the intricasies of model-based image reconstruction and optimization. I would also like to thank Drs. Haupt, Alex Kamenev, John Broadhurst, and Geoffrey Ghose for serving on my final exam committee, and again to Dr. Ghose for serving as my coadvisor.

I am thankful to Drs. Robin deGraaf and Christoph Juchem for introducing me to sequence programming on the 4T Varian system at the CMRR during a visit here, and to Drs. Djaudat Idiyatullin and Naoharu Kobayashi for their continued guidance in this area as questions arose. I am further indebted to Drs. Idiyatullin and Kobayashi for providing their expertise regarding sequence and pulse design, and to Dr. Kobayashi for his assistance in understanding segmented radiofrequency pulses.

As a research system, the 4T scanner has idiosyncrasies not common among MRI scanners. I am grateful to Drs. Gregor Adriany and Lance DelaBarre for their

technical assistance in resolving many issues which arose due to this. My research would not have progressed as smoothly as it did without their knowledge and patience.

Two years of my research were funded by the T32 Neuroimaging Traineeship program (T32 EB008389) at the University of Minnesota, for which funding was secured by Dr. Bin He and continued by Dr. Wei Chen. I thank them for securing the T32 grant at the University of Minnesota and for accepting me into the program.

Finally, I would like to thank my parents, Lisa and Stephen, for their love, support, and confidence in my ability to pursue and accomplish my goals. There are countless other ways in which they helped me reach this stage of my life, but there simply is not sufficient room to describe them all here. I'd like to thank my siblings for their support, as well. Finally, I want to thank my wife, Megan, for her unconditional love during my pursuit of a Ph. D.

In loving memory of my father, Steve Mullen.

Abstract

Magnetic resonance imaging is quite sensitive to experimental imperfections, necessitating extremely expensive electrical infrastructure and design requirements to permit high-quality experiments to be performed. By relaxing the sensitivity to imperfection, the entire system can be made less expensive and more accessible by shrinking the magnet generating the polarizing field. Decreasing the magnet size relative to the bore increases the polarizing field inhomogeneity. Moreover, current progress in MRI at ultra-high field ($\geq$ 7T) is pushing the limits of conventional MRI methods, as field inhomogeneity increases with field strength. Hence, while many of the methods herein were developed with a small magnet in mind, they also apply at ultra-high field. The appeal of ultra-high field is increased detection sensitivity such that ever-smaller structures may be imaged in animals and humans.

The primary goal of this work is to extend the current ability of magnetic resonance imaging to tolerate a large degree of spatial variation in both the transmit and polarizing fields involved. A novel method of decreasing radiofrequency pulse duration for multidimensional pulses is presented, rendering them more robust to field inhomogeneity. Furthermore, this method is leveraged to accelerate data acquisition. A new imaging sequence for quantitative determination of transverse relaxation rates is presented, which tolerates large variations in both the transmit and polarizing magnetic fields, as is often found when imaging with iron-oxide nanoparticles and/or at ultra-high field. Finally, a computationally efficient approach for spatiotemporally-encoded image reconstruction is presented, which is inherently robust to field inhomogeneity.

Contents

List of Tables

List of Figures

Chapter 1

Introduction

1.1 Motivation

The theme of this work is to extend the current ability of magnetic resonance imaging to tolerate a larger degree of spatial variation in both the transmit and polarizing fields involved. Such a goal is desirable due to the current high cost of the hardware necessary to match the correspondingly stringent constraints placed on the level of homogeneity necessary for current imaging methods. For example, modern MRI systems have on the order of 1 - 2 parts per million (ppm) field variation, but can cost upward of millions of US dollars. The high cost results as the imaging volume, large enough to hold a human, is made significantly smaller than the magnet itself. In turn, the electrical infrastructure, length of superconductor, and volume of helium required to operate such a system is enormous. Relaxing the homogeneity constraints can deflate this value by permitting the use of a small, portable magnet, where the imaging volume is comparable in scale to the magnet itself.

Despite its hefty price, MRI systems have several advantages over other medical imaging platforms. Foremost, there is no ionizing radiation involved, as is the case with Computed Tomography (CT) or Positron Emission Tomography (PET). Assuming appropriate safety protocols are followed to keep magnetic objects away from the system, this renders MRI significantly safer than CT or PET. While the repeated radiofrequency pulses used can cause tissue heating in patients, the power used is closely

monitored and kept well below damaging levels. In fast imaging sequence, rapidly switching gradients can cause peripheral nerve stimulation (PNS). While not dangerous, PNS is generally uncomfortable for the patient and can cause motion, inducing artifacts in the reconstructed images. On the contrary, any exposure in CT and PET is damaging, as they employ ionizing radiation. Compared to ultrasound, it has a much higher spatial resolution. By simply varying timing and power parameters in MRI, a wealth of information can be obtained, quickly illuminating health concerns. Such a large variety of information is not available with PET, CT, or ultrasound.

Without writing an entire treatise on MRI methods, as would be necessary for a full coverage of the subject matter, this work attempts to cover the relevant background for a working understanding of the content. The emphasis is on radiofrequency pulse design, imaging sequence design, applications, with some additional work on image reconstruction routines. However, it is in no way exhaustive, and many important aspects of magnetic resonance (MR) have been omitted. Most notable among the topics which deserve more attention is echo formation and coherence, for which the reader is referred to [1]. Relaxation mechanisms are largely ignored, for which the curious reader is encouraged to reference [2], [3]. Knowledge of Fourier transforms is assumed.

Furthermore, as the focus of this thesis is on imaging, a quantum mechanical consideration of the work at hand is not strictly necessary. Therefore, the background section on quantum mechanics is merely a brief argument against using quantum mechanics for imaging studies. For the applications of this work, quantum mechanics is *almost* entirely unnecessary.

1.2 History of NMR and MRI

At the most basic level, proton nuclear magnetic resonance (NMR) is a two energy level system, where transitions between levels are induced by means of a radiofrequency (RF) pulse. The energy difference is established through the Zeeman interaction - that is, the interaction between the magnetic moment of the nucleus and an external magnetic field. Rabi et al. [4] performed some of the earliest experiments examining this interaction, noting RF frequency-dependent energy absorption. How-

ever, it wasn't until 1946 that two independent groups, led by Bloch [5], [6], [7] and Purcell [8], respectively, that magnetic resonance was directly detected following the application of a RF field.

Prior to modern instrumentation, the most straightforward experimental approach for detecting NMR spectra was to apply a constant frequency RF field while simultaneously sweeping the polarizing field. This method, known as *continuous wave NMR*, is extremely slow and insensitive, directly detecting the spectra as a function of resonance frequency. In 1966, Ernst and Anderson [9] introduced *pulsed NMR*, exploiting the conjugate relationship between the time-domain response of the spin system and the frequency-domain response. As its name implies, pulsed NMR utilizes short, pulsed RF fields in the presence of a static polarizing field. The time-domain response is measured experimentally and Fourier transformed to obtain the frequency-domain spectra. Thus, the entire spectrum can be obtained following a small number of RF pulses, greatly enhancing the speed and sensitivity of NMR.

The first recognition of the ability to image using magnetic resonance was by Lauterbur [10], [11]. Therein, it was demonstrated that a RF pulse in the presence of a linear field gradient permitted the ability to encode spatial information, as well as subsequent encoding gradients, marking the birth of MRI. Notably, Lauterbur discovered the degree of localization was independent of the RF frequency. In other words, the spatial resolution of the method is independent of the RF wavelength. The disconnect between resolution and wavelength stands in stark contrast to the case in optics, where the resolution is directly governed by the illuminating wavelength [12]. Shortly thereafter, Hoult [13] showed the necessity to refocus spins prior to signal detection in order to obtain a high-quality image. Hoult's approach is now called an *echo*. The following chapter presents the mathematical and physical background of these advances, as well as the developments since which are necessary to understand the work presented herein.

Chapter 2

Background

2.1 Classical Description of Magnetic Resonance

2.1.1 Qualitative Overview

This subsection is dedicated to a general classical overview of magnetic resonance prior to delving into the quantitative aspects. The motivating factor for doing this is many aspects of magnetic resonance overlap. It is challenging to discuss any single facet without having previously covered others at least in passing.

To begin, a paramagnetic object is placed in a large polarizing magnetic field, inducing a magnetic moment in the object. This magnetic momentic is static and aligned with the polarizing field. To make the magnetic moment detectable, it must be tipped away from the polarizing field. This is done by applying a *radiofrequency pulse* with a resonant circuit called a *transmitter* or *RF coil*. When not aligned with the magnetic field, the moment experiences a torque causing it to precess around the field, while interactions among spins cause the moment to slowly return to alignment with the magnetic field. This process is called *relaxation*. A precessing magnetic moment gives rise to an oscillating magnetic field, which is easily detected inductively (by Faraday's law [14]) by a resonant circuit tuned to the frequency of precession, hereafter referred to as a receiver. As is often the case, the receiver and transmitter are the same circuit, and both are called RF coils.

The magnetic moment is the sum over many smaller moments within the object,

where the smaller moments are to be resolved with respective to their positions in space. Therefore, the quantity of interest is the *magnetization*, or the amount of magnetic moment per unit volume. As mentioned above, a RF pulse establishes magnetization which precesses around the polarizing field. The magnetization is a three-dimensional vector, with one component parallel to the polarizing field, and two other components which are both orthogonal to the polarizing field. The latter two, taken together, are called the *transverse magnetization*, which is the detected quantity in MRI.

The magnitude of the transverse magnetization is determined by how far the magnetization was tipped away from the polarizing field. The angle between the magnetization and the polarizing field is called the *flip angle*. Magnetization which has been flipped away from the polarizing field is said to have been *excited*. To encode information in excited magnetization, *linear field gradients*, hereafter gradients, are applied, which causes the frequency of precession about B_0 to vary linearly as a function of position. The different frequencies are resolved computationally using a Fourier transform with the appropriate number of encoded dimensions.

2.1.2 Equations of Motion

It has been shown [14] that the torque $\vec{\tau}$ on a magnetic dipole $\vec{m}$ in a uniform magnetic field $\vec{B}$ is given by

$$\vec{\tau} = \vec{m} \times \vec{B}. \tag{2.1}$$

Treating the proton as a uniformly charged, rotating sphere, the magnetic dipole moment is given by

$$\vec{m} = \frac{1}{2} \int_{V'} \vec{x}' \times \vec{J}(\vec{x}') d^3x', \tag{2.2}$$

where the primed coordinates indicate integration over the extent of the volume V' and $\vec{J}$ is the current density. For a small volume dV', this can be rewritten in differential form as

$$d\vec{m} = \frac{1}{2} \vec{x}' \times \vec{J} dV'. \tag{2.3}$$

Denoting the charge of the proton by e, its radius by R, and its rotational frequency by ω, consider the infinitesimal charge dq and its contribution $d\vec{m}$ to the total magnetic moment of the sphere. The charge dq can be written in spherical coordinates as,

$$dq = \rho dV' \tag{2.4}$$

$$\rho = e/(\frac{4}{3}\pi R^3) \qquad \text{(charge density)} \tag{2.5}$$

$$dV = r^2 \sin(\theta) dr d\theta d\phi \qquad \text{(volume element).} \tag{2.6}$$

For a moving charge, the current density is simply

$$\begin{aligned} \vec{J} &= \rho\vec{v} \\ &= \rho\vec{\omega} \times \vec{x}', \end{aligned} \tag{2.7}$$

where $\vec{\omega} = \omega\hat{\omega}$ is the angular velocity of the rotating sphere. For simplicity and without loss of generality, the direction of the angular velocity is chosen to be $\hat{z}$. From Eq. 2.3,

$$d\vec{m} = \frac{\rho}{2}\vec{x}' \times (\vec{\omega} \times \vec{x}')dV'. \tag{2.8}$$

Using the vector triple product,

$$\vec{a} \times \vec{b} \times \vec{c} = (\vec{a} \cdot \vec{c})\vec{b} - (\vec{a} \cdot \vec{b})\vec{c}, \tag{2.9}$$

this gives

$$d\vec{m} = \frac{\rho}{2} r^2 \vec{\omega} - (\vec{x}' \cdot \vec{\omega})\vec{x}' dV'. \tag{2.10}$$

For a charge element at radius r, polar angle θ, and azimuthal angle ϕ, the position $\vec{x}'$ is

$$\vec{x}' = r\sin\theta\cos\phi\hat{x} + r\sin\theta\sin\phi\hat{y} + r\cos\theta\hat{z}, \tag{2.11}$$

such that

$$(\vec{x}' \cdot \vec{\omega})\vec{x}' = r^2\omega\cos\theta(\sin\theta\cos\phi\hat{x} + \sin\theta\sin\phi\hat{y} + \cos\theta\hat{z}). \tag{2.12}$$

When integrating $d\vec{m}$ over the volume V', the integrals over ϕ from 0 to 2π for the terms $\hat{x}$ and $\hat{y}$ integrate to 0. This is due to to the periodicity of $\sin\phi$ and $\cos\phi$. Hence, after integrating over ϕ,

$$\begin{aligned}\vec{m} &= \pi\rho\omega \int_0^R \int_0^\pi r^4(1-\cos^2\theta)\hat{z}\sin\theta dr d\theta \\ &= \frac{e}{5}\omega R^2\hat{z}, \end{aligned} \tag{2.13}$$

where the definition of ρ was substituted. The moment of inertia, I, of a solid sphere of mass m_p and radius R is $I = \frac{2}{5}m_p R^2$ [15]. Rewriting the dipole moment in terms of the moment of inertia,

$$\begin{aligned}\vec{m} &= \frac{e}{2m_p} I\omega\hat{z} \\ &= \frac{e}{2m_p}\vec{L} \end{aligned} \tag{2.14}$$

$$\vec{L} = I\omega\hat{z}. \tag{2.15}$$

Thus, the magnetic moment is seen to be directly proportional to the spin angular momentum $\vec{L}$ of the classical proton, with proportionality constant

$$\gamma = \frac{e}{2m_p}, \tag{2.16}$$

where γ is commonly called the *gyromagnetic ratio*. The classical value expected from Eq. 2.16 does not exactly agree with the measured value, since the proton is not a classical particle. The discrepency is captured in the *g-factor*, such that

$$\gamma = g\frac{e}{2m_p} \tag{2.17}$$

which must be described quantum mechanically. The g-factor here is not to be confused with the like-named g-factor in Chapter 4. The value of $\frac{\gamma}{2\pi}$ for a proton is approximately 42.58 $\frac{MHz}{T}$.

Returning to Eq. 2.1, torque is, by definition, the rate of change of angular

momentum. Hence,

$$\vec{\tau} = \frac{d\vec{L}}{dt}. \tag{2.18}$$

Substituting $\vec{L} = \frac{\vec{m}}{\gamma}$ into Eq. 2.18 and that result into Eq. 2.1,

$$\begin{aligned} \frac{d\vec{m}}{dt} &= \gamma(\vec{m} \times \vec{B}) \\ &= \gamma|B|(\vec{m} \times \hat{B}) \end{aligned} \tag{2.19}$$

with $\hat{B} = \vec{B}/|\vec{B}|$ a unit vector pointing in the direction of $\vec{B}$. Thus, Eq. 2.19 are the *Bloch equations*, predicting *clockwise* precession of the dipole about $\hat{B}$. The angular frequency of precession about the field is given by

$$\omega_L = \gamma B. \tag{2.20}$$

If the field in Eq. 2.19 is the polarizing field, the angular frequency is called the *Larmor frequency*,

$$\omega_L = \gamma B_0. \tag{2.21}$$

As currently written, the Bloch equations do not fully predict the outcome of experiments. This is due to the neglect thus far of relaxation, the return to thermal equilibrium following an excitation out of equilibrium. Realizing this shortcoming, Bloch proposed [6] to include exponential relaxation with two different characteristic times. The first, T_1, denotes relaxation along the polarizing magnetic field, while the other, T_2, denotes relaxation orthogonal to the polarizing field. The extended equations then read

$$\frac{d}{dt}\vec{m}_x = \gamma(\vec{m} \times \vec{B})_x - \frac{1}{T_2}m_x \tag{2.22}$$

$$\frac{d}{dt}\vec{m}_y = \gamma(\vec{m} \times \vec{B})_y - \frac{1}{T_2}m_y \tag{2.23}$$

$$\frac{d}{dt}\vec{m}_z = \gamma(\vec{m} \times \vec{B})_z - \frac{1}{T_1}(m_z - M_0). \tag{2.24}$$

A large polarizing magnetic field, B_0, generates longitudinal magnetization M_0, the form of which must be derived quantum mechanically but is simply presented here as

$$M_0 = (\gamma\hbar)^2 \frac{NB_0}{4k_B T}. \tag{2.25}$$

As mentioned at the start of the chapter, the quantity of interest is the magnetization, or the dipole moment per unit volume. Thus, defining

$$\vec{M} = \frac{1}{V} \sum_V \vec{m} \tag{2.26}$$

as the magnetization, it is trivially seen to also satisfy the Bloch equations by direct summation of Eq. 2.22 over an arbitrary volume, V. When the magnetization is displaced from its equilibrium value by a RF pulse (Section 2.2), there is a component of magnetization transverse to B_0, $M_{xy} = M_x + iM_y$, which precesses around B_0 at the Larmor frequency. The value M_{xy} is the transverse magnetization. The associated oscillating magnetic field can be detected with a nearby RF coil tuned to the Larmor frequency. The consequences of this are covered in Section 2.3.

2.1.3 The Rotating Frame

The above equations simply describe the evolution of magnetization in a magnetic field, and do not, as presented, illuminate the magnetic resonance phenomenon. Resonance is, generally, the instance where a large departure from equilibrium is obtained with only a small-amplitude driving field. For magnetic resonance specifically, an applied RF field oscillating at frequency ω is applied, with either linear or circular polarization, orthogonal to the field B_0. For now, a linearly polarized RF field will be considered. Hereafter, RF fields will be denoted by B_1. Hence in the lab frame,

$$\vec{B}_1 = B_1 \cos(\omega t)\hat{x} \tag{2.27}$$

with t being time.

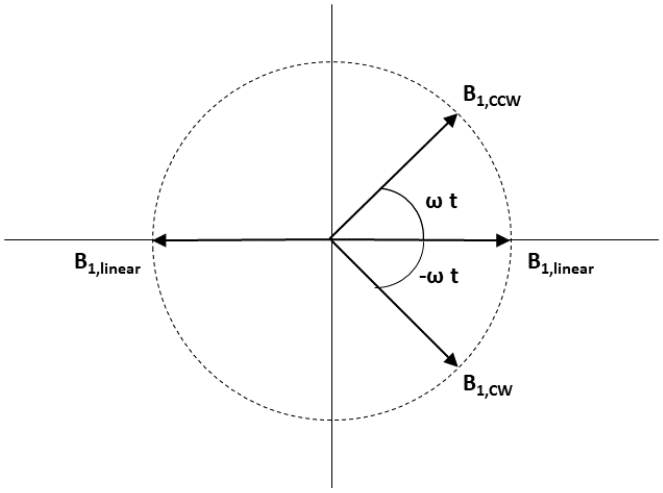

Fig. 2.1. Depiction of the decomposition of a linearly polarized field into two counter-rotating RF fields at the same frequency. CW indicates clockwise rotation, while CCW indicates counter-clockwise rotation.

Rewriting this as the superposition of two counter-rotating magnetic fields (Fig. 2.1), both at frequency ω,

$$\vec{B}_1 = \frac{B_1}{2}\Big(\big(\cos(\omega t)\,\hat{x} + \sin(\omega t)\,\hat{y}\big) + \big(\cos(\omega t)\,\hat{x} - \sin(\omega t)\,\hat{y}\big)\Big). \tag{2.28}$$

Changing frames of reference to a *rotating frame*, which rotates about the z-axis with the clockwise component of B_1 in Eq. 2.28,

$$\vec{B}_1 = \frac{B_1}{2}\Big(\big(1 + \cos(2\omega t)\big)\hat{x'} + \sin(2\omega t)\hat{y'}\Big). \tag{2.29}$$

The angular velocity of the rotating frame is

$$\vec{\Omega} = -\omega\hat{z}. \tag{2.30}$$

When changing from a stationary frame to a rotating frame of reference with angular velocity $\vec{\Omega}$, the apparent time-dependence of physical quantities is altered. The change

in time-dependence for a generic vector $\vec{A}(t)$ is given by [15]

$$(\frac{d\vec{A}}{dt})_{rot} = (\frac{d\vec{A}}{dt})_{stationary} + \vec{A} \times \vec{\Omega}. \tag{2.31}$$

Replacing $\vec{A}$ by the magnetization $\vec{M}$ in the Bloch equations, ignoring relaxation,

$$\begin{aligned}(\frac{d\vec{M}}{dt})_{rot} &= (\frac{d\vec{M}}{dt})_{stationary} + \vec{M} \times \vec{\Omega} \\ &= \gamma\vec{M} \times \vec{B} + \vec{M} \times \vec{\Omega} \\ &= \gamma\vec{M} \times (\vec{B} + \frac{\vec{\Omega}}{\gamma}).\end{aligned} \tag{2.32}$$

Thus, in the presence of both B_1 and B_0, this becomes

$$(\frac{d\vec{M}}{dt})_{rot} = \gamma\vec{M} \times \frac{B_1}{2}\Big(\big(1 + \cos(2\omega t)\big)\hat{x'} + \sin(2\omega t)\hat{y'} + \big(B_0 - \frac{\omega}{\gamma}\big)\hat{z}\Big). \tag{2.33}$$

If the frequency ω of the RF field is chosen to be the Larmor frequency (Eq. (2.21)), the term along $\hat{z}$ cancels. Such a field is said to be *on-resonance*. This is because the $\vec{\Omega}$ term acts as a *fictitious field*, affecting magnetization dynamics in the rotating frame, but which does not exist in the lab frame. Additionally, the time-dependent terms rapidly average to 0, since they are oscillating at twice the Larmor frequency in the rotating frame, which is typically several hundred MHz. This finally leaves

$$(\frac{d\vec{M}}{dt})_{rot} = \gamma\vec{M} \times \frac{B_1}{2}\hat{x'}. \tag{2.34}$$

Thus, in the rotating frame, magnetization precesses about the applied field only, and the effects of the polarizing field are masked, despite its large relative amplitude. In the laboratory frame, the magnetization rotates away from the polarizing field while simultaneously precessing around it. For this reason, all further analysis assumes the rotating frame due to the simplified mathematical description of the dynamics. For sake of comparison, the relative amplitude of B_1 to B_0 is $\frac{B_1}{B_0} \approx 10^{-5}$. For *off-resonance*

frequencies, where $\omega \neq \omega_L$,

$$(\frac{d\vec{M}}{dt})_{rot} = \gamma\vec{M} \times \left(\frac{B_1}{2}\hat{x'} + \frac{\Delta\omega}{\gamma}\hat{z}\right) \tag{2.35}$$

$$\Delta\omega = (\omega_L - \omega). \tag{2.36}$$

In Eq. 2.34, the amplitude of the RF field affecting dynamics in the rotating frame is half the amplitude of the applied field. This stems from the decomposition of the linear field into two counter-rotating fields, one of which is on-resonance, and one of which is $2\omega_L$ off-resonance. Only the field rotating clockwise at the Larmor frequency significantly affects the magnetization motion, so half the amplitude is lost to the other rotating component of the field. However, if the applied field is already circularly polarized, no such lost is incurred. Generating a circularly polarized field can be performed directly by using a quadrature transmit coil.

Above, relaxation was ignored. In biological specimens, the relaxation times T_1 and T_2 are at least several tens of milliseconds to seconds, while RF pulse durations are usually not longer than about 10 ms. Thus, relaxation is substantially longer than RF pulses and may almost always be safely neglected when considering the effects of pulses.

2.1.4 Off-Resonance and Shimming

The off-resonance field in Eq. 2.35 can either arise for several reasons: microscopic field variation due to susceptibility effects, macroscopic field variation, or the RF pulse being transmitted with a finite offset from the Larmor frequency, to name a few. However, macroscopic field variations are generally mitigated by using several additional *shim* coils, which are resistive electromagnets used to homogenize the B_0 field. The current through these coils can be set either manually or automatically, the process of which is called *shimming*.

Despite the ability to shim, there will always be some residual field inhomogene-

ity. In the absence of a RF pulse, Eq. 2.35 simply becomes

$$(\frac{d\vec{M}}{dt})_{rot} = \gamma\vec{M} \times \Delta\omega\hat{z}. \tag{2.37}$$

Transverse magnetization at different off-resonance frequencies then precess about $B_0+\Delta\omega$ at different frequencies. This frequency dispersion causes *dephasing*, whereby the transverse components of magnetization at different spatial locations or within a single encoded voxel, with various $\Delta\omega$, come out of alignment. Dephasing causes a decrease in the net transverse magnetization, in turn decreasing the available detectable signal.

2.2 Details of Radiofrequency Pulses

2.2.1 Amplitude-Modulated Pulses

In the previous section, it was seen that in the rotating frame, on-resonance magnetization rotates around the B_1 field, which had a fixed amplitude in Eq. 2.34. Such a *hard-pulse* need not be the case, and the B_1 amplitude can be modulated in time, such that $B_1 \equiv B_1(t)$. A time-dependent B_1 does not change the analysis thus far, provided the rate of amplitude modulation is slow compared to the Larmor frequency. The total angle precessed about B_1 in the rotating frame, the flip angle, is then

$$\theta = \gamma \int_0^{T_P} B_1(t)dt \tag{2.38}$$

for an RF pulse of duration T_P. If the flip angle is 180°, the magnetization is said to have undergone *inversion*. If a 180° pulse is applied to already excited magnetization, it is called a *refocusing* pulse, as it permits magnetization with a range of off-resonance frequencies which have dephased to realign in the transverse plane. Refocusing gives a *spin echo*, where all the magnetization realigns before dephasing again due to the dispersion of off-resonance frequencies.

It is often desirable to uniformly excite a frequency band in MRI to limit the spatial extent from which signal originates. Some common amplitude-modulated

(AM) pulses to achieve this are sinc, gauss, and Shinnar-LeRoux (SLR) [16], [17], the last of which is generated numerically. Some examples of these pulses are shown in Fig. 2.2, along with the corresponding transverse magnetization as a function of off-resonance frequency. Often, sinc pulses are filtered either with a gaussian window or a Hanning window [1]. Filtering is useful for sinc pulses, as otherwise they significantly affect magnetization outside the desired frequency band, as seen in the oscillations in Fig. 2.2b.

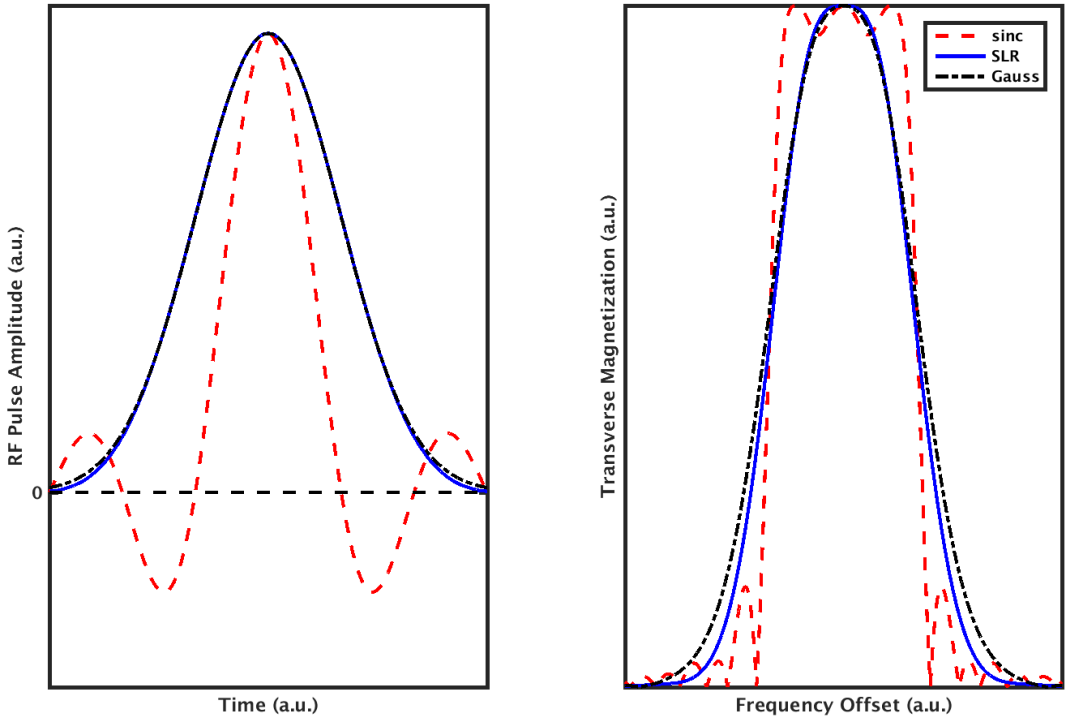

Fig. 2.2. Three example AM pulses, with the legend denoting each. a) The pulse amplitudes as functions of time. Note the similarity of the SLR pulse shape to the gaussian pulse shape. b) The resultant transverse magnetization from each pulse. The transverse magnetization resulting from the SLR pulse is flatter at the top and decays more rapidly moving away from the center. All pulses were simulated with the same bandwidth and flip angle.

For any amplitude modulated pulse of duration T_P, the relationship between its bandwidth *bw* and duration is captured in the dimensionless *time-bandwidth product*,

TBP,

$$\text{TBP} = bw\, T_P. \tag{2.39}$$

For a fixed amplitude-modulation function, TBP is nearly fixed, varying only slightly as a function of flip angle. Thus, to increase the bandwidth of a pulse, its duration must be shortened. In accordance with Eq. 2.38, a shorter pulse necessitates an increase in the peak amplitude of the pulse for a fixed flip angle. The implications of this will be discussed more thoroughly shortly, after coverage of frequency-modulated pulses.

2.2.2 Frequency-Modulated Pulses

Frequency-modulated (FM) pulses provide an alternative mechanism to manipulate spins. Instead of being applied on-resonance at all times, the instantaneous frequency of the pulse is swept as a function of time, while also being amplitude modulated. The time-dependence of the frequency sweep is denoted by $F_2(t)$ while the amplitude modulation is denoted by $F_1(t)$, where $0 \leq F_1 \leq 1$ and $-1 \leq F_2 \leq 1$. Hence, the entire pulse is described by

$$\omega_1 = \omega_1^{\max} F_1(t) \tag{2.40}$$

$$\Delta\omega = AF_2(t) - \omega_L, \tag{2.41}$$

where $\omega_1^{\max}$ is the peak amplitude of the pulse and A is the maximum frequency offset of the pulse.

FM pulses be understood more readily in the *frequency modulated rotating frame*, or FM frame. This frame is one which rotates at the instantaneous frequency of the pulse, with the B_1 amplitude always along the x-axis of the frame, as shown in Fig. 2.3a. In an *adiabatic full passage*, the frequency sweep function is made to start far above resonance with a small B_1 ($\Delta\omega >> \omega_1^{\max}$), sweep through resonance, and continue to sweep far below resonance. This gives an effective B_1, denoted $\vec{B}_{eff}$, which is initially along the z-axis, but whose time-dependent off-axis angle is denoted by

$$\alpha = \arctan\Big(\frac{\Delta\omega(t)}{\omega_1^{\max} F_1(t)}\Big). \tag{2.42}$$

Moving to the B_{eff} frame of reference, where the effective field is placed along the z-axis of the frame, there are only two fields affecting the magnetization. They are the effective field, and a fictitious field, $\frac{d\alpha}{dt}$, shown in Fig. 2.3b. The fictitious field appears due to the change of rotating reference frames. Provided

$$\gamma|\vec{B}_{eff}| >> \frac{d\alpha}{dt} \tag{2.43}$$

at all times, the magnetization will maintain its initial orientation relative to the effective field. Eq. 2.43 is called the *adiabatic condition*, since pulses which satisfy it are said to be adiabatic [18].

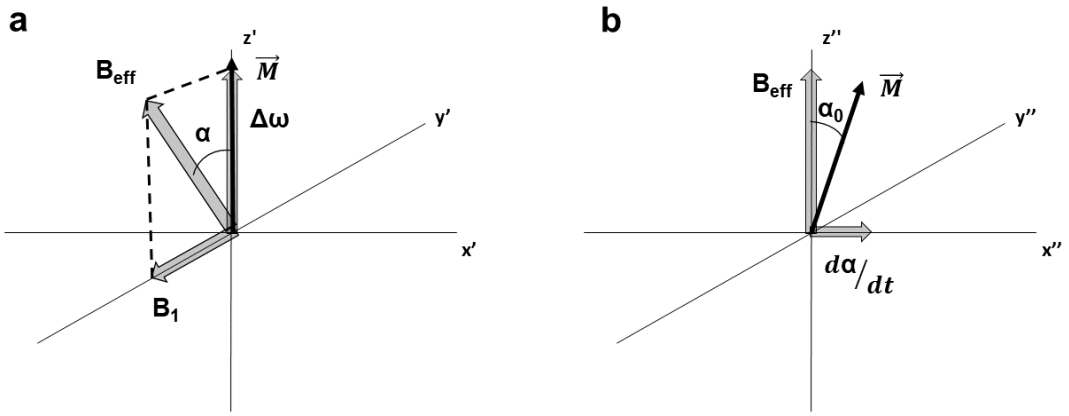

Fig. 2.3. Diagram demonstrating how magnetization follows the effective field of a frequency swept pulse, provided the adiabatic condition is met. This condition is described in the text. a) FM frame, showing the separate B_1 and $\Delta\omega$ fields, as well as their sum, B_{eff}. b) Second rotating frame, with B_{eff} along the z-axis of the frame. Provided $\frac{d\alpha}{dt}$ is negligble, $\vec{M}$ precesses around the effective field with an apex angle α_0 equal to the initial angle between the magnetization and the effective field.

Thus, magnetization follows the effective field during an adiabatic pulse. Adiabatic pulses are insensitive to variations to the peak B_1 amplitude, which is spatially varying in an MRI experiment and can result in spatially varying flip angles. The B_1 insensitivity stems from the adiabatic condition, which provided the peak B_1 is high enough, can be met at all times for a large range of peak pulse powers. These pulses

are therefore frequently used for inversion and refocusing. If the pulse is truncated when the frequency offset $\Delta\omega = 0$, the pulse is said to be an *adiabatic half passage* and can be used for excitation.

Some of the most common frequency-swept pulses in MRI are the *hyperbolic secant*, or HSn, pulses [18],[19],[20]. The amplitudes and frequency sweep functions of HSn pulses, for integer n, are given by

$$F_1(\tau) = \text{sech}(\beta\tau^n) \tag{2.44}$$

$$F_2(t) = \int F_1(t)^2 d\tau, \tag{2.45}$$

where β is a dimensionaless truncation factor and $\tau \, \epsilon \, [-1, 1]$ is a normalized time coordinate. Typically, $\beta = \text{asech}(.01)$, which truncates the pulse at 1% of the peak power. The amplitude and frequency modulation functions for n = 1, 8, and 20 are shown in Fig. 2.4, as well as the resulting M_z when the pulses are driven adiabatically for inversion. As n is increased, a lower peak power is sufficient to achieve adiabaticity at the expense of a less smooth inversion profile as a function of off-resonance.

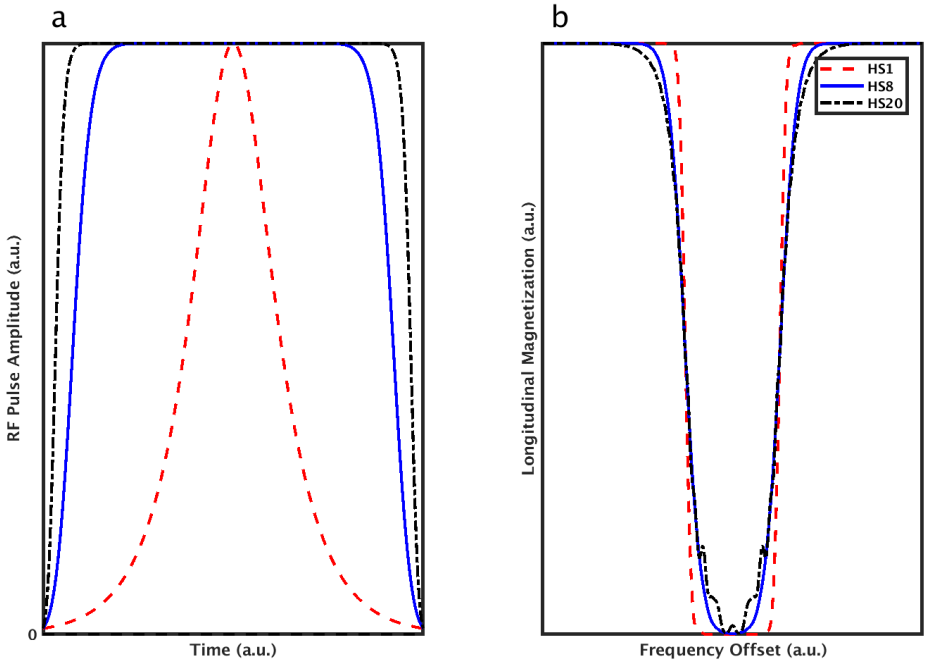

Fig. 2.4. Three example FM pulses, with the legend denoting each. a) The pulse amplitudes as functions of time. b) The resultant longitudinal magnetization from each pulse when driven adiabatically. All pulses were simulated with the same bandwidth and duration.

2.2.3 Specific Absorption Rate

An important safety metric in MRI is the *specific absorption rate* (SAR), which is a measure of the amount of heating induced in a patient due to the RF pulses. The units of SAR are watts per kilogram of tissue, or more generally, energy per time, per mass. The SAR induced by an RF pulse is proportional to the average power of the pulse, which can be measured by

$$\text{SAR} \propto \int_0^{T_P} |B_1(t)|^2 dt. \tag{2.46}$$

By Parseval's theorem [1], the RF power then also satisfies

$$\text{SAR} \propto \int_{-bw/2}^{bw/2} |B_1(f)|^2 df, \tag{2.47}$$

where the integration is performed in the frequency domain and the limits are the bandwidth of the pulse. While quantitative measurements of SAR are monitored directly while scanning using an SAR monitor, it is often beneficial to compare the relative SAR of different pulses using Eq. 2.46 or Eq. 2.47. Moreover, it is clearly seen that using a higher flip angle (Eq. 2.38) requires a higher peak B_1, and thus significantly more energy is absorbed by a patient. Eq. 2.47 demonstrates that as the bandwidth of the pulse increases, the SAR also increases quadratically.

2.2.4 *k*-space Description of Multidimensional Pulses

The earlier description sheds some light on common pulses used in magnetic resonance. It is often desirable, however, to demand a more tailored excitation than the profiles given in the previous subsection. For this reason, an understanding of the connection between RF waveform and resultant transverse magnetization profile is sought. A cursory examination of the results of Fig. 2.2 demonstrates that the excitation profile closely resembles the Fourier transform [1] of the RF pulse. Since magnetization motion is governed by RF frequencies near resonance, it makes intuitive sense that the response of the magnetization at a fixed frequency offset should behave according to the corresponding frequency content of the RF pulse. This notion was codified by Pauly et al. [21] in the k-space formalism of excitation, which holds provided the flip angle is small. It is therefore frequently called the *small-tip-angle approximation*.

The crux of the derivation lies in the assumption of a small flip angle. In this limit, the longitudinal magnetization M_z is assumed to be static, i.e.

$$M_z \approx M_0. \tag{2.48}$$

The equations of motion for the transverse magnetization simplify to

$$\frac{dM_{xy}}{dt} = i\gamma\vec{G}(t)\cdot\vec{x}M_{xy} + i\gamma B_1(t)M_0, \tag{2.49}$$

where $\vec{G}(t)$ are time varying gradient waveforms and B_1 is the RF field, which may be complex. This is easily solved to give

$$M_{xy}(\vec{x}) = i\gamma M_0 \int_0^{T_\mathrm{P}} B_1(t) e^{-i\gamma\vec{x}\cdot\int_t^{T_\mathrm{P}}\vec{G}(s)ds} dt. \tag{2.50}$$

Defining a spatial frequency variable

$$\vec{k}(t) = -\gamma\int_t^{T_\mathrm{P}} \vec{G}(s)ds, \tag{2.51}$$

Eq. 2.50 becomes

$$M_{xy}(\vec{x}) = i\gamma M_0(\vec{x}) \int_0^{T_\mathrm{P}} B_1(t) e^{-i\vec{x}\cdot\vec{k}(t)} dt. \tag{2.52}$$

While this resembles a Fourier transform, as of yet, it is not. A detailed derivation is described in [21], and the result is merely presented here. With a k-space weighting factor $W(\vec{k}) = \frac{B_1}{|\gamma\vec{G}(t)|}$ and a k-space trajectory $S(\vec{k})$, the excitation profile M_{xy} is given by

$$M_{xy}(\vec{x}) = i\gamma M_0(\vec{x}) \int_{\vec{K}} W(\vec{k})S(\vec{k}) e^{i\vec{x}\cdot\vec{k}} d\vec{k}. \tag{2.53}$$

Thus, the magnetization is seen to be the Fourier transform of the weighted k-space trajectory, where the weighting is proportional to the B_1 field and inversely proportion to the rate at which k-space is sampled. An example 2D pulse with Cartesian k-space trajectory is presented in Fig. 3.1, where the excitation profile is also shown.

As an aside, as it is discussed in Chapter 4, in the presence of an inhomogeneous transmit field, Eq. 2.52 can be recast as

$$M_{xy}(\vec{x}) = i\gamma M_0 B_1(\vec{x}) \int_0^{T_\mathrm{P}} B_1(t) e^{-i\vec{x}\cdot\vec{k}(t)} dt, \tag{2.54}$$

where the spatial and temporal dependence of the transmit field are separable.

2.3 Acquisition and Image Encoding Methods

2.3.1 Signal Detection

The establishment of transverse magnetization following an RF pulse was discussed in Section 2.1.1. In the lab frame, the magnetization precesses about the B_0 field while slowly relaxing. Ignoring relaxation during acquisition, which is short relative to the relaxation times, the electromotive force induced in the RF coil by the precessing magnetization is given by Faraday's law

$$\begin{aligned} emf &= -\frac{d}{dt}\int_S \vec{B}(t)\cdot\hat{n}dS \\ &= -\frac{d}{dt}\Phi_M(t). \end{aligned} \tag{2.55}$$

where $\vec{B}$ is spatially dependent although not explicitly written as such to focus on the time-dependence. In Eq. 2.55, the magnetic flux has been defined as

$$\Phi_M(t) = \int_S \vec{B}(t)\cdot\hat{n}dS, \tag{2.56}$$

and the integral is performed over the surface S defined by the RF coil. Focusing on the calculation of magnetic flux, the magnetic field is the curl of the *vector potential* $\vec{A}$, such that

$$\vec{B}(t) = \nabla\times\vec{A}(t). \tag{2.57}$$

Inserting this into Eq. 2.56,

$$\Phi_M(t) = \int_S \nabla\times\vec{A}(t)\cdot\hat{n}dS \tag{2.58}$$

$$= \oint_{\partial S}\vec{A}(t)\cdot d\vec{l}, \tag{2.59}$$

with $d\vec{l}$ a parameterized differential length element of the RF coil and ∂S denotes the boundary of the surface S. The final line of Eq. 2.58 was obtained by applying Stokes' theorem [14].

For a source current distribution $\vec{J}(\vec{r}', t)$, the vector potential satisfies

$$\vec{A}(\vec{r}, t) = \frac{\mu_0}{4\pi} \int_V \frac{\vec{J}(\vec{r}', t)}{|\vec{r} - \vec{r}'|} d^3 r' \tag{2.60}$$

where the integral is performed over all space. Since magnetization gives rise to a magnetic field and a corresponding vector potential, in light of Eq. 2.60, the magnetization can be written in terms of an effective current [14], with $\vec{J} = \nabla \times \vec{M}$. The magnetic flux can then be written in terms of the magnetization as

$$\Phi_M(t) = \frac{\mu_0}{4\pi} \int_V \oint_{\partial S} d\vec{l} \cdot \frac{\nabla' \times \vec{M}(\vec{r}')}{|\vec{r} - \vec{r}'|} d^3 r' \tag{2.61}$$

with ∇' indicating derivatives with respect to the primed coordinates. The product rule for the curl of a scalar multiplied with a vector field is

$$\nabla \times (\phi \vec{F}) = \phi \nabla \times \vec{F} + (\nabla \phi) \times \vec{F}. \tag{2.62}$$

Identifying $\phi = \frac{1}{|\vec{r} - \vec{r}'|}$ and $\vec{F} = \vec{M}$, the integrand in Eq. 2.61 can be recast as

$$\Phi_M(t) = \frac{\mu_0}{4\pi} \int_V \oint_{\partial S} d\vec{l} \cdot \Big(\nabla' \times \frac{\vec{M}(\vec{r}')}{|\vec{r} - \vec{r}'|} - \nabla' (\frac{1}{|\vec{r} - \vec{r}'|}) \times \vec{M} \Big) d^3 r'. \tag{2.63}$$

Considering the volume integral of the first term in parenthesis, it becomes a surface integral upon applying the *divergence theorem* [14], where the surface of integration is that bounding all of space. Clearly there are no source currents or effective source currents there, so this term evaluates to zero, leaving

$$\Phi_M(t) = -\frac{\mu_0}{4\pi} \int_V \oint_{\partial S} d\vec{l} \cdot \Big(\nabla' (\frac{1}{|\vec{r} - \vec{r}'|}) \times \vec{M} \Big) d^3 r'. \tag{2.64}$$

Utilizing the vector identify $\vec{A} \cdot (\vec{B} \times \vec{C}) = -(\vec{A} \times \vec{C}) \cdot \vec{B}$, the flux can be rewritten as

$$\Phi_M(t) = \frac{\mu_0}{4\pi} \int_V \vec{M} \cdot \Big(\nabla' \times \oint_{\partial S} \frac{d\vec{l}}{|\vec{r} - \vec{r}'|} \Big) d^3 r'. \tag{2.65}$$

The term $\nabla' \times \oint_{\partial S} \frac{d\vec{l}}{|\vec{r}-\vec{r}'|}$ is of the form of Eq. 2.57. For a one-dimensional current, the vector potential is given by

$$\vec{A}(\vec{r},t) = \frac{\mu_0}{4\pi} \oint I \frac{d\vec{l}(\vec{r}',t)}{|\vec{r}-\vec{r}'|} d^3r'. \tag{2.66}$$

In light of Eq. 2.57, and restoring all spatial dependencies, the magnetic flux is then

$$\Phi_M(t) = \frac{\mu_0}{4\pi} \int_V \vec{M}(\vec{r}') \cdot \frac{\vec{B}_{receive}(\vec{r}')}{I} d^3r', \tag{2.67}$$

where $\vec{B}_{receive}(\vec{r}')$ is the magnetic field at point $\vec{r}'$ due to a current I through the receive coil. Thus, the quantity

$$\vec{\beta}_{receive}(\vec{r}') = \vec{B}_{receive}/I \tag{2.68}$$

is the magnetic field per unit current produced at the point $\vec{r}'$ and is referred to as the *receive field* of the RF receiver coil. Therefore, the flux is

$$\Phi_M(t) = \frac{\mu_0}{4\pi} \int_V \vec{M}(\vec{r}') \cdot \vec{\beta}_{receive}(\vec{r}') d^3r'. \tag{2.69}$$

The detected signal in the form of the induced emf is then

$$emf = -\frac{d}{dt} \int_V \vec{M}(\vec{r}',t) \cdot \vec{\beta}_{receive}(\vec{r}') d^3r'. \tag{2.70}$$

Only the transverse magnetization precesses, so the dominant time-dependence in Eq. 2.70 is the precessional motion occuring in the transverse plane. Since the precession occurs at the Larmor frequency, the magnetization during acquisition is commonly written in complex form as

$$\vec{M}(\vec{r}',t) \rightarrow M_{xy}(\vec{r}') e^{-i\omega_L t}. \tag{2.71}$$

The derivative in Eq. 2.70 is then simply replaced with $-i\omega_L$ multipled with the original quantity. From this, it is evident that a high Larmor frequency, which cor-

responds to a larger magnetic field, gives rise to a higher amplitude signal in the RF coil. Further, the detected quantity is not just the magnetization - it is the product of the magnetization with the receive field. The effects of this can be overcome by using an array of RF coils [22], or by measuring the receive field and dividing it out of the image, as was done by [23], [24], and as done in Chapter 3.

2.3.2 Image Encoding

Denoting the transverse component of the receive field by β_{xy}, the detected signal is given by

$$s_{\text{lab}}(t) = \int_V \beta_{xy}(\vec{r}) M_{xy}(\vec{r}, t) e^{-i\omega_L t} d\vec{r}, \tag{2.72}$$

where the volume integral is performed over the excited magnetization [1]. The quantity $e^{-i\omega_L t}$ is not spatially dependent and does not contribute to image encoding. It is therefore removed from the signal by *demodulation*, or multiplying by $e^{i\omega_L t}$, yielding

$$s_{\text{demod}}(t) = \int_V \beta_{xy}(\vec{r}) M_{xy}(\vec{r}, t) d\vec{r}. \tag{2.73}$$

When using an array of receivers, the receive fields themselves can be used for image encoding. This technique is called *parallel imaging* [25], [26]. However, when using a single receiver or when not employing parallel imaging, the receive field is typically absorbed into the definition of the magnetization. The product of the two is then the reconstructed image. In the following, this is the convention used, so the receive field in the signal equation will be ignored, with the exception of Chapter 4.

Under current assumptions, the time-dependence of the magnetization $M_{xy}(\vec{r}, t)$ is contained only in the phase of the magnetization. The phase is modulated using gradients during acquisition, imparting a spatially dependent resonance offset, in turn yielding additional precession. In time, the dispersion of off-resonances results in a linearly varying spatial phase across the object as a function of time. Quantitatively, expanding the polarizing field as $B_0(\vec{x}) = B_0 + \vec{G} \cdot \vec{x}$, the phase term is given by

$\exp\Big\{-i\gamma \int_0^t \vec{G}(s) \cdot \vec{x} ds\Big\}$. The signal is then written as

$$s(t) = \int_V M_{xy}(\vec{r}) e^{-i\vec{k}(t)\cdot\vec{r}} d\vec{r}, \tag{2.74}$$

where

$$\vec{k}(t) = \gamma \int_0^t \vec{G}(s) ds. \tag{2.75}$$

This $\vec{k}$ is distinctly different than the $\vec{k}$ defined for excitation in Section 2.2.4. There, the integral was performed over the remaining gradient to be applied, whereas here, the integral is over the gradient which has already occurred. Eq. 2.74 shows that the magnetization as a function of space (the image), and the signal form a Fourier pair, and the magnetization can be recovered using a Fast Fourier Transform (FFT) [27]. The signal space in multidimensional experiments is a function of $\vec{k}$ and is referred to as k-space. Example k-space trajectories are shown in Fig. 2.5. Fast reconstructions for non-Cartesian trajectories can be obtained by *gridding*, or interpolation onto a Cartesian grid, followed by FFT [28].

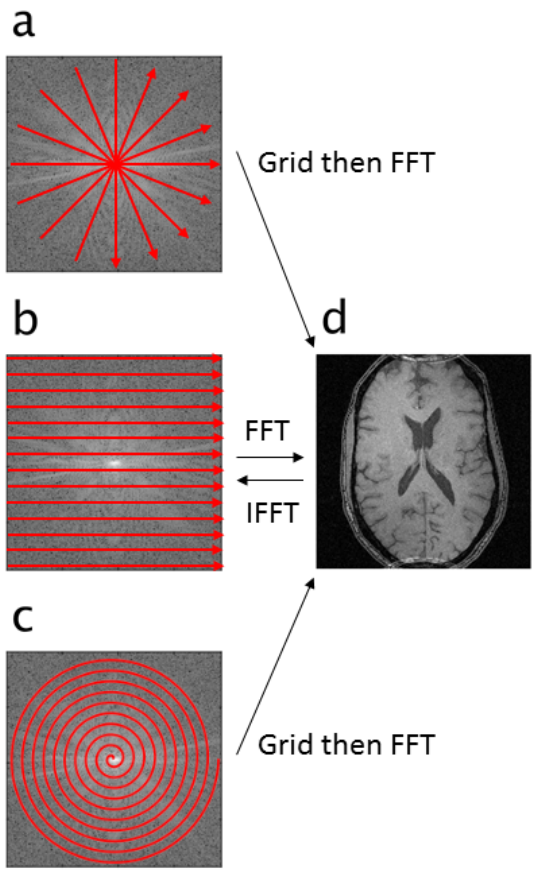

Fig. 2.5. Various k-space trajectories overlaid upon a log image of the signal magnitude, along side the reconstructed image. a) Radial k-space coverage. b) Cartesian k-space coverage. c) Spiral coverage. d) Reconstructed image. The inverse FFT is applied between Cartesian coordinate systems only. Applying the Nonuniform FFT or inverse gridding can resample the inverse FFT of the image onto non-Cartesian coordinates.

To faithfully reconstruct the image using Eq. 2.74, k-space must be *fully sampled*. Discrete sampling of k-space, as is done with the digital receivers in MRI, implies a band-limited signal. The gradients induce a range of frequencies over the object being imaged, with a finite bandwidth, bw, over the object within the RF coil. Hence, the assumption of a band-limited signal is justified. However, the sampling frequency, sw, must exceed twice the maximum frequency component of the signal, $sw \geq 2/(bw)$ which is called the *Nyquist criteria*.

There are an infinite number of possible signals which recreate discretely sampled data, each an identical replica of the lowest frequency signal, modulated by a high frequency offset. These replicas are called *sidebands*, while the primary signal is called the *baseband*. When the sidebands overlap the baseband, *aliasing* occurs, and the image is said to be *undersampled*. Aliasing occurs when sampling is performed below the Nyquist limit. When the sidebands do not overlap the baseband, the image is said to be fully sampled. The spacing of the sidebands from the baseband is called the field-of-view (FOV), and is given by FOV $= \frac{1}{\Delta k}$. Here, Δk is the spacing between samples in k-space. The *resolution*, or voxel size in the image, is given by $\Delta x = \frac{1}{2k_{\max}}$, with $k_{\max}$ the maximum k-space value sampled.

2.3.3 Quantitative Relaxation Mapping

The transverse magnetization in Eq. 2.74 is dependent on the temporal separation from the time of excitation to the time when the signal is acquired. This time delay, the *echo time* t_E, is controlled by the experimenter and changes the contrast of the acquired image according to the relaxation time T_2. In the case of a spin-echo acquisition, Eq. 2.74 can be slightly rewritten to accommodate this as

$$s(t) = \int_V M_{xy}(\vec{r}) e^{\frac{t_E}{T_2(\vec{r})}} e^{-i\vec{k}(t)\cdot\vec{r}} d\vec{r}. \tag{2.76}$$

Hence, the reconstructed image is then $M_{xy}(\vec{r}) e^{\frac{t_E}{T_2(\vec{r})}}$. By acquiring the image with a set of different t_E's, the numerical value of $T_2(\vec{r})$ can be determined as a function of position. This is done by performing a three-parameter nonlinear least squares fitting of the data to the exponential decay curve [29],

$$I(T_E(n), \vec{r}) = A + B \exp^{-\frac{T_E(n)}{T_2(\vec{r})}}, \tag{2.77}$$

for A, B, and T_2. Here, $I(T_E(n), \vec{r})$ denotes the image intensity for the n^{th} echo time at the voxel centered about $\vec{r}$. The fitting is performed on a voxel-by-voxel basis, and the echo times are indexed by the variable n.

2.4 Comments on Quantum Description

It has been argued that quantum mechanics is largely unnecessary for understanding typical MRI measurements [30]. According to the *correspondance principle* [31], in the limit of large energies and large quantum numbers, quantum mechanical predictions merge with those of classical physics. Indeed, in biomedical applications, imaging takes place at approximately 300 K, resulting in thermal energies significantly larger than the energies associated with any clinically applicable magnetic field strength (1.5T - 7T) and inter-spin interaction energies. Additionally, sample sizes contain on the order of 10^{22} protons, obscuring quantum effects. The spins can then be treated as isolated and uncoupled from their environment, resulting in a two-level system. Feynman et al. [32] demonstrated that any two-level system may be understood with classical equations of motion. Therefore, the remainder of this work assumes classical dynamics of the spin systems under investigation.

Chapter 3

Two-Dimensional Frequency-Swept Pulse with Resilience to Both B_1 and B_0 Inhomogeneity

This chapter has been published as a manuscript in the Journal of Magnetic Resonance [33]. A corrigendum has also been published [34].

3.1 Introduction

Two- (2D) and three-dimensional (3D) MRI methods usually employ radiofrequency (RF) pulses that are spatially selective in one direction only. Following RF excitation, phase encoding in one or more directions is then used to spatially encode the ensuing signal. Since this is a Fourier encoding strategy, Nyquists criterion must be met, which necessitates using a field-of-view (FOV) at least as large as the object in all directions. When a high resolution is desired in the phase-encoded direction(s), this condition can lead to lengthy acquisition times. To reduce the acquisition time, a RF pulse that is selective in more than one spatial dimension can be used to delineate a smaller FOV in one or more of the phase-encoded dimensions.

As first described by Pauly et al. [21], multidimensional small tip angle pulses may be described by a parameterized trajectory through k-space, where the trajectory

is determined by the linear field gradients used during the pulse. That work was then extended to large tip angle pulses by Pauly et al. [35], where it was shown that a large tip angle could be achieved if the pulse could be decomposed into several inherently refocused, small tip angle pulses. Here, inherently refocused is synonymous with returning to $\vec{k} = 0$ in excitation k-space. All these 2D pulses were performed in a single shot; in other words, the entirety of k-space was sampled for the pulse in one excitation. A similar approach by Conolly et al. [36] repeatedly plays out sinc pulses during an oscillating echo-planar type of gradient train. The peak amplitude and initial phase of each sinc pulse are modulated according to those of a hyperbolic secant pulse [19] to produce a 2D adiabatic pulse. For this 2D pulse and others similar to it, the large number of pulses necessary to fully sample the 2D k-space of the pulse can lead to prohibitively long pulse duration.

In the 2D pulses of Conolly et al. [36], the bandwidth of the pulse in the direction of the oscillating gradient can be increased by using a frequency-modulated (FM) pulse in place of the amplitude-modulated sinc pulses. This was the approach taken by Dumez et al. [37], whereby chirp pulses were used in both dimensions. The pulse design in that work was described in physical space, not in k-space, and equations describing the pulse design were not given.

Here, we describe a 2D RF pulse which is a hyperbolic secant pulse in both dimensions in k-space. We use an echo-planar imaging (EPI) [38] gradient train during the excitation, and increase the low bandwidth achieved in the slow dimension of the pulses used in previous works. Specifically, we undersample different segments of the pulse to decrease the length of each pulse segment, thus increasing the bandwidth for a fixed time-bandwidth product, R.

Hereafter, the direction of the oscillating gradient will be referred to as the fast-selected dimension, while the direction of the blipped gradient will be referred to as the slow-selected dimension. This nomenclature is due to the relative time needed for spatial selection in each dimension. As was done by Jang et al. [39], B_1^+ inhomogeneity will be addressed by scaling the time-dependent RF amplitude based on a B_1^+ map and having knowledge of the spatiotemporal vertex produced by the 2D FM pulse.

3.2 Theory

3.2.1 Two-dimensional Cartesian excitation

Denoting a normalized k-space vector by $\kappa_{f,s}\epsilon[-1,1]$ in the fast and slow dimensions, respectively, the amplitude- and phase-modulated functions of the RF pulse, as defined in terms of the pulses k-space trajectory, are

$$\omega_1 = \omega_{1,max}\text{sech}\big(\beta\kappa_f(t)\big)\text{sech}\big(\beta\kappa_s(t)\big) \tag{3.1}$$

$$\phi_{RF} = A_f\log\Big(\cosh\Big(\beta\kappa_f(t)\Big)\Big) \pm A_s\log\Big(\cosh\Big(\beta\kappa_s(t)\Big)\Big). \tag{3.2}$$

In these equations, β determines where these functions are truncated, and ni the present work, its value was determined according to $\text{sech}(\beta) = 0.01$ (i.e., the amplitude-modulated function truncates at 1% of maximum). In Eq (3.2), choosing the positive sign leads to a parabolic phase over the object, while a negative sign yields a hyperbolic phase profile. For the remainder of this work, the negative sign will be used. Additionally, $\kappa_{f,s}$ are normalized by $k_{f,s} = \frac{\gamma}{2}\Big|\int_0^{T_P} G_{f,s}(t')dt'\Big|$, which is Eq (7) of [21]. Denoting the time-bandwidth product of the pulse in the fast and slow dimensions as R_f and R_s respectively, the coefficients $A_{f,s}$ are defined by $A_{f,s} = \frac{\pi R_{f,s}}{2\beta}$. The formulae given yield a rectangular excitation profile, although the same trajectory can be used with the k-space weighting as described by Jang et al. [39] to obtain a circular excitation profile. In the latter case, the single-shot Cartesian trajectory also yields an adiabatic pulse. Profile thickness is given in both dimensions of the current pulse as

$$\Delta x_{f,s} = \frac{R_{f,s}}{2k_{\{f,s\},max}}, \tag{3.3}$$

where f and s denote the fast and slow dimensions, respectively. For B_1 compensation, the instantaneous vertex position is given by

$$x_{f,s} = \frac{\Delta x_{f,s}}{2}\kappa_{\{f,s\}}(t). \tag{3.4}$$

Further below it will be shown how Eq (3.4) can be used to modify the pulse to produce a uniform flip angle with a spatially-varying RF field, B_1^+. While the 2D

spatial selection can be performed in any orientation, the fast and slow spatially-selected dimensions will herein generally be referred to as X and Y, respectively.

3.2.2 Segmentation

As mentioned in the Introduction, the bandwidth in the fast-selected dimension can be further increased by replacing the sinc pulses in the 2D pulse by Conolly et al. [36] with frequency-swept pulses. The 2D frequency-swept pulses in this work are based on the original hyperbolic secant pulse, HS1 [19], but other frequency-swept pulses can also be used, including higher order HSn pulses [20] or a chirp pulse [40], as was done by Dumez et al. [37]. The k-space representation of this pulse and its Bloch simulated excitation profile are shown in Fig. 3.1. The bandwidth in the slow-selected dimension can be increased by only sampling segments of the fully sampled 2D pulse with each excitation, as shown in Fig. 3.2. This decreases the pulse length while maintaining R, such that the bandwidth in the slow dimension increases in inverse proportion to the pulse length reduction. However, to retain the desired 2D excitation profile, a full image readout must be acquired for each pulse segment. Depending on the specific sequence used, this might necessitate a complex tradeoff between minimum scan time and pulse bandwidth, since as the pulse is shortened, the minimum possible repetition time TR decreases. For a fixed TR, the total acquisition time scales linearly with the number of pulse segments used. At the end of all acquisitions, the data are summed over all segments in either k-space or image space with the appropriate weights.

Using a 2D pulse permits increased spatial resolution in a fixed imaging time by decreasing the FOV in the phase-encoded dimensions of an experiment. By segmenting the pulse with a fixed TR, the acquisition time increases multiplicatively with the number of segments. Thus, to avoid increasing imaging time, the number of segments used must not exceed the acceleration gained by shrinking the FOV. If we assume that phase encoding is performed in the zoomed spatial dimensions, then the number of segments $\mathrm{N_{seg}}$ should ideally satisfy

$$\mathrm{N_{seg}} = \frac{PE_{1,\mathrm{full}}}{PE_{1,\mathrm{zoomed}}} \frac{PE_{2,\mathrm{full}}}{PE_{1,\mathrm{zoomed}}} \tag{3.5}$$

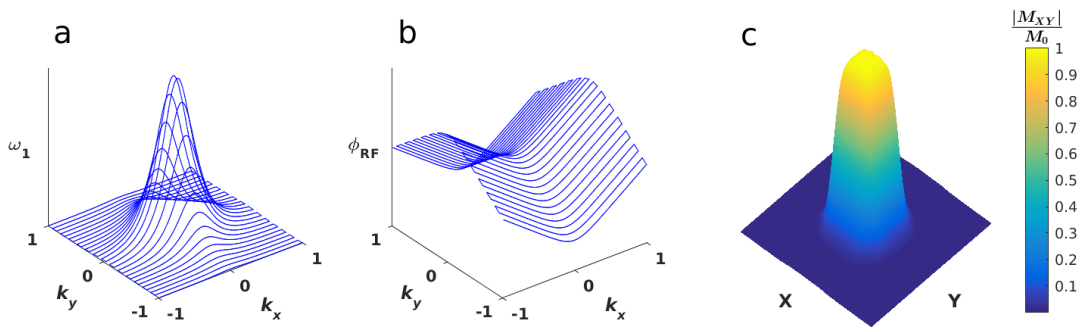

Fig. 3.1. k-space description of the 2D pulse. a) The RF amplitude as a function of k-space. b) The RF phase as a function of k-space. c) The transverse magnetization (M_{xy}) profile produced by this pulse.

to not increase the imaging time, where $PE_{i,\text{full}}$ and $PE_{i,\text{zoomed}}$ denote the number of phase encoded steps in a given dimension (i) in the full and zoomed FOV, respectively. This assumes equal resolution between zoomed and full FOV scans.

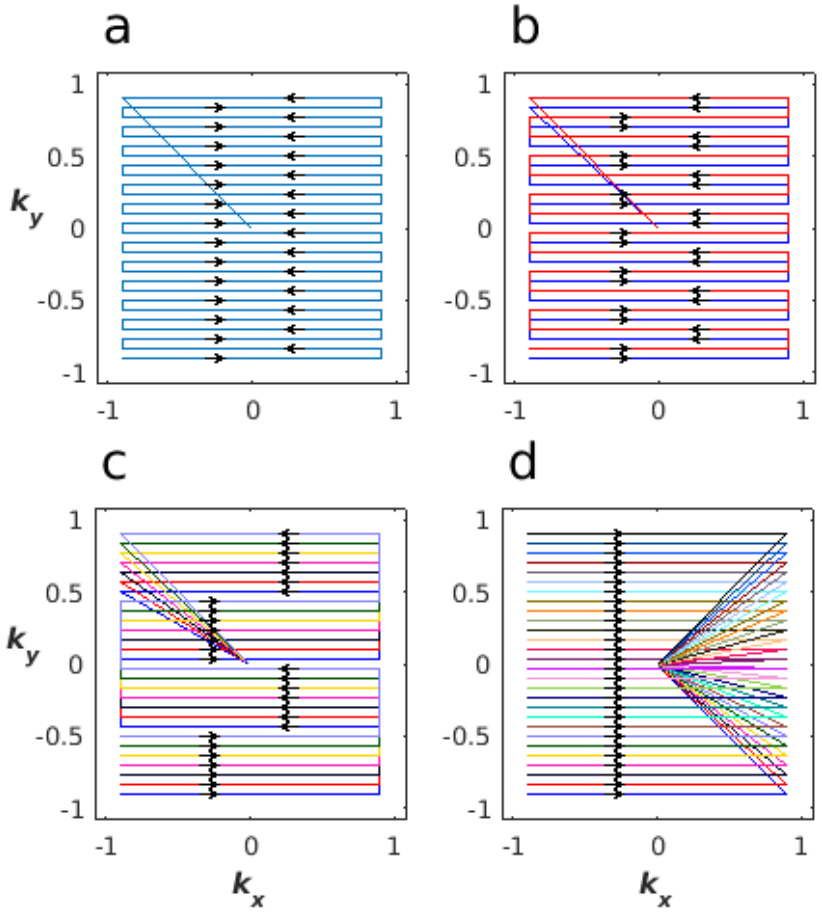

Fig. 3.2. Example k-space trajectories for a 2D RF pulse. a) A single segment coverage of k-space. b) Covering k-space in 2 segments, with each segment sampling 14 equidistant lines of k-space. c) 7-segment trajectory, with each segment sampling 4 equidistant lines of k-space. d) Fully segmented trajectory, sampling only 1 line of k-space with each segment. Another option for segmented pulses is to alternate the initial direction of the k-space trajectory between segments, which gives different off-resonant behavior. Trajectories do not need to be interleaved as shown. Segmented trajectories which sample k-space sequentially and do not overlap are also possible. Colors were chosen using [41].

To sample each segment correctly in pulse k-space, care must be taken to ensure each segment has the same k-space center defined. Since the k-space trajectory is defined by the integral of the remaining gradient, there must be a variable area

gradient lobe at the end of each segment in the slow-selected dimension. If these refocusing lobes are not the correct magnitude and polarity, different segments may amount to sampling the pulse multiple times along the same line(s) of k-space. Hence, the trajectory of a given segment depends crucially on the refocusing gradient, and the sampling weight depends on the RF amplitude and phase. Thus, even though each segment can use the same gradient waveform during RF transmission, its exact trajectory in k-space is determined by the gradient refocusing lobe that follows the RF pulse(s) of a given segment.

3.2.3 Obtaining consistent contrast

As a consequence of the amplitude modulation in the 2D HS1 pulse, each pulse segment produces a different flip angle. As a result, under the commonly used acquisition condition TR $<<$ T_1, the different pulse segments produce variable T1-weighting of the image data. This can be remedied by rescaling the power of each pulse segment to achieve a constant flip angle for all segments. However, during the summation over all segments used, perfect signal cancellation outside the desired selected region does not occur. This issue is readily solved by reweighting the reconstruction of each segment with a weight equal to the original flip angle of the segment. For a fully segmented pulse in which one line of k-space is sampled per segment, this procedure then amounts to reweighting each reconstruction according to a HS1 pulse defined by the number of segments used. For a partially segmented pulse, the data for each segment is scaled in post-processing by the integral of the respective pulse segment. The weights are given by

$$C_i = \max\Big| \int_0^{T_P} \omega_{1,i}(t) \exp\Big(- j\, \phi_{RF,i}(t)\Big) \exp\Big(j\, \vec{k}_i(t) \cdot \vec{r}\Big) dt\Big|, \tag{3.6}$$

where the subscript i denotes segment number and $j = \sqrt{-1}$.

When undersampling a pulse, the sidebands in the slow dimension move closer to the baseband as the number of segments increases. The signals from these sidebands cancel only after summing the acquired data. When a pulse segment is undersampled beyond the Nyquist limit, the sidebands and baseband overlap, and this leads to a

non-uniform flip angle per segment. Thus, in this case, despite maintaining the proper excitation region after summation, it is not possible to obtain a consistent flip angle across the entire excitation region for each segment. However, when using a fully segmented pulse, such spatial variation of the flip angle in the slow dimension does not occur for any segment. In this limiting case, there is again uniform T_1 contrast within the desired profile.

While rescaling the pulse amplitude to achieve the same flip angle for each segment gives equal SNR for each readout, rescaling the data in post-processing before summation yields a suboptimal SNR. The exact SNR can be calculated using Eq. 2 of [42], wherein the SNR as a fraction of the maximum possible for N segments is

$$\frac{\mathrm{SNR}_{\mathrm{seg}}}{\mathrm{SNR}_{\text{single-shot}}} = \frac{\sum_{i=1}^{N} |C_i|}{\sqrt{N \sum_{i=1}^{N} |C_i|^2}}, \tag{3.7}$$

where the C_i are the coefficients used to scale the data in post-processing.

3.2.4 B_1^+ Compensation

Because the pulse is phase modulated in two spatial domains, 2D spatiotemporal excitation takes place during the pulse in a manner that is dictated by the resulting (rasterized) trajectory of a hyperbolic phase function in space. By assuming excitation at a given moment is localized to the vertex of this hyperbolic phase function, the 2D pulse can be modified to achieve uniform flip angle despite the existence of significant B_1^+ inhomogeneity. The process begins by obtaining a unitless B_1^+ map (denoted by $B_{1,c}^+$) that is normalized to 1 at its maximum. Then the RF waveform can be recalculated as

$$\omega_{1,c}(t) = \frac{\omega_1(t)}{B_{1,c}^+(x_f(t), x_s(t))}, \tag{3.8}$$

where x_f and x_s describe the vertex position in the fast and slow dimensions respectively. In areas where the B_1^+ map is not well defined, the original pulse value may be used.

3.3 Simulations

3.3.1 Adiabaticity and Off-Resonance Effects

The simulated pulse consisted of 28 lines of k-space describing the pulse in the slow dimension. Additionally, the R value in both directions of the pulse was set to 9 and the slab thickness set at 5 cm. Each subpulse element, which samples one line of pulse k-space, was 700 s. The duration of the gradient blips in the slow dimension were 120 s with a half-sinusoid shape. Taken together with the number of lines of k-space, these parameters fully define the 2D pulse according to Eqs (3.1) - (3.3) . An example MATLAB script for creating a segmented 2D HS1 pulse is found in [43]. In the following simulations, relaxation effects have been ignored.

As shown in Fig. 3.3, the 2D HS1 pulse can be driven adiabatically when sampled on a Cartesian k-space trajectory, in contrast to the 2D spiral trajectory described in [39]. When driven sub-adiabatically (Figs. 3.3.a and 3.3.b), the 2D excitation profile remains square and unchanged even when altering the excitation flip angle. When driven adiabatically, the cross section through the fast dimension (Fig. 3.3.c) becomes wider than that through the slow dimension (Fig. 3.3.d) as the peak RF amplitude ($\omega_1^{\max} = \gamma B_1^{\max}$) increases. This happens because the transition regions in the profile of each subpulse undergo adiabatic inversion in the process of executing the full 2D pulse.

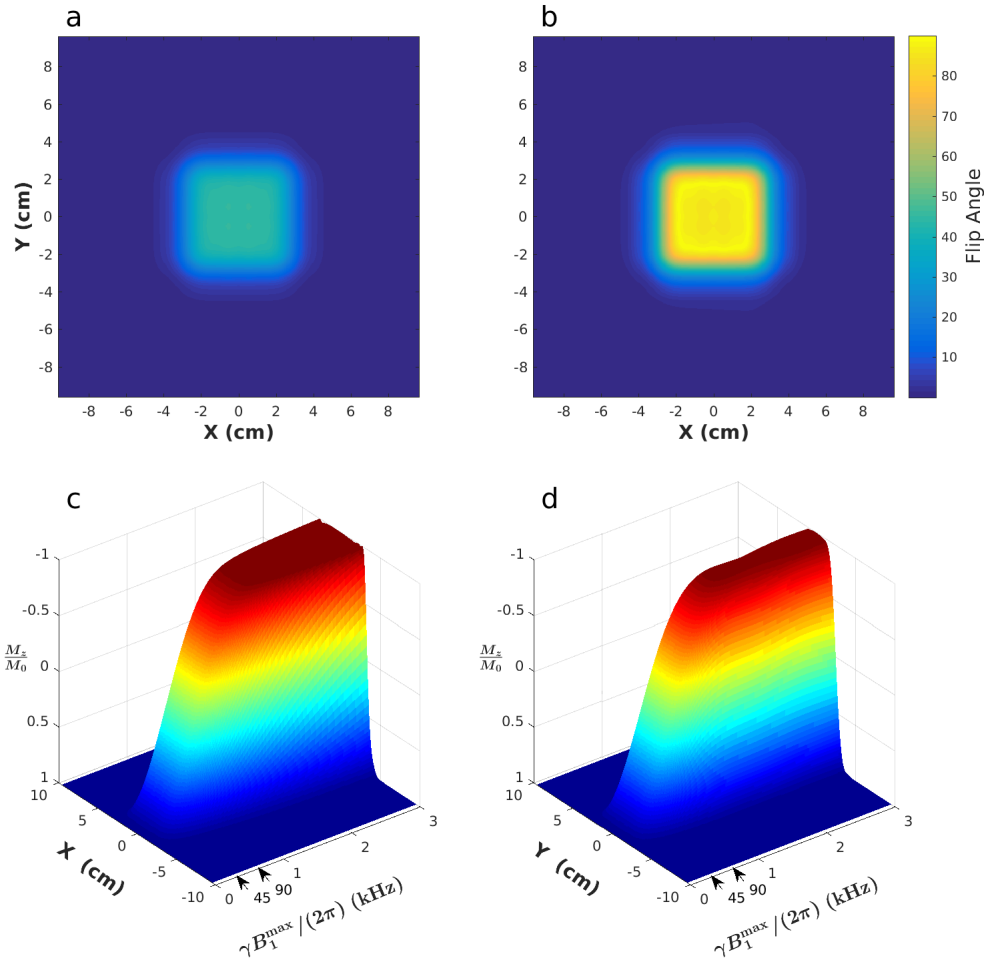

Fig. 3.3. Demonstration of the non-adiabatic and adiabatic regimes of the single shot 2D pulse. a) Transverse magnetization when applying the single-shot pulse for a 45° excitation. b) Transverse magnetization when applying the single-shot pulse for a 90° excitation. Notice the profile width is unchanged in both spatial dimensions. c) Surface plot showing the normalized longitudinal magnetization along the fast dimension as a function of B1max when traversing all of k-space in a single shot. When the pulse begins operating adiabatically, the transition regions begin to invert, increasing the slab width in the fast dimension. d) Surface plot showing the longitudinal magnetization along the slow dimension as a function of $B_1^{\max}$ when traversing all of k-space in a single-shot. $B_1^{\max}$ denotes the peak B_1 used in the pulse. Arrows in (c) and (d) indicate the RF amplitude settings used to obtain the 45° and 90° flip angles for (a) and (b).

The Bloch simulated magnitude and phase of the excitation profile are shown in Fig. 3.4. Similar cross sections showing the excitation profile through the fast and slow dimensions for various offset frequencies are given in Fig. 3.5. In the ideal case, there should be no dependence of the excitation profile on offset frequency, but Bloch simulations reveal the inability of the single-shot pulse to maintain a consistent profile in the presence of large frequency offsets in either the fast or slow dimensions. Despite the large bandwidth in the fast dimension, frequency offsets prevent spin isochromats from returning through $\vec{k} = 0$ with each sweep, marring the profile in that direction. In the slow dimension, constant frequency offsets cause translations in physical space of the excitation profile. As the number of pulse segments is increased, the fast dimension noticeably improves in quality. In the slow dimension, it can be observed that the unwanted transverse magnetization away from the desired excitation region has diminished in amplitude relative to the single shot case, although this is not as apparent as in the fast dimension. For the fully segmented pulse, the selected region exhibits only translation in physical space as a function of the frequency offset, while the slow dimension exhibits complete independence from constant frequency offsets.

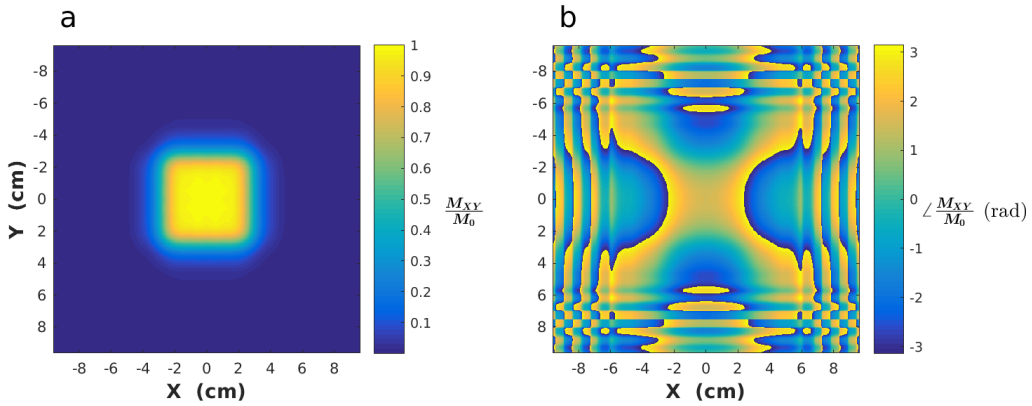

Fig. 3.4. Excitation profile of the 2D pulse for any number of segments. a) Magnitude of the normalized transverse magnetization profile at the end of the pulse for any number of segments, provided they are properly weighted prior to summing. b) Phase of the transverse magnetization profile (radians).

Such a dramatic difference between the fully segmented pulse and any of the

partially segmented pulses can be understood as follows. Ideally, the transverse magnetization does not freely evolve between different sampling times of $k_{\text{fast}} = 0$. If the time between sampling $k_{\text{fast}} = 0$ for any number of segments is given by τ, the transverse magnetization evolves an amount

$$\Phi = \delta\tau \tag{3.9}$$

between subpulses, where δ is a constant frequency offset. In the fully segmented pulse, these phases are identical for all pulse segments, whereby their effects are cancelled perfectly. For any other number of segments, the phase offset results in additional phase offsets in k-space. This gives an imperfect cancellation of transverse magnetization for off-resonant spins.

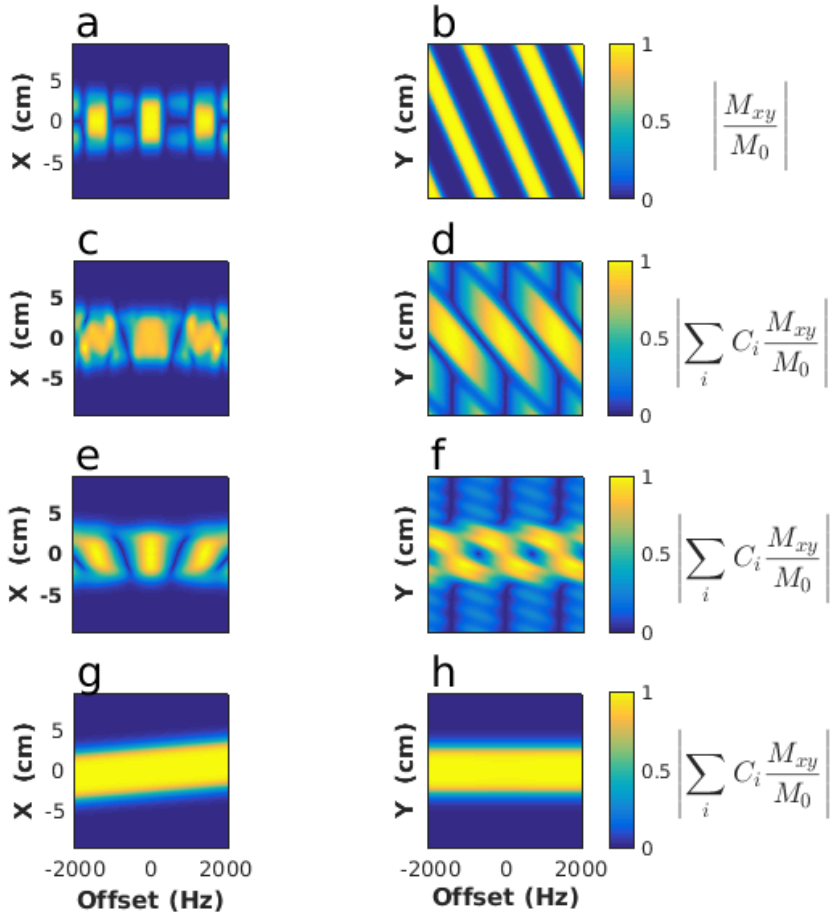

Fig. 3.5. Excitation profile behavior for various frequency offsets and number of pulse segments. a) Normalized transverse magnetization profile along the fast dimension versus a constant frequency offset when traversing all of k-space in a single shot. Note the rapid degradation of the profile with small offsets. b) The profile along the slow spatially-selected dimension versus a constant offset. Sidebands are intense and near the center band. c) With 2 segments defining the pulse, the profile in the fast dimension versus a constant offset is beginning to improve, while in d) the sidebands in the slow dimension are still prominent. e) Using 7 segments to define the pulse, the fast dimension has improved further. f) With 7 segments, the sidebands in the slow dimension are noticeably diminished in amplitude. g) With the fully segmented pulse, the profile simply shifts in physical space with a constant offset in the fast dimension, while in h), there is no dependence on constant offsets in the slow dimension. Rows 1-4 use the respective k-space trajectories shown in Figs. 2a 2d. The complex transverse magnetization is given by $M_{\mathrm{xy}} = M_{\mathrm{x}} + jM_{\mathrm{y}}$ and the coefficients C_i are defined in the text as (3.6).

3.4 Materials and Methods

All experiments were performed with a Varian DirectDrive console (Agilent Technologies, Santa Clara, CA) interfaced with a 4T, 90-cm magnet (Oxford Magnet Technology, Oxfordshire, UK) and a clinical gradient system (model SC72, Siemens, Erlangen, Germany). The maximum slew rate available on this gradient system is 100 mT/m/ms. Experimental verifications of the fully segmented and single-shot imaging sequences were performed using the pulse parameters described in the simulations section. A protocol approved by our institutions IRB was followed for human brain imaging of healthy volunteers after written, informed consent was obtained.

Gradient pre-emphasis for the fast gradient direction was performed using the gradient impulse response function (GIRF) [44], which is measured by using triangular gradient waveforms of varying width and amplitude on each gradient channel to fully sample the GIRF in the frequency domain. Gradient waveforms were measured following a protocol similar to Stich et al. [45], where 12 triangular waveforms were employed with amplitudes distributed linearly from 0.3125 G/cm to 3.75 G/cm. The slew rate of each waveform was set to 0.9 times the maximum possible to minimize waveform errors from the gradient amplifiers. The offset slice method [46] was used to measure the waveforms. In this method, a single 1-mm thick slice was offset 1.5 cm from isocenter for each gradient channel. The readout bandwidth was 50 kHz and the total readout time was 17 ms to obtain a spectral resolution of 58.82 Hz. Thirty averages were used with TR = 6 s and TE = 13.83 ms. Gradient pre-emphasis was necessary to prevent Nyquist ghosting of the excitation profile which results when there is a mismatch in sampling of $k = 0$ between the positive and negative gradient polarities.

Due to the longer minimum TR necessary for the single-shot excitation, T_2^*-weighted imaging was performed with this sequence, using a flip angle of 15°, TR/TE = 41.5 ms/25 ms with one average. The total single-shot pulse length was 23.704 ms. The receiver bandwidth was set at 100 kHz. Using the same total acquisition time, a full brain image was acquired at 1.6 mm isotropic resolution with a FOV = 192 x 192 x 192 mm^3. Identical sequence settings were used with the single-shot pulse to demonstrate spatial selectivity, followed by a sequence which zoomed on the selected

region. The isotropic resolution of this zoomed experiment was 800 m with a FOV = 192 x 96 x 96 mm^3 with the same total imaging time of 7.6 minutes.

A demonstration of B_1^+ compensation was performed using the single-shot sequence on a uniform agar phantom and a quadrature surface coil for excitation and reception. The B_1^+ profile was measured using the double angle method (DAM) [47], while the B_1^- map was measured using an adiabatic half passage excitation followed by two adiabatic full passages for refocusing. Each of these pulses was operated with sufficient RF power to be in the adiabatic regime. Reconstructed images were divided by the B_1^+ map where there was sufficient signal to divide by. This level was taken as 10% of the maximum image intensity in the B_1^+ map.

For the fully segmented sequence, a 3D T_1-weighted GRE sequence was used with TR/TE = 6.09 ms/2.76 ms, flip angle = 10.4°, and receiver bandwidth = 100 kHz. Isotropic resolution of 1.5 mm^3 was used, with a FOV = 192 x 96 x 96 mm^3. To demonstrate robustness to B_0 inhomogeneity, an additional experiment was performed in which one linear gradient was held fixed throughout the duration of the imaging sequence. A B_0 map was measured for a single slice, which demonstrated the constant gradient resulted in approximately 16.66 kHz over 19 cm in the slow-selected direction of the pulse.

3.5 Results

The surface coil experiment provided an extreme case of B_1 inhomogeneity for demonstrating B_1^+ compensation. The relative improvement in the excitation profile can be seen in Fig. 3.6, where the results of the compensated and uncompensated pulses are shown after dividing by the B_1^- map. The lower flip angle in the B_1^+ compensated image is due to a lower average RF power in the compensated pulse when using the same peak power.

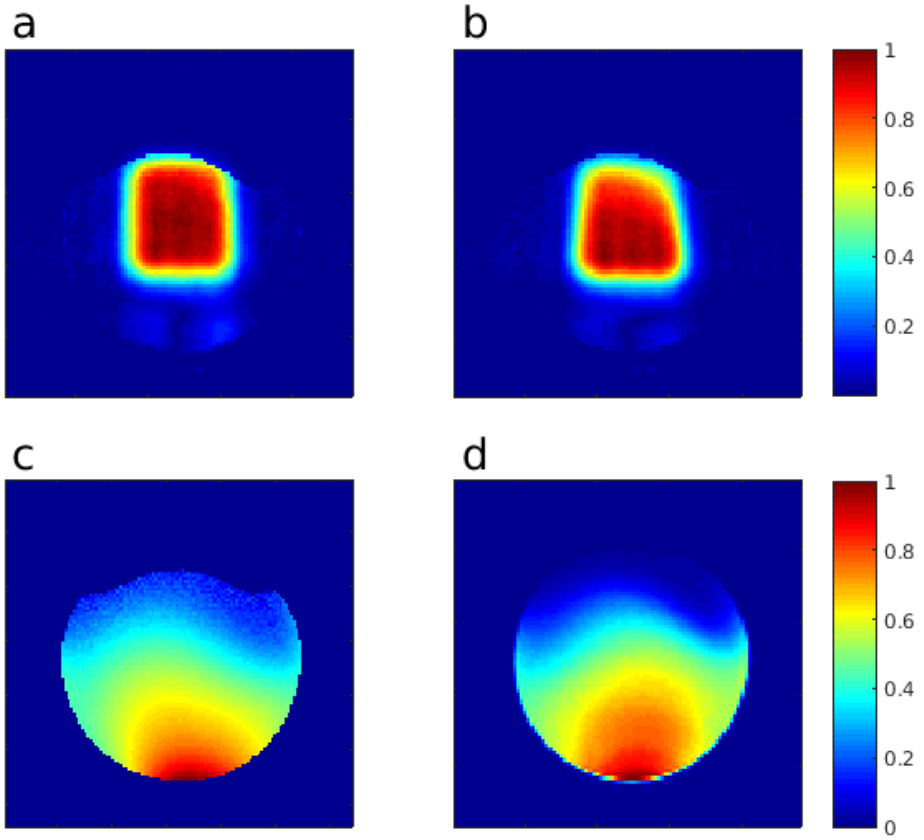

Fig. 3.6. Experimental demonstration of the B_1^+ compensation method described in the text. a) Excitation profile obtained using the B_1^+-compensated pulse. b) Excitation profile obtained using the original pulse. Both a) and b) have been divided by the receive coil sensitivity shown in (d), which was measured using the sequence described in the text. c) Transmit (B_1^+) map measured using the double angle method.

Selected cross sections from 3D brain images obtained with the single shot and fully segmented pulses are shown in Figs. 3.7 and 3.8, respectively. The single-shot pulse was used for excitation in a T_2^*-weighted sequence while the fully segmented pulse was used in a T_1-weighted sequence. The fully segmented version yields the most well-defined excitation profile, since it is essentially immune to off-resonance effects. This is clearly seen in the images collected with a constant gradient on during the sequence, where the excited profile is nearly identical to that obtained in a homogeneous field.

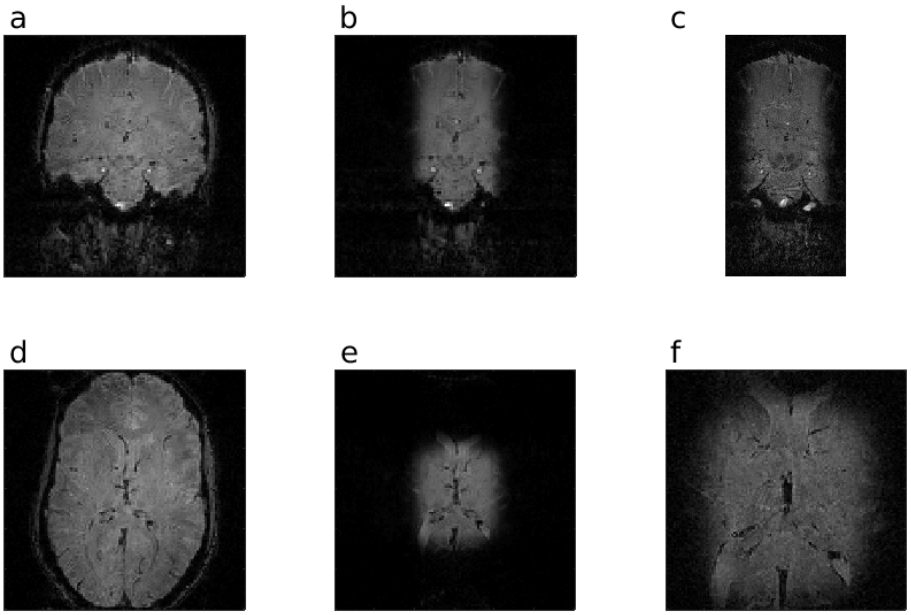

Fig. 3.7. In vivo brain images obtained with a 3D T_2^*-weighted GRE imaging sequence, using TR = 41.5 ms, TE = 25 ms, and flip angle = 15°. a - c) Coronal cross sections. d - f) Axial cross sections. a,d) FOV = 192 x 192 mm^2, isotropic resolution of 1.6 mm^2, with a non-selective excitation. b,e) FOV = 192 x 192 mm^2, isotropic resolution of 1.6 mm^2, with single-shot 2D HS1 excitation. c,f) FOV = 192 x 96 mm^2, isotropic resolution of 0.8 mm^2, with single-shot 2D HS1 excitation.

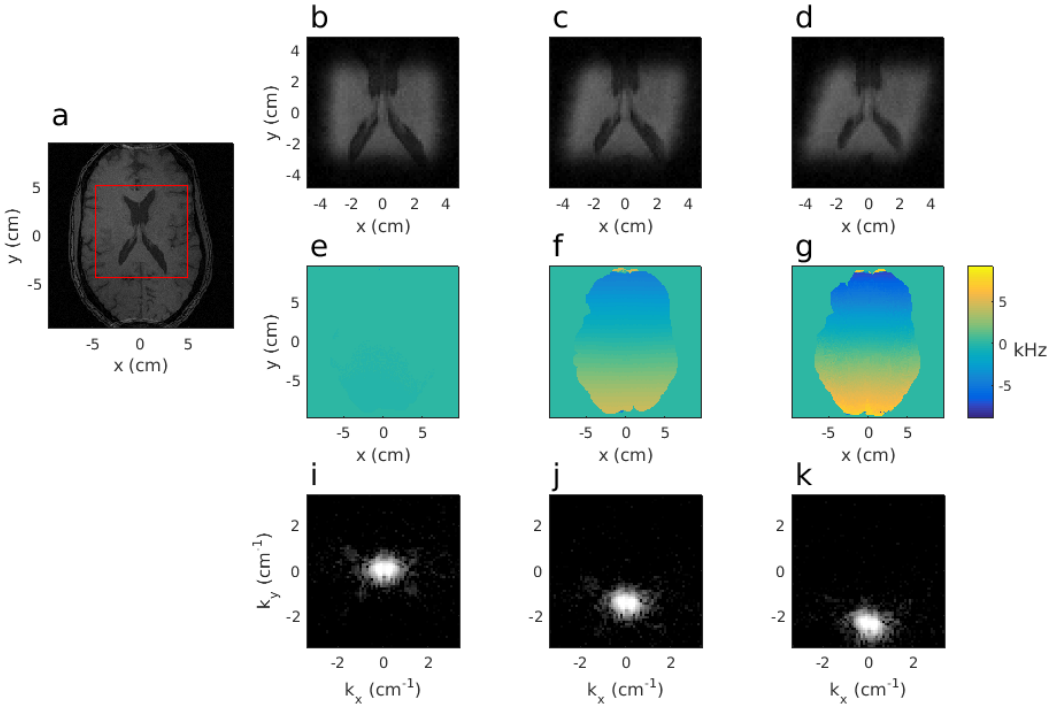

Fig. 3.8. Brain images obtained with a T_1-weighted 3D GRE acquisition. Sequence parameters were TR = 6.09 ms, TE = 2.76 ms, and flip angle = 10.4°. a) A single plane is shown from this dataset. The red box depicts the zoomed FOV used for (b d). The in-plane resolution of this cross section is 1 mm^2 and FOV = 192 x 192 mm^2, while the through-plane resolution was 1 mm. b) The same sequence parameters as (a) except a fully segmented pulse was used for excitation. The in-plane resolution of this cross section is 1.5 mm^2 and FOV = 96 x 96 mm^2, while the through-plane resolution was 1.5 mm. The B0 map for this case is shown in e). c) The same as (b), except the acquisition was performed in the presence of a constant field inhomogeneity created by turning on a gradient in the y-direction and leaving it on for the duration of the sequence. The measured B_0 for this dataset is given in f). In d), the gradient was set even higher, creating a frequency variation of approximately 16.66 kHz across the brain in the slow dimension of the pulse. The corresponding B_0 map is given in g). Note that all B_0 maps are shown on the same scale to demonstrate the magnitude of the inhomogeneity. This obscures the small fluctuations in (e) as they are significantly smaller than those in (f) and (g). In both (c) and (d), the static gradient in the slow dimension causes a change in orientation of the gradient during excitation, resulting in a tilted profile. i) k) The log-scale Fourier domain of the data shown in (b d), respectively. Note how there is no additional signal loss from the constant gradient, but only a shift in k-space.

3.6 Discussion and Conclusions

Single-shot multidimensional pulses require long pulse lengths, which decreases their bandwidth. Herein, we have shown how undersampling a multidimensional pulse by segmenting it and adding the resultant segments together after data collection permits shorter pulses, in turn leading to higher bandwidths. To the best of our knowledge, this work describes the first experimental implementation of a frequency-swept pulse in a multi-shot (segmented) form, whereas only amplitude-modulated pulses have been implemented in segments previously ([48], [49], [50]). The method of segmenting a 2D EPI excitation trajectory was first proposed by Panych et al. [48], while the first segmented pulses were interleaved spirals [50]. Previously, segmented 3D pulses have been shown to be useful in 2D MRI for slice selection and B0 compensation [49]. In the segmentation method of Panych et al. [48], a 2D excitation profile was defined using a segmented EPI k-space trajectory with B_1 amplitudes given by the Fourier transform of the desired excitation shape. To obtain consistent T_1 contrast, an equal flip angle was assumed to be produced by every pulse segment without rescaling the RF power used for transmitting each segment. This condition cannot be satisfied when using shaped pulses. That work also did not focus on the use of a segmented 2D EPI trajectory to increase the pulse bandwidth, as done herein. Finally, previously described segmented pulses ([48], [49], [50]) do not permit the herein described method of B_1^+ compensation since they are not FM pulses.

Although the imaging experiments presented demonstrate only the single-shot and fully segmented cases, it should be noted that any number of segments can be used to fully sample the pulse. However, use of an integer divisor of the number of lines of k-space is recommended, so that the number of subpulses, the subpulse length, and the total pulse length are all equal between segments. If this condition is not met, care must be taken to ensure TR and TE are maintained between segment acquisitions. It should be noted that diffusion effects may differ between segments outside of this recommended pulse design regime. Also, while here the pulse shapes along both directions were HS1 pulses, this need not be the case. For example, a sinc pulse could be used for modulation in the slow dimension.

Although not demonstrated in the experiments, this 2D HS1 pulse which sam-

ples k-space on a Cartesian grid can be used to invert magnetization in an adiabatic manner, provided $B_{1,\max}$ is above the threshold needed to satisfy the adiabatic condition. Here, $B_{1,\max}$ denotes the peak B_1 of the pulse. Conversely, the previously described 2D HS1 pulse of Jang et al. [39] which utilizes a spiral k-space trajectory cannot achieve adiabaticity, regardless of the $B_{1,\max}$ value. A juxtaposition of the Cartesian k-space trajectory described herein with the spiral trajectory of Jang et al. [39] helps to elucidate how the different trajectories through the pulses k-space determine the magnetization profile with respect to frequency offset for a specific k-space weighting function, such as the 2D HS1 pulse. For the Cartesian sampling scheme, the pulse behaves adiabatically using the single-shot trajectory, due to the adiabatic frequency sweep in the slow dimension. The subpulses are frequency swept, but by themselves are not necessarily functioning adiabatically. Unfortunately, when the 2D k-space trajectory is segmented, the pulse cannot function adiabatically because the segmentation process creates discontinuities in the frequency sweep. For this reason, a segmented 2D HS1 pulse is not useful for adiabatic inversion, while the single-shot pulse is practical for such purposes.

When driven sub-adiabatically (e.g. for excitation), there exists a unique method to compensate for B1+ inhomogeneity. This method is that used by Jang et al. [39], where the pulse is compensated along the trajectory of a moving vertex in physical space. Note again that this method of compensation cannot be achieved with amplitude-modulated 2D pulses since a vertex trajectory cannot be created. It is unique to multidimensional FM pulses.

Upon inspection of the results of the fully segmented pulse (see Fig. 3.8), no noticeable loss of signal can be seen despite the large increase in B_0 inhomogeneity imposed by the constant gradient field. The inhomogeneity merely shifts the position of the acquired data in k-space and produces a tilt in the excitation profile. Provided the acquisition k-space shift does not preclude a large amount of the signal energy from being sampled, no significant signal loss occurs. This condition is met provided the shift is smaller than $k_{\max}$, the largest acquisition k-value sampled. Hence, for a given resolution Δx and echo time T_E, the following must be satisfied

$$k_{\text{shift}} = \gamma G_\Delta T_E < k_{\max} = \frac{1}{2\Delta x} \tag{3.10}$$

where G_Δ is a constant linear field inhomogeneity. This equation should hold true for non-linear inhomogeneous fields as well. In that case, G_Δ is the local field gradient and G_Δ is a function of x (i.e $G_\Delta(x)$). That is, the k-space center position varies depending on the location of each isochromat in space.

By virtue of its hyperbolic phase profile, this pulse has potential applications in xSPEN MRI [51], [52]. In that method, a hyperbolic phase profile permits an acceleration of data acquisition by utilizing the correlation between k-space and image space when a hyperbolic or parabolic phase profile is present. These correlations exist due to the localization of signals originating from the vertex of the phase profile. Hence, the k-space signal appears as a transposed, low-resolution version of the resulting image. This approach was not taken in the present work since the gradient slew rate limitations precluded the use of high time-bandwidth products while maintaining a reasonable pulse length.

In summary, the combination of the features discussed thus far makes 2D frequency-swept pulses an attractive candidate when resilience to large B0 and B1+ field inhomogeneities is needed. To increase the bandwidth further in the future, parallel transmission techniques [53], [54] might be employed to further decrease the pulse length and drive up the bandwidth.

Chapter 4

Accelerating Imaging with Segmented 2D Pulses using Parallel Imaging and Virtual Coils

This work has been accepted for publication in the Journal of Magnetic Resonance [55].

4.1 Introduction

Previous work has shown how the k-space trajectory of a multidimensional radiofrequency (RF) pulse [33], [39], [48], [50], [49] can be segmented and acquired in separate shots. In the absence of segmenting, multidimensional RF pulses suffer from a low bandwidth due to the long pulse lengths necessary for full sampling. Undersampling of excitation k-space permits a shorter pulse length and increased pulse bandwidth; however, in MRI applications of segmented 2D and 3D pulses, the need to fully sample acquisition k-space per excitation segment leads to longer scans, since the imaging time increases linearly with the number of pulse segments used. This requirement decreases the utility of this approach. Alternatively, as described by Norris et al. [56], the effective bandwidth can be increased by multiplying the pulse by a Dirac comb. By this approach, the effective bandwidth increases due to the

production of sidebands, which may not be ideal for certain applications such as 3D inner volume imaging.

Segmenting multidimensional pulses is useful whenever multidimensional localization is desired with robustness to B0 inhomogeneity. Examples include localized spectroscopy [50], [57], [58] and inner volume imaging [59], [60]. For sequences with an EPI readout, the reduced field-of-view (FOV) resulting from using a multidimensional pulse permits shorter echo-trains, thereby diminishing distortions in regions with large susceptibility differences [60]. Segmenting the excitation pulse in these cases would increase the excitation bandwidth, yielding a more robust excitation profile.

Signals produced by each excitation segment contain independent information although the same object is being imaged while using the same transmit and receive coil(s). This is due to various spatial phases resulting per excitation with the different pulse segments. In previous work [33], the acquired data for all pulse segments were fully sampled prior to a weighted, complex summation of the data. Here, it is shown that the redundancy between pulse segments permits data undersampling in the phase-encoded dimension aligned with the segmented dimension of the pulse. The data can then be reconstructed using Generalized Autocalibrating Partially Parallel Acquisitions (GRAPPA) [25] and potentially other parallel imaging techniques. This approach is made possible by treating the data from each pulse segment as if received by a virtual coil with a spatially dependent sensitivity map. The total number of virtual coils is then equal to the number of excitation segments used, provided there is only one receive coil.

Blaimer et al. [61] originally introduced the notion of virtual coils, although in that work, the virtual coils were generated in an undersampled Cartesian acquisition by treating synthetic, conjugated data as if originating from a virtual coil. A similar approach to accelerate acquisition when using more than one type of excitation was taken by Orzada et al. [62], using a technique named Time Interleaved Acquisition of Modes (TIAMO). There, the transmit coil was driven in two different excitation modes, with the data being undersampled on acquisition for both modes and reconstructed using GRAPPA. This resulted in two virtual receive coils. In the new method described here, the transmit coil operates in the same excitation mode for

all pulses, instead using undersampled pulse segments for additional spatial encoding to accelerate data acquisition. The current work also permits a zoomed FOV in two dimensions. However, the reconstruction frameworks of the two approaches are similar, with some differences that will be thoroughly discussed in the next section and in the discussion.

4.2 Theory

When using a 2D RF pulse that has been segmented to achieve increased excitation bandwidth, the FOV can be reduced in the two spatially-selected dimensions, as with the fully-sampled, single-shot 2D pulse. To avoid an increase in imaging time, previous work [33] relied on the condition that the number of pulse segments not exceed the acceleration gained by using a reduced FOV. This condition is no longer strictly necessary, as the different pulse segments induce their own spatial modulation. The data from each excitation segment are then used to synthesize unsampled data in an accelerated acquisition. This concept is motivated by considering the excitation profile following a given pulse segment and the signal received following that excitation, neglecting relaxation effects. Assuming a small tip angle excitation [21], the magnetization profile $P(\vec{r})$ of the imaged object $I(\vec{r})$ following pulse segment j is given by

$$P_j(\vec{r}) \propto i\,\gamma\,I(\vec{r}) \int_0^{\mathrm{T_p}} B_{1,j}^{+}(\vec{r},t)\,\exp(i\,\vec{k}_j(t)\cdot\vec{r})\,dt. \tag{4.1}$$

Here, $B_{1,j}^{+}(\vec{r},t)$ is the total complex RF field at position $\vec{r}$ and time t, γ is the proton gyromagnetic ratio, $\mathrm{T_p}$ is the RF pulse duration, and $\vec{k}_j(t)$ is a parameterized trajectory through excitation k-space for pulse segment j. The index j runs from 1, ..., N_s, where N_s is the number of pulse segments used. Using the separability in space and time of the transmit field, that is, $B_{1,j}^{+}(\vec{r},t) = B_{1,j}^{+}(\vec{r})B_{1,j}^{+}(t)$, Eq. 4.1 can be rewritten as

$$P_j(\vec{r}) \propto i\,\gamma\,I(\vec{r})B_{1,j}^{+}(\vec{r}) \int_0^{\mathrm{T_p}} B_{1,j}^{+}(t)\,\exp(i\,\vec{k}_j(t)\cdot\vec{r})\,dt. \tag{4.2}$$

The result of the integral is a function of position $\vec{r}$ only, so Eq. (4.2) can be rewritetn as

$$P_j(\vec{r}) \propto i\,\gamma\, I(\vec{r}) B_{1,j}^{+}(\vec{r}) M_j(\vec{r}), \tag{4.3}$$

where

$$M_j(\vec{r}) \triangleq \int_0^{\mathrm{T_p}} B_{1,j}^{+}(t) \exp(i\,\vec{k}_j(t)\cdot\vec{r})\,dt. \tag{4.4}$$

Now consider the signal, $S_(m,j)$, received in coil m following excitation by pulse segment j during signal acquisition. The index m is in the range 1, ..., N_c, where N_c is the number of physical coils used. When using a spatially dependent receive field $B_1^{-}(\vec{r})$, the signal can be written as

$$S_{m,j}(\vec{k}_a(t)) \propto \int_V B_{1,m}^{-}(\vec{r})\, P_j(\vec{r}) \exp(-i\,\vec{k}_a(t)\cdot\vec{r})\,dV. \tag{4.5}$$

The subscript a denotes acquisition, and the integral is performed over the sensitive volume V of the receive coil. Inserting the definition of P_j from Eq. (4.3), the signal is recast as

$$S_{m,j}(\vec{k}_a(t)) \propto i\,\gamma \int_V B_{1,m}^{-}(\vec{r})\, M_j(\vec{r})\, B_{1,j}^{+}(\vec{r})\, I(\vec{r}) \exp(-i\,\vec{k}_a(t)\cdot\vec{r})\,dV. \tag{4.6}$$

By defining a spatially dependent quantity as

$$\tilde{B}_{m,j}(\vec{r}) \triangleq i\,\gamma B_{1,j}^{+}(\vec{r})\, B_{1,m}^{-}(\vec{r})\, M_j(\vec{r}), \tag{4.7}$$

the signal equation becomes

$$S_{m,j}(\vec{k}_a(t)) \propto \int_V \tilde{B}_{m,j}(\vec{r})\, I(\vec{r}) \exp(-i\,\vec{k}_a(t)\cdot\vec{r})\,dV. \tag{4.8}$$

From Eqs. (4.7) and (4.8), the quantity $\tilde{B}_{m,j}$ can clearly be interpreted as a complex coil sensitivity profile. As discussed in [62], this is equivalent to assuming homogeneous excitation followed by Fourier and sensitivity encoding. Here, however, the virtual coil profile is the product of the physical receiver sensitivity, transmit field map, and pulse segment excitation profile, which distinguishes it from TIAMO. There,

the virtual profile is the product of the physical receive sensitivity and transmit field map only. It is immediately apparent that even when only one physical receive coil is present, there are still N_s virtual coils to work with. When an N_s-segment pulse is combined with standard GRAPPA, the data from each pulse segment acquired with one physical coil can be split into N_s virtual coil data sets. Hence, the number of effective coils, $\tilde{N}_c$, is equal to the product $N_s N_c$, as seen from Eq. (4.7).

When using segmented pulses with N segments, Mullen et al. [33] noted the signal-to-noise ratio (SNR) for a N-segment pulse with respect to a single-shot pulse with N averages decreases as

$$\frac{\mathrm{SNR}_{\text{segmented}}}{\mathrm{SNR}_{\text{single-shot}}} = \frac{\sum_{j=1}^{N} |C_j|}{\sqrt{N \sum_{j=1}^{N} |C_j|^2}}, \tag{4.9}$$

with C_j

$$C_j = \max\Big| \int_0^{T_P} \omega_{1,j}(t) \exp\Big(- i\, \phi_{RF,j}(t)\Big) \exp\Big(i\, \vec{k}_j(t) \cdot \vec{r}\Big) dt \Big|. \tag{4.10}$$

Here, the subscript j denotes segment number and i the square root of -1. The C_j are weighting coefficients used in the pulse segment combination and were originally defined in [33]. Note that the equation presented previously omitted the term incorporating the k-space trajectory [34]. In Eq. 10, each C_j is set equal to the maximum value of the integral across all space $\vec{r}$, but other scaling prescriptions could be used, such as the mean value of each segments magnetization profile.

When partially segmenting a 2D pulse, the flip angle at each spatial location varies from segment to segment, and the amount of variation is spatially dependent and increases with number of segments used, except when using the fully segmented pulse. With the commonly employed condition TR ¡¡ T1, variable T1-weighting of the different segments cannot be ignored. The coefficients Cj are thus used to scale the peak RF amplitude to obtain a more consistent flip angle across pulse segments. This procedure requires a processing step to compensate for the increased flip angles from scaling, so that signal outside the region of interest is perfectly cancelled when summing over segments. By scaling the amplitude of each pulse segment, flip angle

variations are minimized enough to avoid noticeable image artifacts.

However, undersampling the data using an effective acceleration R decreases the SNR by $\sqrt{R}$ relative to an unaccelerated acquisition [63]. Combining Eq. 4.9 with Eq. 5 of [63], the ratio of the SNR for a segmented 2D excitation, accelerated readout dataset to that of the equivalent sequence with a single-shot coverage of 2D excitation k-space and an unaccelerated readout is given by

$$\frac{\mathrm{SNR}_{\text{segmented,accelerated}}}{\mathrm{SNR}_{\text{single-shot,unaccelerated}}} = \frac{\sum_{j=1}^{N} |C_j|}{g\sqrt{R\,N\sum_{j=1}^{N} |C_j|^2}}, \tag{4.11}$$

where g is the g-factor map, an indication of noise amplification due to noise correlations.

4.3 Simulations

Simulations were performed to demonstrate the spatial modulation of transverse magnetization profiles of each pulse segment, which act as virtual coil profiles. For the first set of simulations, and in the experiments at 4T, identical excitation k-space parameters were used as in [33]. Therein, the 2D pulse was a 2D hyperbolic secant (HS1), with a time bandwidth product (TBP) equal to 9 in both dimensions, slab thickness = 5 cm, 28 total lines of excitation k-space, and subpulse durations of 700 s. With 4 excitation segments, each segment traversed 7 lines of excitation k-space, with the same initial direction for each segment. The second 2D pulse simulated, which was used experimentally at 3T, had the following parameters: $\mathrm{TBP}_{\mathrm{fast}} = 16$, $\mathrm{TBP}_{\mathrm{slow}} = 10$, and slab thickness in the slow and fast dimensions equal to 9 cm and 3.6 cm, respectively. A total of 20 lines of excitation k-space were sampled in the slow dimension, where each subpulse duration was 800 s. Excitation k-space was sampled on the gradient ramps using VERSE [64] to shorten the pulse duration further. As discussed in [33], the flip angle of each pulse segment must be kept the same to maintain consistent T_1 weighting. The peak transmit field, $B_1^{\max}$, to achieve the desired flip angle was determined by integration for each segment of the pulse. Data were recombined following the procedure in [33].

As can be seen in Fig. 4.1, in the case of the fully-segmented pulse with the pulse parameters used at 4T, the virtual coil profiles form a spatial-encoding basis set in one dimension, permitting higher undersampling factors in the segmented dimension of the pulse.

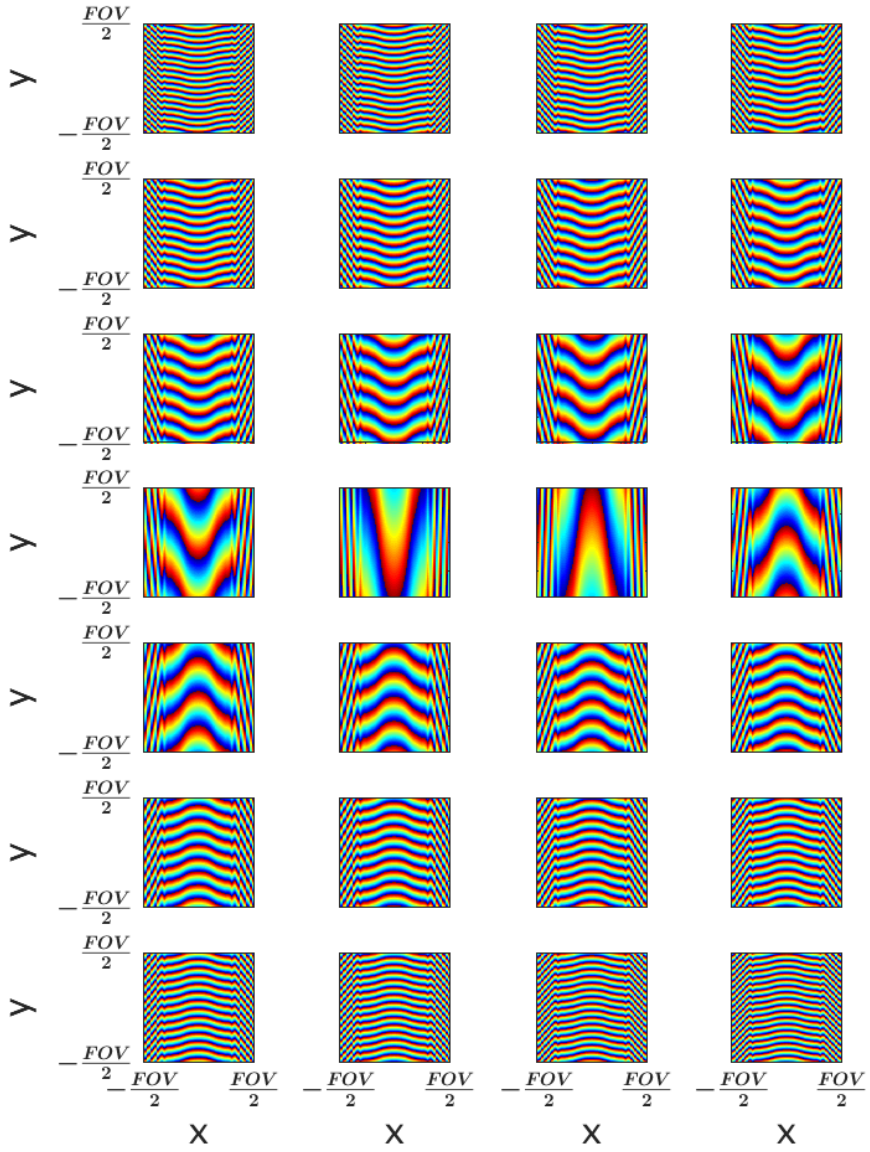

Fig. 4.1. The phase of the transverse magnetization for each of the 2D excitation segments when fully segmented into 28 pulse segments. The pulse parameters are described in the text. The x dimension is the fast (unsegmented) dimension of the pulse, while y is the slow(segmented) dimension of the pulse.

The phases of the transverse magnetizations produced with the 4-segment pulse are shown in Fig. 4.2. Although the spatial modulation of the magnetization phase in

this case is less than that of the fully segmented case, the spatial modulation afforded is sufficient to permit a limited amount of acquisition undersampling.

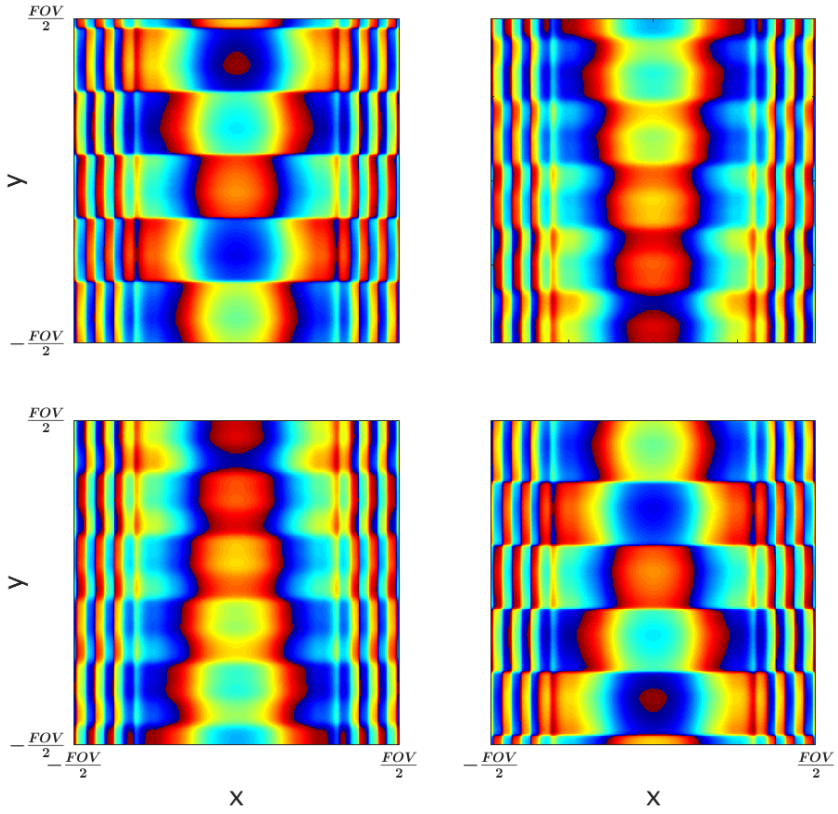

Fig. 4.2. The phase of the transverse magnetization for each of the 2D pulse segments when traversed in 4 segments.

To evaluate off-resonance effects for both 4-segment pulses used in experiments, the excitation profiles were simulated over a range of constant frequency offsets using an in-house Bloch simulator. These results are presented in Fig. 4.3. The excitation profile in the fast dimension (x) of the pulse is clearly improved, while this is not evident in the slow dimension (y) of the pulse. For the 4-segment pulse used at 3T, the behavior in the slow dimension of the pulse is worse than for the 4-segment pulse at 4T due to using a lower k_{max} in the slow dimension of the pulse, by nearly a factor of two. This leads to a higher sensitivity to off-resonance effects. Equivalent simulations

for the fully segmented pulse are simulated and discussed in detail elsewhere [33].

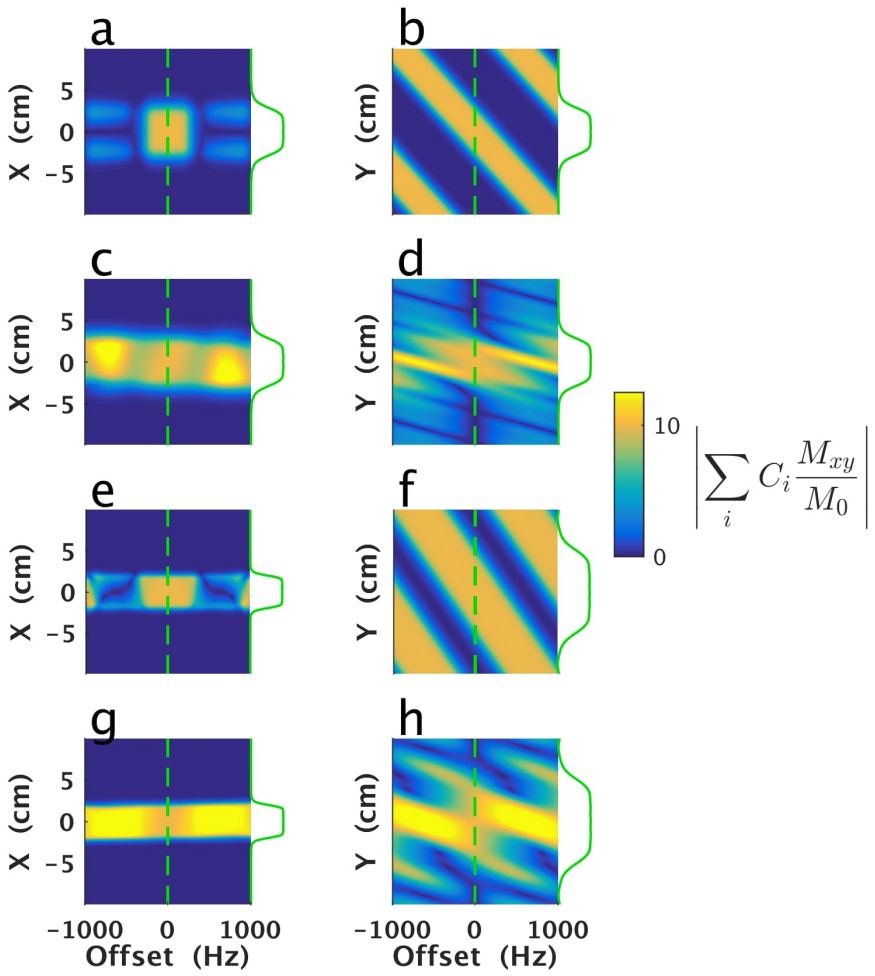

Fig. 4.3. Simulated excitation profiles produced by the 2D pulses used in experiments at 4T (a-d) and 3T (e-h), when performed without (a,b,e,f) and with segmentation (c,d,g,h). In all cases, the relative magnitude of the transverse magnetization is displayed as a function of position (x or y) versus resonance offset, for the case of flip angle equal to 10° on resonance. As can be seen, the shape of the on-resonance excitation profile (green) is invariant with pulse segmentation. Coefficients C_i used in combining the data from the 4 shots (segmented pulses) are as defined in [33].

4.4 Materials and Methods

The performance of the 2D pulse acceleration method was tested in human brain imaging experiments using 4T Varian and 3T Siemens MRI scanners. The different RF hardware of these MRI systems (i.e., the different numbers of receiver coils and channels) allowed the acceleration method to be tested without (4T) and with (3T) conventional parallel acquisition. A protocol approved by our Institutional Review Board (IRB) was followed for human brain imaging of healthy volunteers after obtaining written, informed consent. All scans were performed using the pulse segments as the outermost loop of the acquisition. That is, the k-space data were fully sampled for a given pulse segment before acquiring data for subsequent segments.

4T experiments:

Two experiments were performed with a Varian DirectDrive console (Agilent Technologies, Santa Clara, CA) interfaced with a 4T, 90-cm magnet (Oxford Magnet Technology, Oxfordshire, UK) and a clinical gradient system (model SC72, Siemens, Erlangen, Germany). Experimental verification of the fully segmented and 4-segment imaging sequences was performed using the same pulse parameters as in [33] and as discussed in the Simulations section. Two experiments were performed to demonstrate the method at different levels of pulse segmentation. Both of these experiments were performed with a single channel transmit, single channel receive RF coil, with Cartesian acquisition trajectories.

Gradient pre-emphasis was necessary on this system to prevent Nyquist ghosting of the excitation profile, which occurs when the positive and negative gradient lobes do not sample evenly about the center of k-space. Gradient pre-emphasis for the fast gradient was performed using the gradient impulse response function (GIRF) [44]. Therein, multiple triangular gradient waveforms of varying width and amplitude are measured on each gradient channel to fully sample the GIRF in the frequency domain. Gradient waveforms were measured following a protocol similar to Stich et al. [45], although here, 12 triangular waveforms were employed with amplitudes distributed linearly from 0.3125 G/cm to 3.75 G/cm. The slew rate of each waveform was set to 0.9 times the maximum possible to minimize waveform errors from the gradient

amplifiers. The offset slice method [46] was used to measure the waveforms. In this method, a single 1-mm thick slice was offset 1.5 cm from isocenter for each gradient channel. The readout bandwidth was 50 kHz and the total readout time was 17 ms to obtain a spectral resolution of 58.82 Hz. Thirty averages were used with TR = 6 s and TE = 13.83 ms.

For the fully segmented sequence, a 3D T_1-weighted, spoiled GRE sequence was used with TR/TE = 6.09 ms/2.76 ms, flip angle = 10.4 degrees, and receiver bandwidth = 100 kHz. Isotropic resolution of 1.5 mm^3 was used, with a FOV = 192 x 96 x 96 mm^3. The data acquired with 2D excitation were fully sampled experimentally and downsampled retrospectively to facilitate a comparison of SNR. The acquisition time for the fully sampled dataset was approximately 11.64 minutes, while acquisition time for the accelerated readout would be approximately 1.59 minutes. For comparison, a non-selective excitation was used with FOV = 192 x 192 x 192 mm^3, matrix size 192 x 192 x 192, while keeping the same TR, TE, flip angle, and acquisition bandwidth used in experiments deploying 2D pulses. The GRAPPA kernel was 3 x 2 x 3 in k_x, k_y, and k_z, respectively. Every 11th line of acquisition k-space was sampled in the slow dimension of the pulse, which was phase encoded on readout. The center 6 x 32 lines of k-space were fully sampled in the phase-encoded dimensions (k_x and k_y) for use as autocalibrating signals (ACS). An elongated rectangle was employed to capture the maximal amount of signal energy for each pulse segment. The peak signal shifts in the slow dimension of the pulse when comparing different segments, and the shape of the ACS region was designed to account for this. The ACS lines were used in the final reconstruction. The acceleration per pulse segment is $R = 7.341$ with the sampling pattern discussed and shown in Fig. 4.4.

For the 4-segment excitation sequence, a 3D T_2^*-weighted, spoiled GRE sequence was performed using a flip angle of 10°, TR/TE = 41.5 ms/25 ms with one average. The receiver bandwidth was set at 100 kHz. Isotropic resolution of 1 mm was used, with a FOV = 192 x 96 x 96 mm^3. Again, data were fully sampled experimentally and undersampled in processing. The acquisition time for the fully sampled dataset was about 25.50 minutes and about 13.55 minutes for the undersampled readout. A reference image was acquired with the same TR, TE, flip angle, and bandwidth, but with FOV = 192 x 192 x 192 $mm^3$and 1 mm isotropic resolution. The GRAPPA

kernel was again 3 x 2 x 3 in kx, ky, and kz, respectively, where every 3rd line of acquisition k-space was sampled in the slow dimension of the pulse. The center 40 lines of k-space were fully sampled in both phase-encoded dimensions for use as ACS data which were again used in the final reconstruction. The acceleration per segment in this case is $R = 1.882$, and the sampling pattern is shown in Fig. 4.5.

Noise prescans were measured at 4T using the same gain and receiver bandwidth as their respective imaging sequence, following the procedure in [65]. To obtain an accurate approximation of the noise standard deviation, 10^4 complex points were acquired in the absence of RF pulses. This yields an estimate of the noise standard deviation which is accurate to 1%, as described by Robson et al. [63]. As the pulse segments were acquired sequentially in time, there is no noise correlation between pulse segments. The pseudo-replica method [63] was used with 256 pseudo-replicas to calculate SNR and g-factor maps. The GRAPPA kernel weights were calculated once for the original undersampled k-space data and used in all following pseudo-replica images. For validation of the pseudo-replica results, the g-factor maps were also calculated using the method of Breuer et al. [66], where the g-factor is calculated directly from the GRAPPA kernel. The g-factors were compensated according to Eq. 13 of [66] to account for using the ACS data in the final reconstructions.

3T experiments:

Another experiment was performed on a 3T Siemens Prisma scanner using a 32 channel head coil. A 2D HS1 pulse was designed using the second set of parameters presented in the Simulation section. This pulse was used for excitation in a 3D GRE EPI sequence, where the phase-encoded dimensions were aligned with the spatially-selected dimensions of the 2D pulse. The sequence parameters were: TR/TE = 67 ms/19 ms, flip angle = 10°, FOV = 192 x 93 x 36 mm^3, and isotropic resolution of 1.5 mm. Data were fully sampled experimentally and undersampled in processing. The acquisition time for the fully sampled dataset was 12.9 seconds, while the acquisition time for the accelerated dataset would have taken approximately 5.412.58 seconds. Gradient preemphasis was not necessary on this system.

The same GRAPPA kernel size was used here as at 4T, but now every 5th line

of acquisition k-space was sampled in the slow dimension of the pulse. The central 16 lines of acquisition k-space were fully sampled in the phase-encoded dimension which was aligned with the segmented dimension of the pulse. All data along the fast dimension of the pulse was used as calibration data, as there were only 24 phase encodes in that direction. The ACS data were not used in the final reconstruction. The acceleration per segment in this case is $R = 5$, where the undersampling pattern is shown in Fig. 8. When combining the coil and pulse segment images, it is important to first perform a summation of the complex data over the pulse segments, since this combination is phase sensitive. The combination of coil data can then be performed in any desired manner, such as with sum-of-squares (SOS). In addition to using the pulse segments as virtual coils, reconstructions were also performed by first summing the pulse segments for each physical coil, followed by applying GRAPPA using only the physical coils for reconstruction.

4.5 Results

The results of a fully segmented pulse and 4-segment pulse at 4T are shown in Figs. 4.4 and 4.5, respectively. In both cases, a reference 3D gradient echo image is given with the same timing parameters and flip angle as the data using the associated 2D pulse. The direct Fourier reconstruction of the undersampled data is a low-resolution image dominated by the ACS energy. Using GRAPPA on the data from different pulse segments yields an image comparable in quality to the fully sampled reconstruction. For the 4-segment pulse, a small amount of residual blurring is visible around the periphery of the excitation profile.

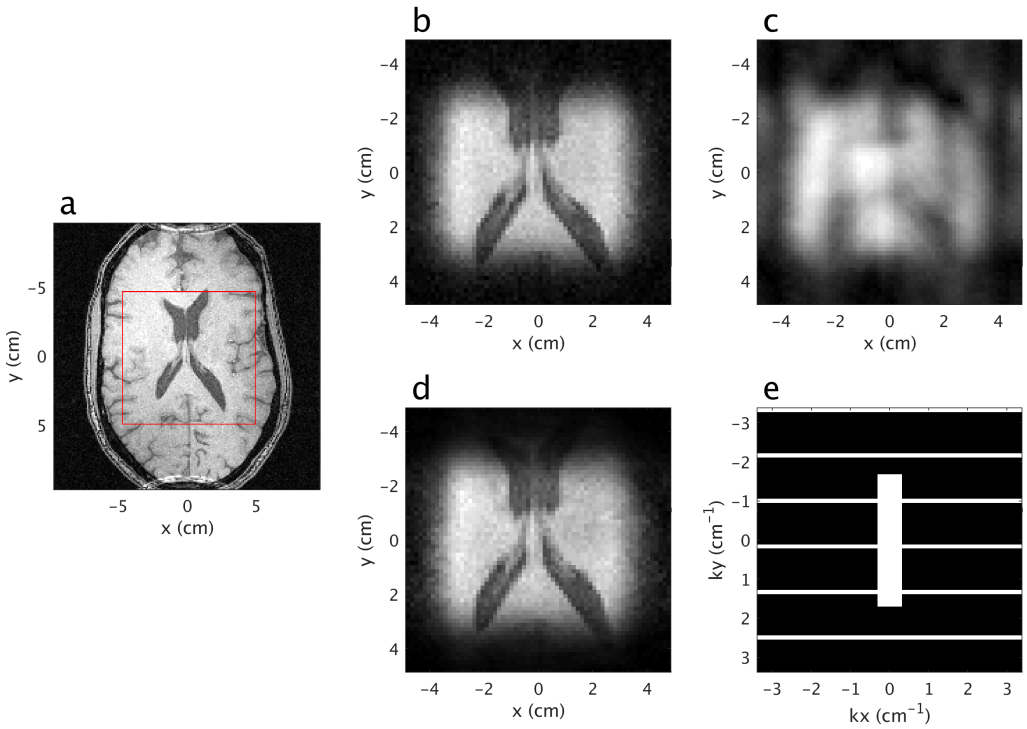

Fig. 4.4. Single plane from the 3D reconstructions of the fully segmented 2D HS1 pulse. Sequence parameters were TR = 6.09 ms, TE = 2.76 ms, FA = 10.4°, FOV = 96 x 96 x192 mm^3 with matrix size of 64 x 64 x 128. a) The sequence as described run with a non-selective excitation and FOV = 192 x 192 x 192 mm^3 and matrix size of 192 x 192 x 192, reconstructed using 3D FT. The red box indicates the zoomed FOV in the phase-encoded dimensions. b) FT reconstruction of fully-sampled image data excited by the segmented 2D pulse. c) FT reconstruction of undersampled image data, resulting in low resolution due to the center ACS region containing most of the signal energy. d) GRAPPA reconstruction of the undersampled image data. e) The retrospective undersampling pattern. White indicates sampled values, whereas black indicates unsampled.

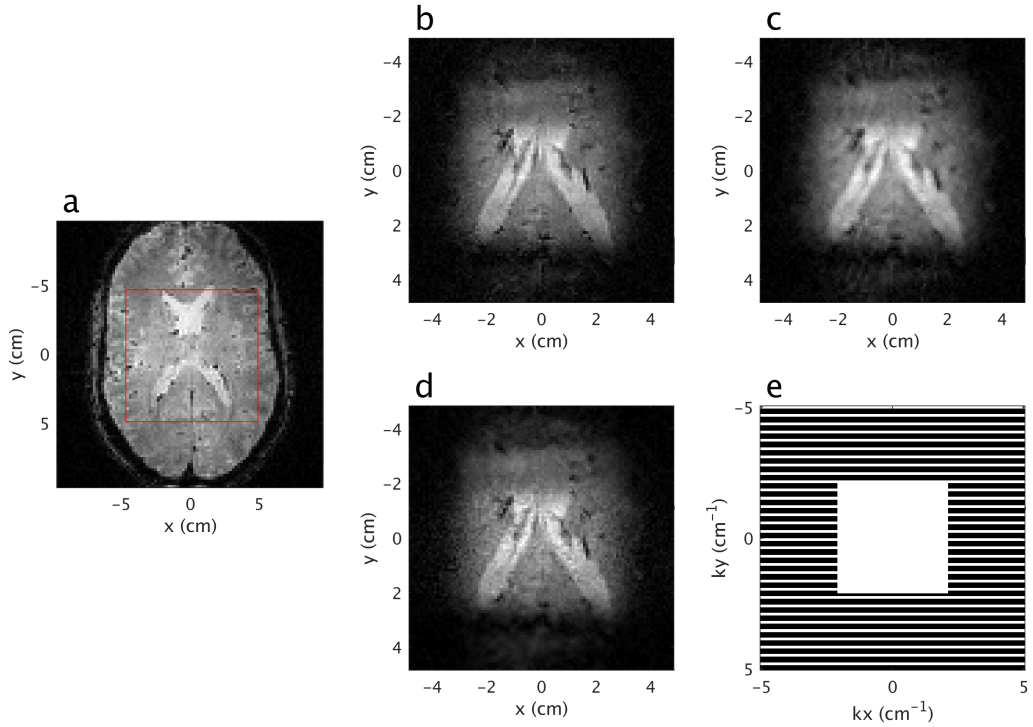

Fig. 4.5. Single plane from the 3D reconstructions of the 4-segment 2D HS1 pulse. Sequence parameters were TR = 41.5 ms, TE = 25 ms, flip angle = 10°, FOV = 96 x 96 x 192 mm^3 with matrix size of 96 x 96 x 192. a) Reference image acquired with a non-selective excitation and FOV = 192 x 192 x 192 mm^3 and matrix size of 192 x 192 x 192, reconstructed using 3D FT. The red box indicates the zoomed FOV in the phase-encoded dimensions. b) FT reconstruction of fully-sampled image data excited by the segmented 2D pulse. c) FT reconstruction of undersampled image data, resulting in low resolution due to the center ACS region containing most of the signal energy. d) GRAPPA reconstruction of the undersampled image data. e) The retrospective undersampling pattern. White indicates sampled values, whereas black indicates unsampled.

The SNR and g-factor maps for the fully segmented pulse are shown in Figure 4.6, while those for the 4-segment pulse are shown in Figure 4.7. There is a modest loss of SNR for both cases. The g-factor map for the fully segmented pulse is spatially uniform within the excitation band of the pulse. For the 4-segment pulse, the g-factor map is non-uniform in space, being largest near the center of the profile

and diminishing in magnitude near the edges of the profile in the slow dimension of the pulse. A discussion on the low values of the g-factor, particularly for the fully segmented pulse, is given in the Discussion section.

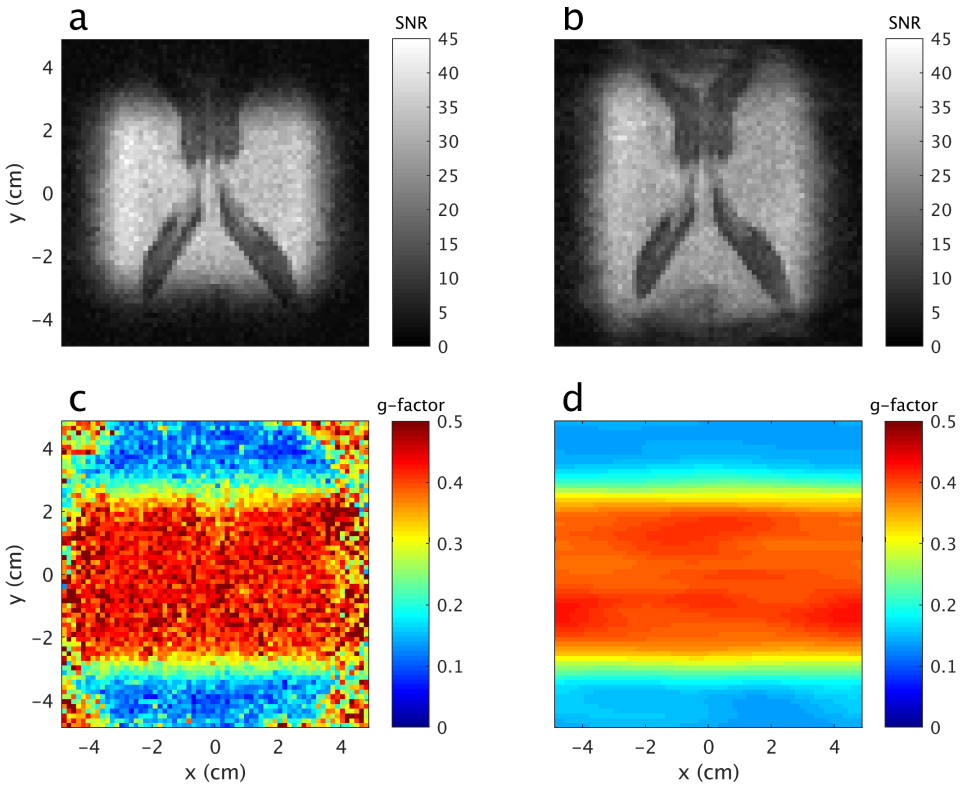

Fig. 4.6. SNR maps and g-factor map for the fully segmented excitation. a) SNR map for the fully sampled readout, excited with the fully segmented 2D HS1 pulse. b) SNR map for the undersampled data, showing a modest decrease in SNR. c) The g-factor map calculated by the pseudo-replica method. d) The g-factor map calculated directly from the GRAPPA kernel.

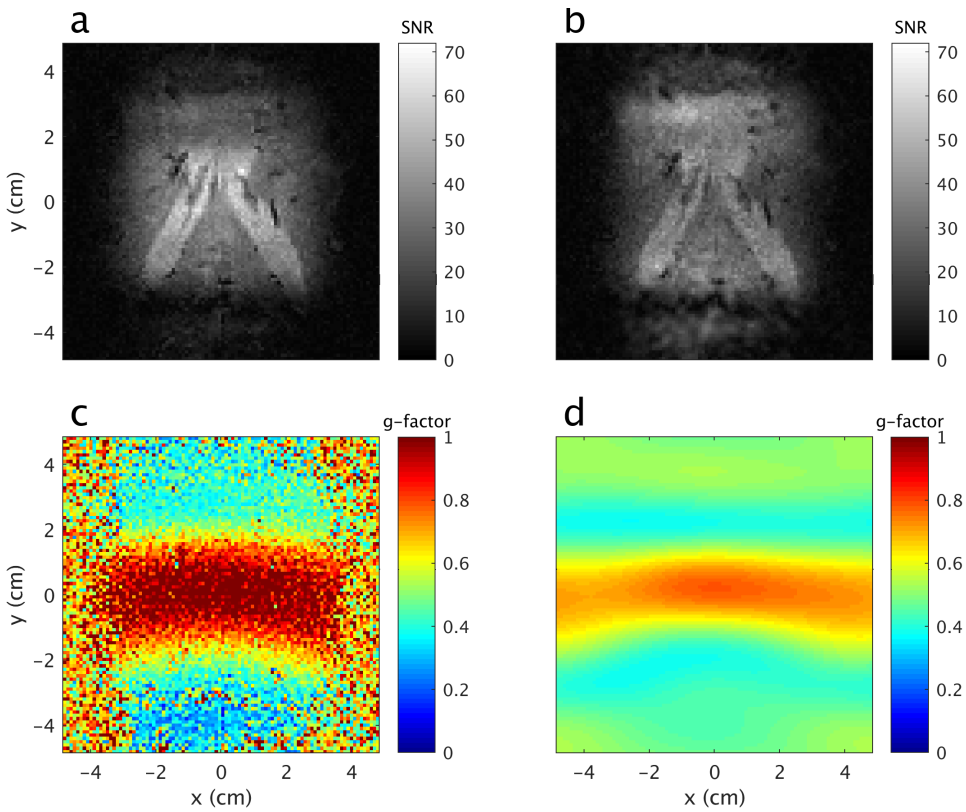

Fig. 4.7. SNR maps and g-factor map for the 4-segment excitation. a) SNR map for the fully sampled readout, excited with the 4-segment 2D HS1 pulse. b) SNR map for the undersampled data. c) The g-factor map calculated by the pseudo-replica method. d) The g-factor map calculated directly from the GRAPPA kernel.

The reconstruction of 3T data using a 32-channel head coil is presented in Fig. 4.8. Again, the direct reconstruction of the undersampled data appears as an aliased, low resolution version of the fully sampled image. Except for some apparent noise amplification, the GRAPPA-reconstructed image recovers the lost resolution and eliminates the aliasing due to data undersampling. SNR and g-factor maps were not calculated for the 3T data.

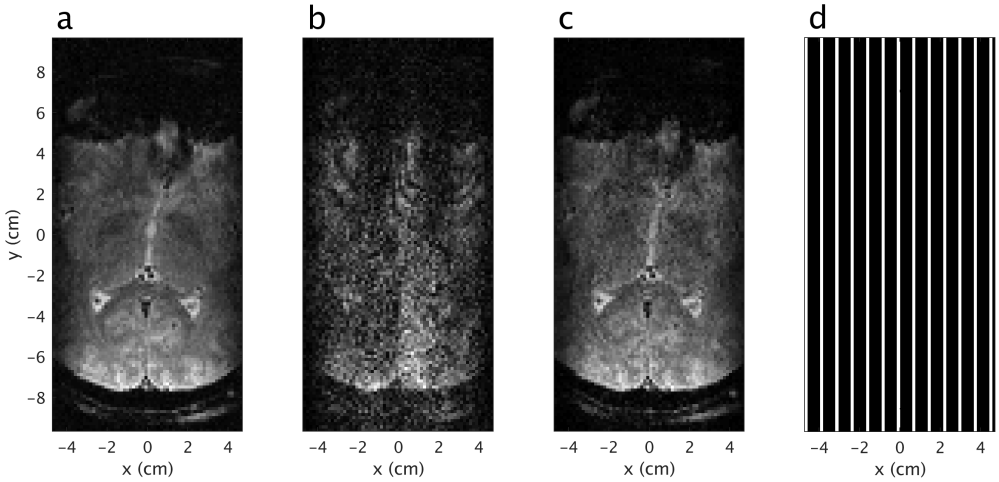

Fig. 4.8. Reconstruction of data from a 4-segment pulse when using a 32-channel receive coil in a 3D GRE EPI sequence. The readout direction is vertical, and the segmented direction of the pulse is horizontal. The horizontal direction was phase encoded during acquisition. a) The fully sampled reconstruction. b) GRAPPA reconstruction using only physical coils for GRAPPA after first summing over pulse segments. c) GRAPPA reconstruction using each pulse segment as a virtual coil d) The undersampling pattern applied to the fully sampled data. White indicates sampled values, whereas black indicates unsampled.

4.6 Discussion

While a segmented multidimensional pulse can provide greater tolerance to off-resonance effects as compared to its single-shot counterpart, the increased imaging time associated with segmentation can be a significant detriment. However, as shown herein, undersampling of acquisition k-space can be performed when using a segmented 2D pulse. Such undersampling can overcome the increased acquisition time associated with segmenting a 2D pulse, without significant detriment to the reconstructed images. As in the case of standard parallel imaging, the acceleration must not exceed the effective number of coils used. Due to limited spatial encoding with a small number of pulse segments, the degree of undersampling must be strictly less

than the number of segments in some cases; otherwise, residual image aliasing persists.

The increased immunity to resonance offset, particularly in the fully-segmented case, is an appealing aspect of segmented multidimensional pulses. Indeed, Weber-Fahr et al. [58] applied a fully segmented pulse defined on a Cartesian trajectory to perform short-TE, single voxel spectroscopy with high resilience to B_0 inhomogeneity. There, the flip angle of the pulse was not increased at the periphery of k-space, followed by data scaling in processing, as was done in the present work. Qin et al. [57] applied a fully-segmented radial trajectory for a similar purpose to [58], which would likely benefit from a similar acceleration technique as presented here. Other applications include reduced FOV imaging with an EPI readout, whereby a 2D pulse permits a reduced FOV so that the EPI echo-train length can be shortened [60]. This lessens image distortions due to B_0 inhomogeneity. Segmenting the pulse in this scenario has the added benefit of reducing distortion of the excitation profile due to resonance offsets and permits a decreased minimum TE. 3D pulses have even longer durations than 2D pulses, further deteriorating pulse performance in the presence of resonance offsets.

As the pulse is segmented, the RF energy deposition increases, although by how much depends on the number of pulse segments. For ease of comparison, an equal TR and flip angle (10°) are used for each segment and compared to the single-shot case with the same parameters. For the 4-segment pulse, with a spatially varying flip angle, the peak flip angle within the magnetization profile for each segment is set to 10°. The first and fourth segments of the 4-segment pulse, which are equal in power by symmetry, deposit approximately 1.61-fold greater RF energy per unit time as the equivalent single-shot pulse. The second and third segments, which are also equal by symmetry, deposit approximately 1.23-fold greater RF energy per unit time as the single-shot pulse. For the fully segmented pulse, all segments are identical, and each segment deposits approximately 3.03-fold greater RF energy as the single-shot pulse per unit time.

Schneider et al. [59] and Jang et al. [67] employed parallel transmission (pTx) when employing 3D pulses for inner volume imaging to increase pulse performance. Applying pTx to shorten pulse duration is intrinsically different than the approach described herein. Excitation k-space is undersampled in pTx and the spatial in-

formation from multiple transmitters is used to compensate for the undersampling [68]. Here, the pulse is fully sampled when considering all segments of excitation k-space, while the acquisition is undersampled. Pulse segmentation and subsequent data undersampling could thus provide an alternative to parallel transmission on systems where such capabilities are not an option. In principle, this method could be extended to work with pTx such that the number of pulse segments is reduced.

Typically, g-factors are greater than unity, representing an amplification of noise due to the undersampling. Here, the fully segmented and 4-segment pulses used resulted in g-factors less than unity in many voxels. Such a result in the past has been argued to originate in the least-squares solution of the GRAPPA kernel weights, which conditions the noise in the reconstruction [63], [69]. The g-factors in this work are significantly less than those found in previous studies, particularly for the fully segmented pulse, yet the underlying reason for this remains unknown. The g-factor maps were calculated by two different methods, pseudo-replica and directly from the GRAPPA kernel, in order to validate the numerical accuracy of this finding. Future efforts will investigate the origin(s) of the small g-factors found herein. However, the virtual coil sensitivities used in this work clearly differ in nature from the sensitivities of physical coils, which are typically greatest in magnitude near the coil and diminish quickly with distance. In light of these differences, future work will investigate the influence of the size of the ACS region on the g-factor map, or on how the choice of GRAPPA kernel affects the g-factor map.

Returning to a comparison with TIAMO [62], the transmitter in the present application is operated in a fixed mode, so there is no index over the transmit field map. In TIAMO, the transmitter is not operated in a fixed mode, so the transmit field map varies between acquisitions. The role of the varying transmit field map in TIAMO is replaced by the pulse segments in this work to achieve spatial encoding. Additionally, the different excitation modes used in TIAMO yield a varying flip angle between each excitation at a fixed spatial location. This non-ideality results in varying T_1-weighting and SNR at the same spatial location for each transmit mode. The present approach maintains consistent T_1 contrast and SNR with each excitation by using the same flip angle with every excitation segment. Finally, the present approach requires a complex summation over the excitation segments before combination of

data from physical coils. This phase sensitive summation is not necessary in TIAMO.

In the spirit of reproducible research, all scripts to generate the in-vivo results in this paper can be found in the database [70].

4.7 Conclusions

We have presented a method for accelerating data acquisition when using segmented 2D RF pulses, which can likely be generalized to multidimensional pulses. We demonstrated the effects of noise amplification and have shown such amplification is approximately spatially uniform. We have also demonstrated the compatibility of the technique with conventional GRAPPA by treating all virtual and physical coil data as individual coils in the GRAPPA algorithm.

Chapter 5

Fast T_2 Mapping at Ultra-high Field using Adiabatic Pulses

5.1 Introduction

Quantitative T_2 magnetic resonance measurements have a wide range of applications, from identifying disease or tissue change [71], [72], to measuring iron concentrations in vivo [73], [74], as well as in ex vivo tissues preserved with iron-oxide nanoparticles (IONPs) [29], [75]. However, using conventional multiple echo spin-echo for quantitative T_2 mapping is strongly limited by transmit field, or B_1^+, inhomogeneity, which increases with field strength. The spatially varying B_1^+ yields flip angle errors, which with multiple refocusing pulses cause the signal to attenuate more rapidly than with full refocusing. These effects can be mitigated by applying a single refocusing pulse per excitation, which only permits the collection of data corresponding to one echo time per excitation. Collecting a single echo with each excitation yields an unrealistically long acquisition which is clinically unfeasible, and the likelihood of subject motion is increased.

Adiabatic pulses overcome the issue of B_1^+ inhomogeneity, although two identical refocusing pulses must be applied to eliminate spatially varying phase induced by each pulse, as first shown by Kunz [76], [77]. The need to apply two refocusing pulses following excitation increases the minimum echo time, in turn decreasing the sensitiv-

ity to fast relaxing spins. Park et al. [78] described that with a specific relationship between a spatially-selective frequency-swept excitation and an adiabatic refocusing pulse, only one refocusing pulse is necessary to eliminate the spatially varying phase induced by the frequency sweep. Using a selective excitation with phase-matched frequency-swept pulses permits a multi-slice acquisition, at the expense of the excitation being non-adiabatic. In contrast, the sequence used by Mitsumori et al. [73] is fully adiabatic to minimize the effects of B_1^+ inhomogeneity. A non-selective adiabatic half-passage (AHP) is used for excitation, followed by adiabatic refocusing. Despite the benefits associated with adiabatic excitation, the sequence with AHP excitation can only acquire data from a single-slice, since spatial selectivity originates from the refocusing pulses.

Herein, we have extended the pulse sequence of Park et al. [78], which allows us to quickly acquire multiple echoes from many slices within a decreased timeframe. The sequence employs adiabatic refocusing to limit signal attenuation resulting from B_1^+ field inhomogeneity. Hereafter, the sequence is referred to as Multi-Slice, Multi-Adiabatic Spin Echo MSMASE. A sequence diagram is presented in Fig. 7.2.

5.2 Materials and Methods

All experiments were performed with a Varian DirectDrive console (Agilent Technologies, Santa Clara, CA) interfaced with a 4T, 90-cm magnet (Oxford Magnet Technology, Oxfordshire, UK) and a clinical gradient system (model SC72, Siemens, Erlangen, Germany). The maximum slew rate available on this gradient system is 100 mT/m/ms. A protocol approved by our institutions IRB was followed for human brain imaging of healthy volunteers after written, informed consent was obtained.

While Park et al. [78] demonstrated three distinct conditions between excitation and refocusing to eliminate the spatial phase resulting from frequency-swept HS1 pulses, Condition I of that work was chosen here. Therein, the time-bandwidth product (R) and duration ($\mathrm{T_p}$) of the HS1 excitation pulse are twice that of the HS1 refocusing pulse such that the bandwidth is the same for both pulses. Here, the parameters for excitation were $R_{exc} = 20$, $\mathrm{T_{p,exc}} = 14$ms, while for refocusing, $R_{\mathrm{exc}} = 10$, $\mathrm{T_{p,exc}} = 7$ms. Condition II of [78] has poor off-resonance performance, while

Condition III requires a higher peak power for the refocusing pulse and has poorer slice definition compared to Conditions I and II. Further specifics of Conditions II and III are well explained elsewhere [78]. Since two refocusing pulses must be applied following the first echo, only the odd echoes are collected, e.g. echoes 1, 3, 5, and on. The peak amplitude for the refocusing pulses was set sufficiently high so that the pulse operated in the adiabatic regime for all spins within the defined slices.

The data were collected with 1mm in-plane resolution, 2.5mm slice thickness, and three slices to stay within FDA recommended SAR limits. The FOV = 256 x 256 mm^2, TR = 4 s, TE = 29.7, 66.1, 102.4, 138.7, and 175.0 ms, with four slices. The phases of the transmitter and receiver were 0° on the first, third, etc. phase encodes, while the phases were 180° on the second, fourth, etc. to push DC signal to the edge of the FOV. The acquisition bandwidth was $sw = 50kHz$.

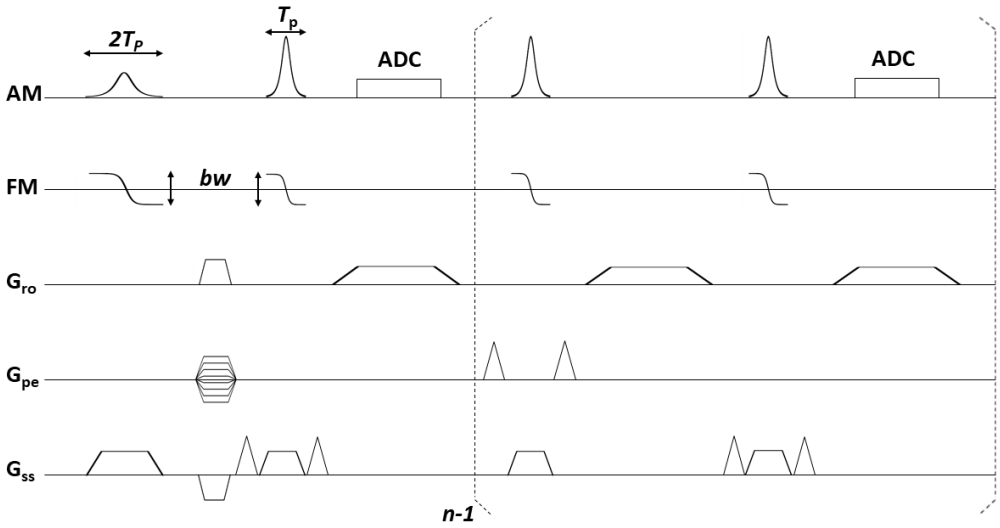

Fig. 5.1. Sequence diagram of MSMASE.

To further reduce the first echo time, the slice refocusing gradient and the first crusher gradient may be combined due to their opposing polarities. While not strictly necessary, combination of slice refocusing and crushing was utilized herein. Additionally, the frequency-encoding gradient may either be refocused with every acquisition, or it can be applied during the even echoes to eliminate the need to adjust the dephasing gradient along the frequency encoding axis. The latter approach was

applied in this work for simplicity. When refocused with each acquisition, the dephasing/rephasing lobes of the frequency encoding gradient must be well-tuned so that imperfections do not propagate to subsequent echoes. Imperfect adjustment manifests as a a shift of the acquisition window relative to $\vec{k} = 0$ for later echoes.

Employing sufficient crushing gradients surrounding the 180° pulses is vital in suppressing stimulated echo from seeping into the acquisition. Stimulated echoes manifested here as a zipper-like artifact in the readout direction of the image(s). While the crushing scheme shown in Fig. 1 worked to visually suppress the zipper artifact in the images corresponding to separate echo times, it was readily visible in the calculated T_2 maps. Since the stimulated echo signal only contaminated the leading points in the frequency-encoding direction, the first 25 points - 9.77% - of each readout were removed. The reconstruction was then treated as a partial Fourier acquisition, using a projection onto convex sets (POCS) algorithm [79], [80],[81] to iteratively determine the removed data. To avoid filtering and data recovery using POCS, alternative crusher placement and/or amplitudes may be used.

MSMASE acquisitions were reconstructed using vnmrJ 4.2, and relaxation maps were calculated using MATLAB 2012b. For each voxel, the time points were fit along the T_2 recovery curve using a three-variable exponential fit [29]. The robustness of the exponential fit was tested for each voxel by adjusting the boundary values [75]. The relaxivity measurements were determined with least-squares fitting.

For gray matter, white matter, and cerebrospinal fluid (CSF), four regions-of-interest (ROIs) were selected manually from a single slice, with each ROI containing 16 - 54 pixels. For both the caudate and putamen, two ROIs were selected, each containing 11 - 30 pixels. With all brain regions, the corresponding ROIs were merged, followed by calculating the mean and standard deviation for each region. This is a similar procedure to that of Jezzard et al. [82].

5.3 Results

The calculated T_2 maps are shown in Fig. 5.2 alongside the anatomical scans corresponding to the second echo, with TE = 66.1 ms. The contrast of the T_2 map images has been enhanced to display structures with low T_2 relative to CSF.

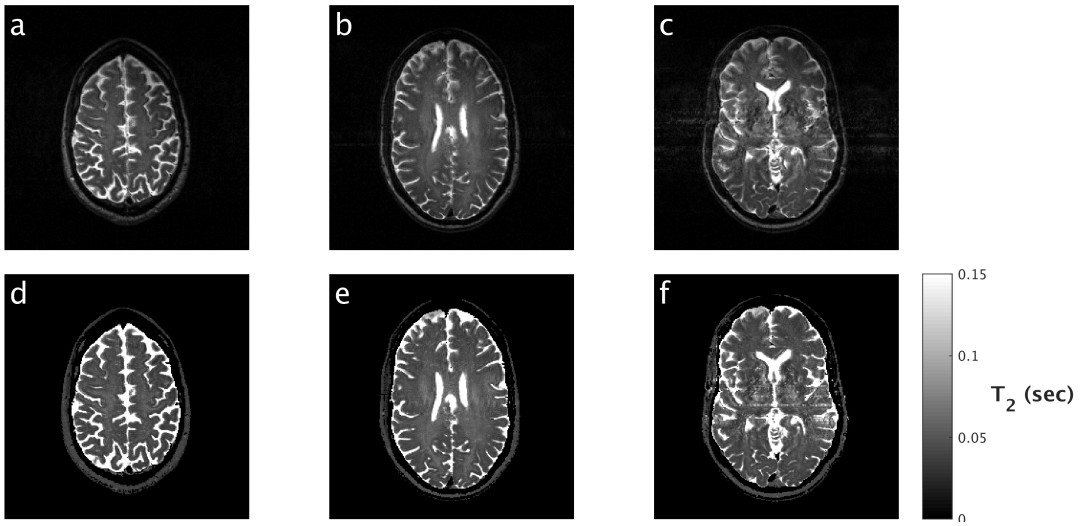

Fig. 5.2. a - c) Anatomical T_2-weighted images collected with TE = 66.1 ms. d - f) The calculated T_2 maps from the corresponding multi-echo acquisition.

A comparison of the results found here at 4T compared to the results found by Jezzard et al. [82], are shown in Table 5.1. The results found here are in good agreement with previously measured values at 4T [82].

Table 5.1: Comparison of apparent T_2 values in multiple brain regions using MSMASE to T_2 values measured in the literature.

$T_2^\dagger$ (ms)					
	Cortical Gray Matter	White Matter	Caudate	Putamen	CSF
MSMASE	61.7 ± 11.4	44.9 ± 4.3	37.5 ± 6.5	39.1 ± 6.4	761 ± 391
Jezzard et al. [82]	63.4 ± 6.2	49.8 ± 2.2	45.7 ± 10.8	47.3 ± 12.0	704 ± 245

CSF - cerebrospinal fluid

5.4 Discussion

Adiabatic pulses far exceed the abilities of amplitude modulated pulses at high-field, where transmit fields are particularly inhomogeneous. The ability to effectively

refocus echoes despite a large spatial variation in peak transmit field permits the ability to rapidly collect quantitative information in a multi-slice fashion. For IONPs, and other short decaying signals, the large intrinsic linewidths demand high-bandwidth excitation and refocusing pulses. In this regime, amplitude modulated pulses require a shorter duration and higher amplitude to maintain a 180° pulse. The resulting short, high amplitude pulses yield excessive heating and potentially untenable peak pulse amplitudes. By distributing energy in time, adiabatic frequency-swept pulses are able to refocus all off-resonances within the bandwidth of the pulse with a significantly lower peak transmit amplitude [18].

By replacing the AHP excitation used by [73], a minor decrease in resilience to B_1^+ inhomogeneity is sacrificed in return for the ability to obtain data from multiple slices. In both sequences, all refocusing is fully adiabatic and the minimum echo time and echo spacing are comparable. In principle, any amplitude modulated pulse could be used for slice-selective excitation, followed by adiabatic refocusing. Using an amplitude modulated excitation requires two adiabatic refocusing pulses before the first collected echo, in addition to the necessary crushing gradients and time delays for proper refocusing. Combined, these effects yield a longer minimum echo time than using a pair of matched frequency-swept pulses as performed herein. By increasing the number of slices, the number of refocusing pulses is increased multiplicatively, while the SAR increases commensurately. Hence, high field strengths demand limiting the number of slices or the number of echos acquired per slice. More slices may be used at lower field strengths due to the correspondingly lower SAR.

Using a train of high-amplitude, large bandwidth pulses results in high SAR. With the parameters described in this work, the 10-minute averaged SAR was 97.6% of the FDA limit. In principle, 20 slices could have been achieved on samples if SAR was not a limiting issue. By increasing TR, energy deposition is more distributed in time, while the increased acquisition time can be compensated for by employing parallel imaging [25], [26]. In the absence of multiple coils, previous studies have leveraged sparsity along the echo time dimension to accelerate acquisition [83], [84]. More recently, Zhang et al. [85] utilized a locally low rank approach to achieve more accurate results at high acceleration factors, even with a single receiver. Future work will explore the use of accelerated imaging techniques with MSMASE at high fields

strengths to limit SAR.

Chapter 6

Alternative Methods for Imaging with Inhomogeneous B_0

6.1 Slant-Slice Method

6.1.1 Introduction

With asymmetric magnet designs, the inhomogeneity of the polarizing field B_0 is often predominantly along one axis and can be made approximately linear. Hence, it is equivalent to imaging with a static, linear field gradient on at all times. Employing spin-echos and selecting rotated slices, Epstein & Magland [86] demonstrated the ability to perform a fast spin-echo sequence for T_2-weighted anatomical imaging in this scenario. Denoting the permanent gradient as G_p, an additional gradient G_x orthogonal to G_p was used during slice selection, and frequency-encoding was achieved by reversing the polarity of G_x. Defining the a quantity $\mu = \frac{G_x}{G_p}$, the angle between the normal vector of the slice and G_p is given by $\theta = \arctan(\mu)$, as shown in Fig. 6.1. Since the readout gradient is obtained by reversing the polarity of G_x, the angle α between the readout gradient and the selected slice is $\alpha = 90^\circ - 2\theta$.

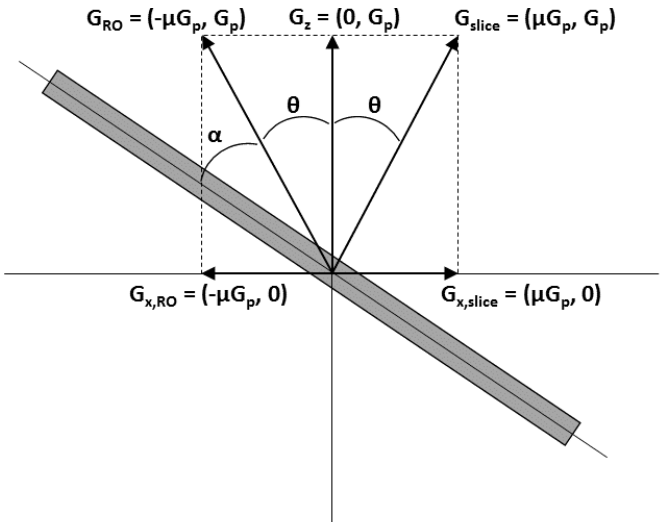

Fig. 6.1. Demonstration of using the static field gradient for both slice selection and readout. Adapted from [86].

In the case that $\alpha \neq 0°$, the readout gradient does not lie in the plane of the slice, which results in blurring. Epstein & Magland [86] showed that a given sample in k-space, at $k(t)$, the signal is attenuated by the factor

$$\mathrm{A}(\mu, t) = \mathrm{sinc}\big(k(t)d\frac{1-\mu^2}{2\mu}\big), \tag{6.1}$$

where d is the slice thickness. Such signal attenuation results in blurring, as it amounts to filtering k-space and more severely attenuates larger spatial frequencies. For μ near unity, the attenuation factor A is approximately 1, and the blurring is negligible.

The work described by Epstein & Magland [86] was limited to T2-weighted fast spin-echo sequences. Particularly at high-field, such as 4T and above, fast spin-echo is limited by the high SAR necessary for a long train of echos. Here, the slant-slice method is adapted to generate T_1 weighted images using a modified MDEFT [87] sequence.

6.1.2 Materials and Methods

Experiments were performed with a Varian DirectDrive console (Agilent Technologies, Santa Clara, CA) interfaced with a 4T, 90-cm magnet (Oxford Magnet

Technology, Oxfordshire, UK) and a clinical gradient system (model SC72, Siemens, Erlangen, Germany). The maximum slew rate available on this gradient system is 100 mT/m/ms. A protocol approved by our institutions IRB was followed for human brain imaging of healthy volunteers after written, informed consent was obtained.

To generate a static linear field, the z-gradient was turned on at the beginning the sequence and not modified until the entire imaging sequence was complete. As a result, the magnetic field variation was approximately 80 kHz over a 25 cm length along the z-direction. Imaging was performed using the modified MDEFT [87] sequence shown in Fig. 6.2.

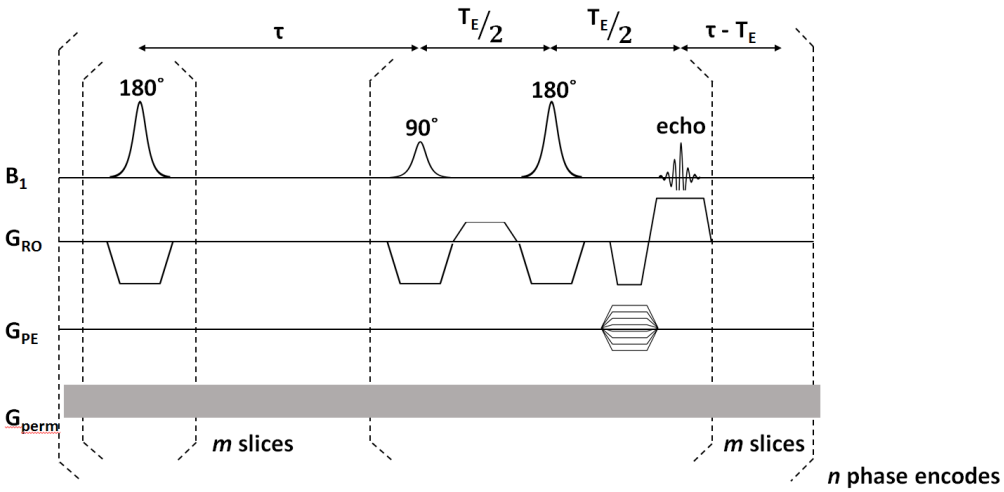

Fig. 6.2. Pulse sequence demonstrating the combination of the slant-slice method and MDEFT.

The sequence parameters were: 1 average, TR = 1500 ms, TE = 9.11 ms, acquisition bandwidth = 119047 Hz, slice thickness = 2.5 mm, and 1 x 1 mm^2 in-plane resolution. The pulse widths were 2.06 ms, while the time-bandwidth products of the excitation and refocusing/inversion pulses were 3.6 and 2.375, respectively. Spin inversion, excitation, and refocusing were performed with identical sinc pulses weighted by a Gaussian. Due to the inability to change G_p, the π pulse slice thickness is slightly thinner than that of the $\frac{\pi}{2}$ pulse. The inversion and refocusing pulse durations were not shortened to compensate the slice narrowing due to peak B_1 power limitations.

6.1.3 Results

Six selected slices of a 16-slice set are shown in Fig. 6.3. The slices were imaged at an oblique angle, specifically with $\alpha = 45°$, and as such are not displayed in standard anatomical orientation.

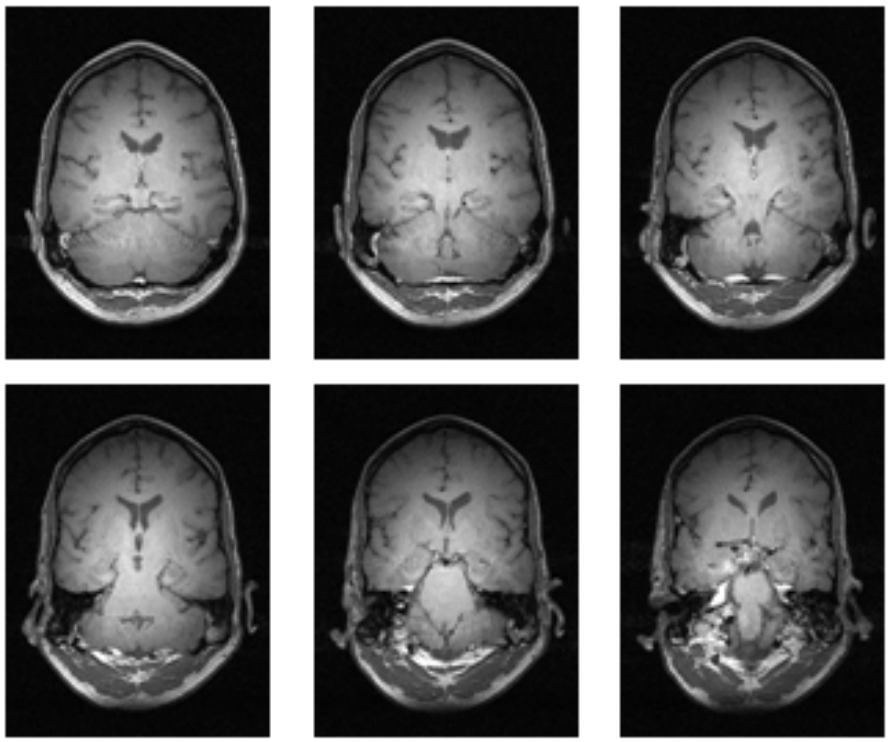

Fig. 6.3. Six of the slices acquired using slant-slice MDEFT, from a 16 slice set.

6.1.4 Discussion

An additional constraint in the slant-slice method is imposed on the FOV, since the FOV in the frequency-encoded direction is given by $FOV = \frac{sw}{\gamma G_{RO}}$, where sw is the acquisition spectral width and $G_{RO} = \sqrt{G_x^2 + G_p^2}$. Since G_p is fixed and the sw is limited to a discrete set by hardware constraints, the FOV cannot be set arbitrarily. Further, the composite frequency-encoding gradient is typically larger than in conventional MRI for a FOV typical for neuroimaging. Thus, the sw must

be relatively large, leading to a commensurate decrease in SNR.

The slant-slice method requires relatively homogeneous magnetic fields with the exception of the constant linear term. Hence, while well-adapted to situations where a permanent, linear gradient is imposed, the slant-slice method is sensitive to nonlinearities in the permanent field. Finally, the permanent gradient induces irreversible diffusion losses; however, in T_1-weighted images, these losses are not significantly noticeable.

6.2 Non-Fourier Image Encoding: Spatiotemporal Methods

6.2.1 Theory of Spatiotemporal Encoding

While the slant-slice method employs conventional Fourier encoding, a less conventional approach to imaging with inhomogeneous B_0 is to employ *spatiotemporal* encoding methods [88], [89], [90], [91]. In these methods, a swept radiofrequency pulse [18] is applied in the presence of a linear field gradient and B_0 inhomogeneities, which produces a quadratic phase in space along the direction of the field gradient [92]. For spins far from the vertex of this quadratic phase, integration across a voxel leads to destructive interference. Thus, the spins near the vertex are the dominant contributors to detected signal at any given time. In a spin-echo sequence utilizing spatiotemporal encoding, the field inhomogeneities at a fixed spatial location x are refocused as the vertex of the quadratic phase profile sweeps through x. Since the signal magnitude is then independent of the value of B_0 at x, assigning the magnitude of the signal at time t to the image magnitude at the vertex position $x(t)$ results in a distortion-free, low-resolution image of the object.

Direct assignment of the signal magnitude at time t to spin density ρ (the image) as described above yields a low-resolution image, as it assigns all signal collected at time t to a single spatial position. A more SNR efficient approach is described in [88], where an inverse problem approach is taken, leveraging knowledge of how the signal energy is distributed in space and time to correctly assign signal to all voxels at a given time, as is done with conventional Fourier encoding. To see how this is done,

first consider the discrete-space, discrete-time signal equation:

$$s(t_j) = \sum_m \exp(ik_j \cdot x_m)\rho(x_m, t_j), \tag{6.2}$$

where system-dependent factors such as gain have been absorbed into the definition of the spin density ρ. It has been assumed that the signal and spin density have both been vectorized. In Eq. 6.2, the quadratically varying phase is generally not solvable analytically, but is included in the definition of ρ.

Note the spin density is a function of both space and time in Eq. 6.2 - the vertex of the quadratic phase moving in space makes the spin density appear to change in time. Fortunately, as only the spatially dependent term is of clinical interest, the image is separable from the time-dependent term. That is,

$$\rho(x_m, t_j) = Q(t_j, x_m)\rho(x_m), \tag{6.3}$$

where the spatially- and time-dependent term has been denoted by Q. Hence, Eq. 6.2 can be rewritten as

$$s(t_j) = \sum_m \exp(ik_j \cdot x_m)Q(t_j, x_m)\rho(x_m). \tag{6.4}$$

In matrix form, this becomes

$$\vec{s} = \boldsymbol{A}\vec{\rho}, \tag{6.5}$$

where the j, m^{th} entry of $\boldsymbol{A}$ is given by

$$\boldsymbol{A}_{j,m} = \exp(ik_j \cdot x_m)Q(t_j, x_m). \tag{6.6}$$

As $\boldsymbol{A}$ generally consumes several GB of computer memory for an imaging sequence with spatiotemporal encoding in multiple dimensions [88], efficient methods for obtaining an optimal solution for ρ from Eq. 6.5 are discussed later in this chapter. The exact form of $\boldsymbol{A}$ is calculated numerically by Bloch simulation of the entire sequence, storing in memory only those time points corresponding to acquisition in the sequence. Intra-voxel averaging of spins [93] is necessary to correctly predict the

coherence effects produced by a frequency-swept RF pulse. Averaging amounts to simulating the sequence for a large grid of spins followed by binning to the desired image resolution. In practice, between 5-10 spins per voxel per encoded dimension is typically sufficient to accurately simulate the effects of intra-voxel dephasing.

In principle, $\boldsymbol{A}$ exactly describes the experiment performed, predicting a signal $s(t)$ from an accurate image estimate ρ. Realistically, exact knowledge of $\boldsymbol{A}$ is impractical, as it requires knowledge of the transmit and receive fields, timing errors, gradient waveform errors, B_0 inhomogeneities, patient motion, etc. While many of these parameters can be measured or tracked during an experiment and incorporated into $\boldsymbol{A}$, any mismatch between the model $\boldsymbol{A}$ and the experiment results in image artifacts. From experience, gradient waveform and timing errors are the dominant source of image artifacts in spatiotemporal image encoding. Hence, simulations only produce an estimate of $\boldsymbol{A}$. A method to experimentally measure the encoding matrix is presented in the Sequence Design section.

6.2.2 Reconstruction Methods

A least-squares inverse solution to Eq. 6.5 can be found by using the Moore-Penrose psuedoinverse. However, the pseudoinverse requires the inversion of $\boldsymbol{A}$, which is computationally intractable. A better approach is to begin with a more general form of Eq. 6.5 which can be solved iteratively using first-order methods:

$$\hat{\rho} = \arg\min_{\rho} ||\mathbf{A}\rho - s||_2^2 + \lambda R(\rho), \tag{6.7}$$

Here, $R(\rho)$ is a *regularizer* which permits the incorporation of *a priori* constraints on the image and λ controls the strength of the regularizer relative to the data fidelity term $||\mathbf{A}\rho - s||_2^2$. Lower values of λ reduce the effects of regularization, more strongly enforcing the predictions of $\boldsymbol{A}$, while higher values of λ permit a larger discrepancy between the measured signal and the predicted signal for an estimate of the image ρ. Setting $\lambda = 0$ would reduce the result to that of the pseudo-inverse. One of two common regularization methods is Tikhonov, with $R = |\rho|^2$, which limits the maximum voxel intensity. The other is Total-Variation (TV) [94], which reduces noise

while preserving edge definition. The effects of regularization on image resolution are described in [95]. Fast algorithms to obtain optimal solutions for these regularizers are found in [96],[97].

Although the inverse of $\boldsymbol{A}$ need not be known for first-order iterative methods, storing such a large matrix potentially renders even this method prohibitively memory intensive. Gutierrez et al. [98] proposed to estimate the forward operator $\boldsymbol{A}$ as the composition of a set of "fast" transforms with sparse matrices, which can then be applied efficiently and which requires little memory. To see this, consider a collection of k fast transforms, denoted by $F_1, F_2, ..., F_k$, and a collection of sparse matrices, $S_1, S_2, ..., S_k$. Here, the transforms F_j are predetermined, and the sparse matrices S_j are found by specifying a desired approximation accuracy. Hence, the S_j are determined by approximating the forward operator as

$$A \approx \sum_{l=1}^{k} S_l F_l \equiv \hat{A}. \tag{6.8}$$

Two example fast transforms which could be used in Eq. 6.8 are the FFT and the identity transform. Once the matrices S_k have been determined for a given forward operator $\boldsymbol{A}$, they can be stored and do not need to be recalculated.

6.2.3 Sequence Design

STEREO

The first spatiotemporal encoding pulse sequence used in this work was STEREO (STEering REsonance over the Object) [88]. A brief overview of the method is presented here. The principle underlying STEREO is to excite spins along a 2D spiral trajectory using sin/cos modulated gradient waveforms in two dimension during a frequency-swept RF pulse of duration T_P. The simultaneous application of the FM pulse and the oscillating gradients yields maximum energy deposition along a vertex traversing the spiral - for an excellent graphical description, see Fig. 2 of [88]. The resonance condition (see Ch. 2) is satisfied when

$$\Delta\omega(t) - \gamma\vec{G}(t) \cdot \vec{r} = 0, \tag{6.9}$$

where $\Delta\omega(t)$ is the RF offset as a function of time, $\vec{G}(t)$ are the time-dependent linear field gradients, and $\vec{r}$ is the spatial position of a spin. For an Archimedean spiral, the gradients are sinusoidal, and given by

$$G_x(t) = G\sin(\theta(t)) \tag{6.10}$$

$$G_y(t) = G\cos(\theta(t)), \tag{6.11}$$

where G is the gradient magnitude. For a set of N interleaved spirals, the angle $\theta(t)$ for the i^{th} spiral is

$$\theta_i(t) = \frac{2\pi t}{T_P} + \frac{2\pi i}{N}. \tag{6.12}$$

The position of the vertex at time t is

$$\vec{r}(t) = \hat{G}(t)\frac{\Delta\omega(t)}{\gamma G}, \tag{6.13}$$

where $\hat{G}$ is a unit vector in the instantaneous direction of the gradients. The pulse sequence is shown in Fig. 6.4.

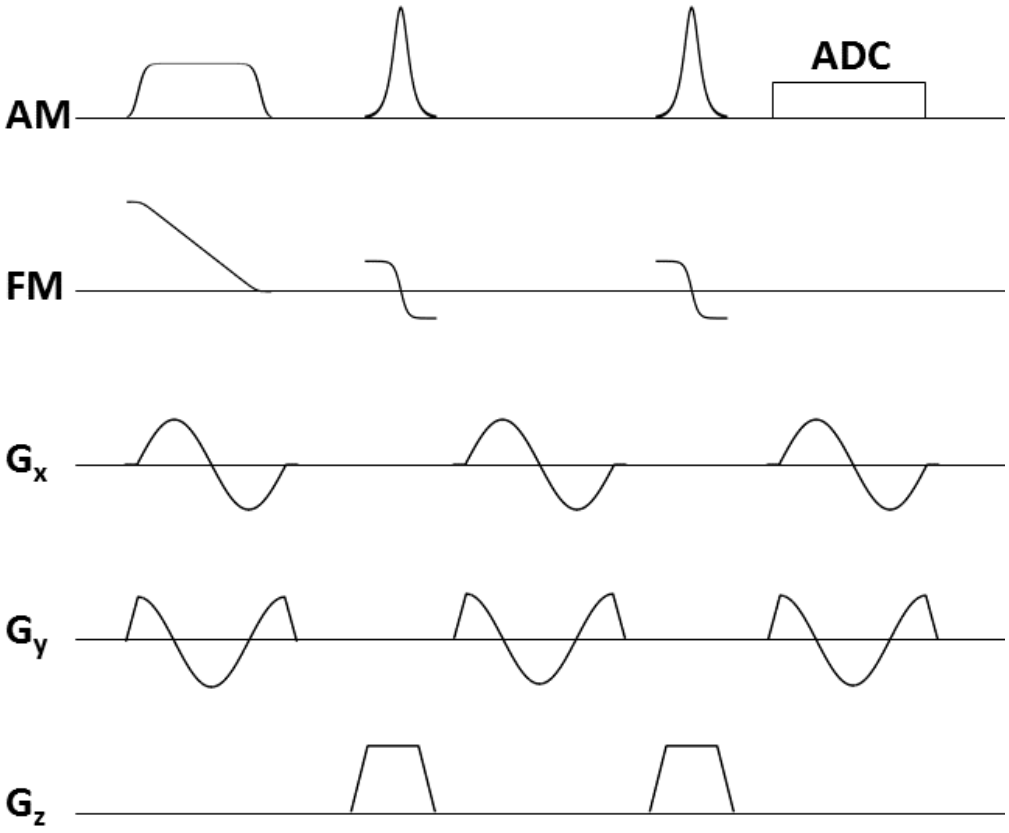

Fig. 6.4. Diagram of the STEREO pulse sequence.

In order to directly measure the encoding matrix, phase encoding gradients are added to the sequence in the spatiotemporally encoded dimensions, as presented in Fig. 6.5. For a sequence such as STEREO with many different excitations, each excitation would need to be measured, making such a method impractical. However, for sequences with few different excitations, this method can be performed more quickly. Measurement of the encoding matrix should be performed on a large, uniform phantom, as the encoding matrix is generated numerically using a completely uniform phantom within the FOV.

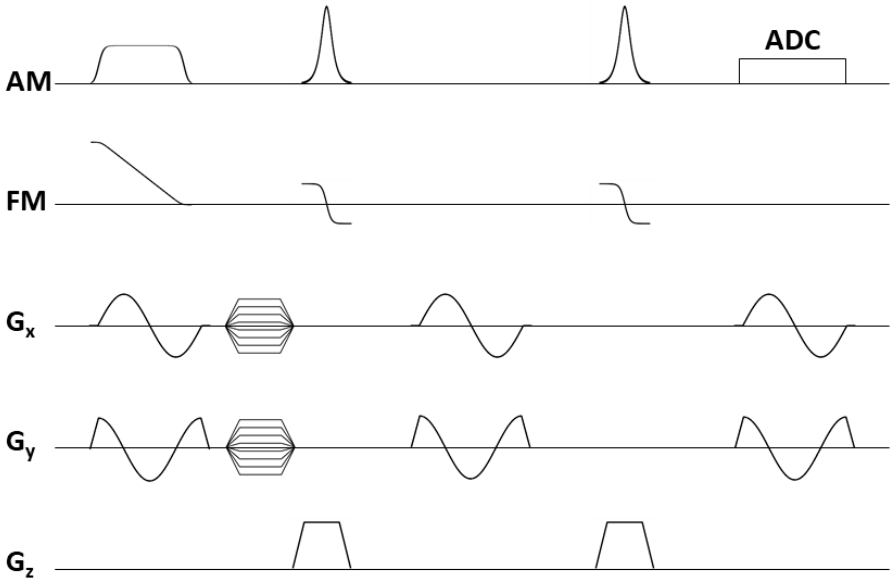

Fig. 6.5. Diagram of the STEREO pulse sequence with phase encoding to measure the encoding matrix.

2D HS1

The spiral 2D HS1 pulse is generated similarly to the 2D pulse described in Chapter 3, except on a spiral trajectory. The spiral k-space trajectory is given by

$$\vec{k}(t) = k_{\max}\tau^{\alpha}\exp(i\theta(t)) \tag{6.14}$$

$$\theta = 2\pi N\tau^{\alpha}. \tag{6.15}$$

The gradient waveforms are generated by taking the derivative of this expression, and then generated numerically. If the gradients are generated by taking the numerical derivative of the k-space trajectory, errors may occur near $\vec{k} = 0$. The RF pulse amplitude and phase are given by

$$\omega_1(t) = \omega_1^{\max}\mathrm{sech}(\beta\frac{|\vec{k}|}{k_{\max}}) \tag{6.16}$$

$$\phi_{RF}(t) = \frac{\pi R}{2\beta}\log\Big(\cosh(\beta\frac{|\vec{k}|}{k_{\max}})\Big). \tag{6.17}$$

Above, $\omega_1^{\max}$ denotes the peak RF amplitude, R is the time-bandwidth product of the pulse, and β is the cutoff value of the pulse. Conventionally, $\text{sech}(\beta) = .01$, truncating the pulse at 1% peak value. The spatiotemporally encoded sequence using this pulse on excitation traverses the same k-space trajectory on readout as was used for excitation, as shown in Fig. 6.6.

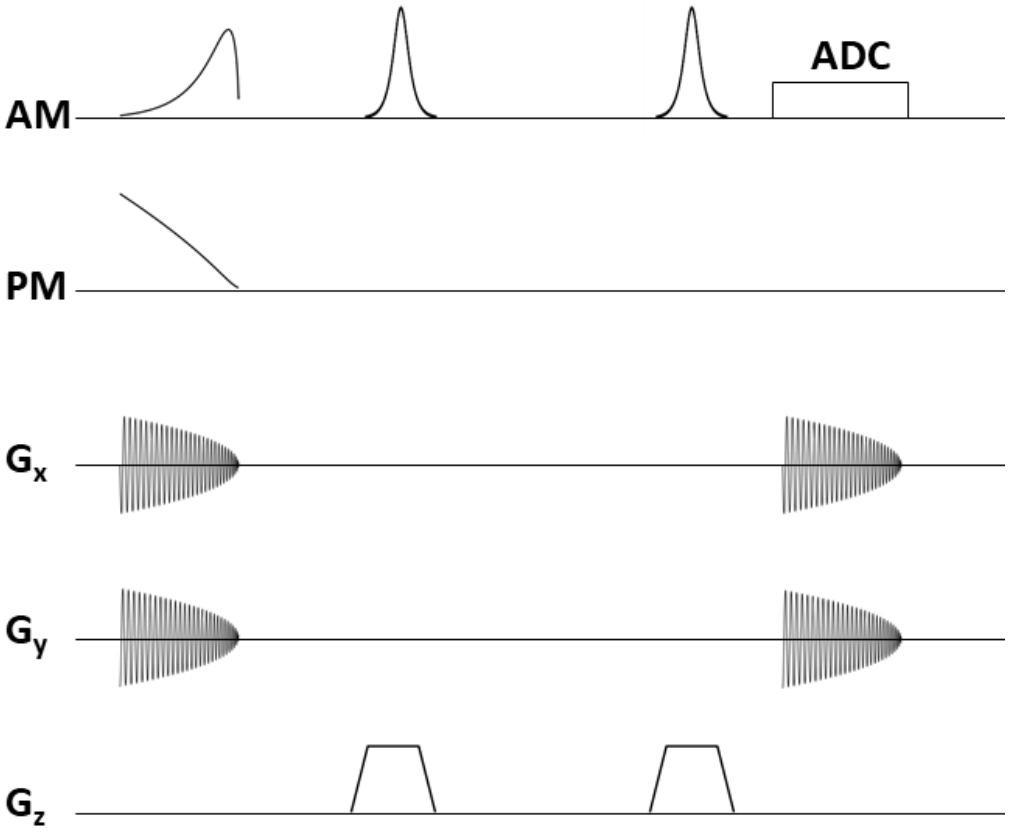

Fig. 6.6. Diagram of the spiral 2D HS1 pulse sequence. Here, PM denotes phase modulation.

6.2.4 Experiments

Experiments were performed with a Varian DirectDrive console (Agilent Technologies, Santa Clara, CA) interfaced with a 4T, 90-cm magnet (Oxford Magnet

Technology, Oxfordshire, UK) and a clinical gradient system (model SC72, Siemens, Erlangen, Germany). The maximum slew rate available on this gradient system is 100 mT/m/ms. A protocol approved by our institutions IRB was followed for human brain imaging of healthy volunteers after written, informed consent was obtained.

STEREO

A single 2D STEREO experiment was performed using 128 spokes and a maximum excitation radius of 10 cm. The excitation RF pulse was a HS8, time-bandwidth product = 128 [18] with a 6ms duration. The flip angle was 90°. Slice-selective refocusing was performed using two HS1 pulses [19] with sufficient power to be operating in the adiabatic regime. Other sequence parameters were TR = 2 sec, TE = 46 ms, acquisition bandwidth $sw = 89285.7$ Hz, and 1024 complex data points were collected per excitation. Data were collected following the ramp up of the readout gradients. The first spiral was repeated 3 times before data collection to drive the system into a steady state prior to imaging. Without reaching a steady-state, the signal intensity for the first several spirals is abnormally high, resulting in image artifacts. EXORCYCLE [99] was used to suppress unwanted signal originating from the transition regions of the selective refocusing pulses. The total scan time was 17.07 minutes, but if only one average had been used, the total time would have been 4.27 minutes.

To examine the effects of grid size on image quality, the data for this sequence was reconstructed onto three different grid sizes: 64 x 64, 96 x 96, and 128 x 128. In all cases, the simulation FOV was 20cm with 10 x 10 intravoxel averaging. Simulations assumed perfect refocusing pulses. Tikhonov regularization was used to address a hyperintensity artifact in the center of the images. All reconstructions used the same experimentally obtained signal.

2D HS1

The experiment using the 2D HS1 pulse for excitation was performed in two dimensions, with two standard adiabatic 180° HS1 pulses used for slice selection and refocusing. The time-bandwidth product of the 2D pulse was R = 12, while the duration was 26 ms. The k-space trajectory for both excitation and readout was a 28.5 turn spiral, where the readout trajectory was time-reversed compared to excitation. Both sampled their respective k-spaces to 3mm resolution, such that $k_{\max} = \frac{1}{3mm}$, with $\alpha = 0.3$ in Eq. 6.15. Four averages were collected using EXORCYCLE [99]

phase cycling. The repetition time was 2 seconds while the nominal echo time (for the acquisition of k = 0) was 34 ms. The acquisition bandwidth was 250000 Hz and 6500 complex points were collected. The flip angle was 45°, as the pulse performance begins to degrade further from the small-tip angle regime [39]. Additionally, the magnetization profile degrades with excitation k-space trajectory errors. Therefore, the excitation gradients were measured using the offset slice method [46]. In this method, a single 1-mm thick slice was offset 1.5 cm from isocenter for both gradient channels. The measured waveforms were used to generate the 2D pulse corresponding to the experimental trajectory. The same technique was used to measure the readout gradient waveforms so the observed readout trajectory could be used for gridding and to generate the forward model.

By considering the 2D selective pulse as a mask on the object, the mask can be generated via Bloch simulation and pointwise multiplied by the gridded and model-based reconstructions to limit spurious signal from contaminating the image in regions where it is known there should not be signal. As the data consistency term in the model-based reconstruction does not change with arbitrary fluctuations where there is no magnetization, any perturbation in these regions is multiplied by zero, and thus are impacted only by the regularization. Moreover, in the limit of large undersampling, gridding experiences a large amount of artifact outside the excitation region, as well. For these reasons, masking was done in this work as described here on both the gridded and model-based reconstructions.

To further distinguish the performance of the presented technique compared to gridding, a numerical experiment was performed by undersampling, by various amounts, the model, signal, and acquisition k-space trajectory to emulate the effects of undersampling the acquisition. Adjacent time points were averaged, and the resulting model, trajectory, and signal were used for the same reconstructions as the corresponding fully sampled data.

6.2.5 Results

STEREO

Fig. 6.7 shows the reconstruction results at various grid sizes. The spiral artifacts

become more prominent as the grid size is increased. Despite the spiral artifacts, the images have excellent contrast and SNR.

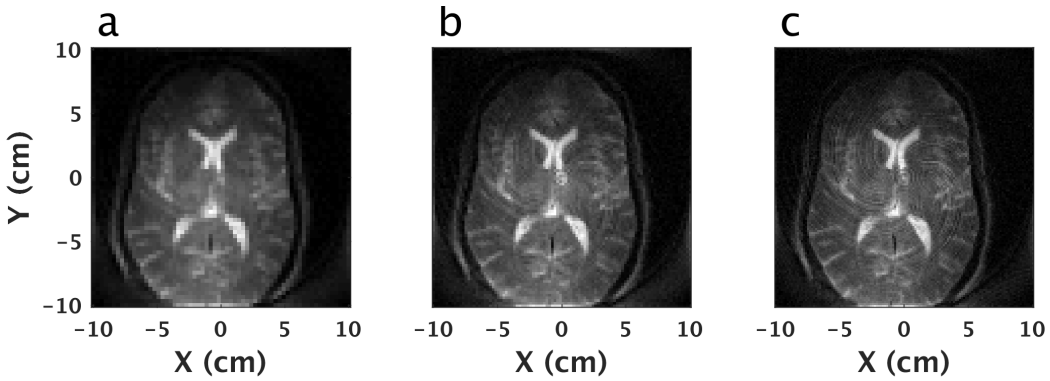

Fig. 6.7. Algebraic reconstructions using the approach described in this section at three different grid sizes. Reconstructions on a a) 64 x 64 grid, b) 96 x 96 grid, c) 128 x 128 grid.

2D HS1

The model-based reconstruction for the 2D pulse demonstrates the superiority of the model-based reconstruction over gridding, especially at high undersampling factors. Comparing the fully sampled data, Figs. 6.8b and 6.8c, there is visibly less blurring and sharper edges in the model-based reconstruction. While the gridded result has clearly degraded at high undersampling factors, particularly in apparent resolution, the undersampled model-based reconstruction is nearly visually identical to Fig. 6.8c, the fully sampled reconstruction.

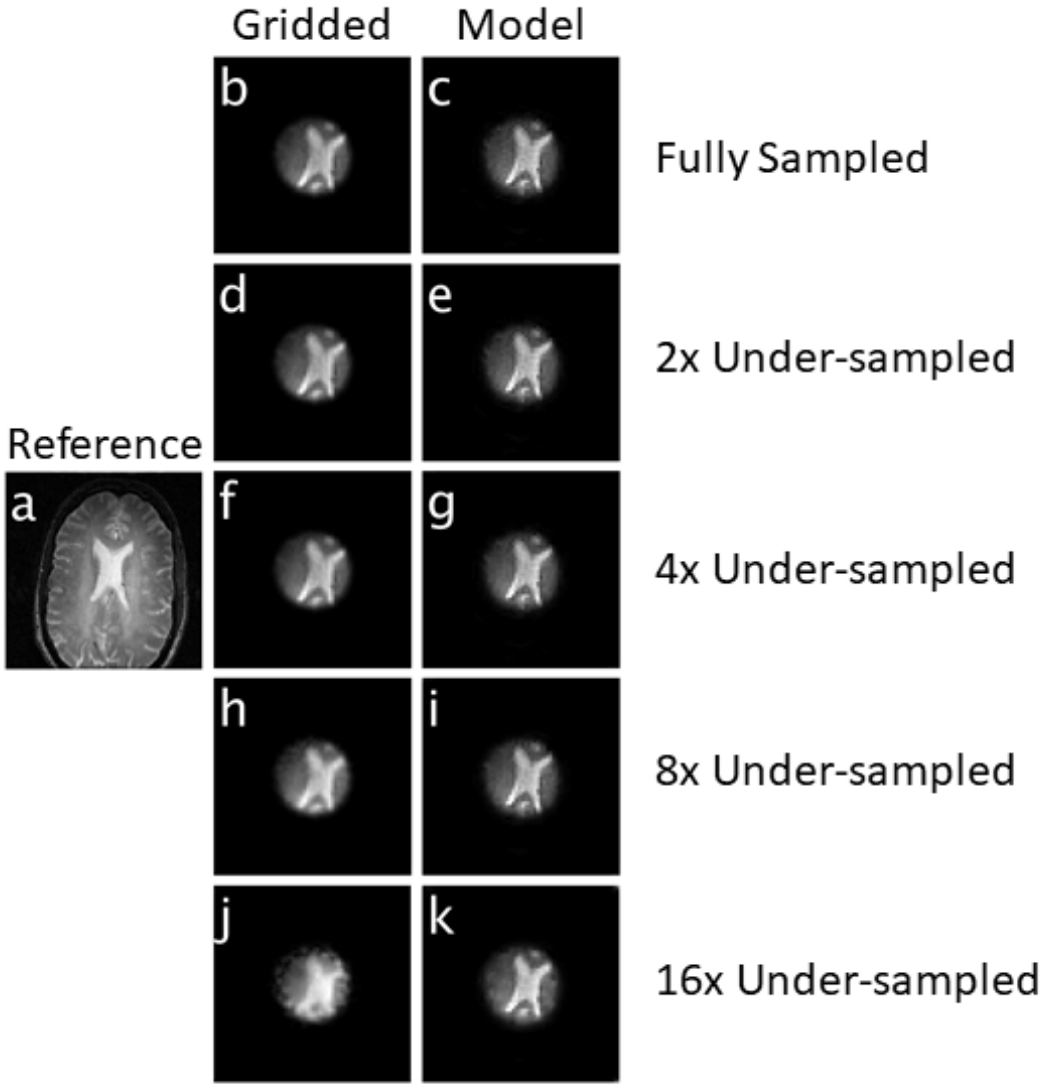

Fig. 6.8. Comparison of reconstructions for single-shot spatiotemporal acquisition. a) Fully sampled reference image. (b, d, f, h, j) Reconstructions using gridding at the indicated undersampling factors. (c, e, g, i, k) Model-based reconstructions at the indicated undersampling factors.

6.2.6 Discussion

Regarding STEREO, the direction pseudo-inverse calculation performed in previous work [88] limited the grid size for the encoding matrix to 51 x 51 for reasonable

reconstruction times, resulting in limited spatial resolution. The iterative reconstruction methods applied herein allowed larger grid sizes, resulting in higher spatial resolution. While images reconstructed onto smaller grid sizes exhibit few artifacts, those reconstructed onto larger grid sizes began to exhibit spiral artifacts. Phantom studies also showed similar spiral artifacts, eliminating motion as a likely cause. Hence, the suspected source of these artifacts is gradient waveform and timing errors, since each spiral is distorted differently by the gradient amplifiers. Static system imperfections, such as transmit and receive field inhomogeneities, are absorbed into the image when solving for ρ. As STEREO is a spin-echo sequence, B_0 inhomogeneity is fully refocused and does not contribute significantly to image artifacts in STEREO. The ability to ignore B_0 inhomogeneity assumes the excitation trajectory defined by the gradients is not substantially altered by the presence of the field inhomogeneities. If necessary, a B_0 map can be incorporated into the model and the RF pulse can be compensated to excite an undistorted trajectory.

Incoherent, noiselike artifacts arise if the simulation FOV is chosen to be smaller than the maximum excitation radius in STEREO. Signals originating from outside the FOV are not encoded in the encoding matrix, and heuristically, appear as noise in the reconstructions. The advances herein demonstrate the ability to image at high resolution using STEREO with reasonable reconstruction times and limited computational requirements. A caveat is the necessity to accurately simulate the forward operator.

Compared to gridding, the model-based reconstruction is able to better utilize available data in the presence of undersampling to maintain a high quality reconstruction. The reconstruction fidelity is maintained by enforcing priors on the image through regularization, such as Tikhonov or Total Variation. With large amounts of undersampling, gridding attempts to interpolate measured data onto neighboring, Cartesian k-space points without having any measured data in the near vicinity of the re-sampled points. The sparse sampling then leads to large errors in the interpolated values, whereas the model-based reconstruction does not explicitly perform interpolation and hence is able to avoid such problems.

Chapter 7

Future Directions

Multiple new approaches to tolerate large field inhomogeneities have been presented. A method to decrease 2D RF pulse duration by segmenting the k-space trajectory was demonstrated, which increases pulse bandwidth at the expense of increased imaging time. A technique to overcome the increased imaging duration by leveraging the unique spatial modulation induced by the pulse segments was subsequently described. Therein, the different pulse segments were treated as virtual coils and used in combination with parallel imaging techniques. In this work specifically, GRAPPA was employed due to its robust performance in the absence of explicit coil maps. Future developments in the area of segmented pulses include discovering the cause of the paradoxically small g-factors found in Chapter 4, as the SNR decreased significantly less than anticipated given the acceleration factors used. Extensions to non-Cartesian excitation trajectories and finding optimal acquisition trajectories for a given segmented pulse are also of interest.

An adiabatically refocused, multi-echo, multi-slice sequence was developed which permits the rapid collection of quantitative T_2 images. Quantitative relaxation maps are useful in a wide range of applications, most interestingly to measure IONP concentrations in ex vivo tissues. The primary benefits of the sequence described herein are the high-bandwidth pulses, yielding the technique robust to polarizing field inhomogeneity, and adiabatic refocusing, rendering the sequence robust to B_1^+ inhomogeneity. The largest hindrance with the method is high SAR, stemming from needing two refocusing pulses per echo. Further developments may explore methods to circumvent the

need for two adiabatic refocusing pulses per echo. Other extensions include increasing the repetition time to lower SAR through the use of locally-low rank methods and/or parallel imaging to overcome the increased repetition time.

Perhaps the most widely applicable technique herein is spatiotemporal encoding with model-based reconstruction. Spatiotemporal encoding is largely immune to off-resonance effects, making it an ideal candidate for imaging with inhomogeneous fields. However, without considering the image reconstruction as an inverse problem, spatiotemporal encoding exhibits large SNR losses. With multidimensional spatiotemporal encoding, or when experimental imperfections need to be included in the forward model, the forward model generally needs to be constructed via Bloch simulation, returning large, dense matrices which realistically cannot be stored in memory or applied efficiently. By representing the dense matrix as a collection of sparse matrices with fast implementations, the image reconstruction problem becomes feasible. Herein, the 2D spatiotemporal information encoded by the STEREO sequence was reconstructed quickly by this method. Moreover, for spiral trajectories with spatiotemporal encoding, the model-based reconstruction greatly outperformed conventional gridding and FFT. By constructing physically accurate models in cases with large polarizing field inhomogeneity, high-quality magnetic resonance imaging should be realizable with clinically relevant reconstruction times in magnets with poor polarizing field inhomogeneity.

References

[1] E. Haacke, R. Brown, M. Thompson, and R. Venkatesan, *Magnetic Resonance Imaging: Physical Principles and Sequence Design*. John Wiley & Sons, Inc., 1999, ISBN: 9780471351283.

[2] A. Abragam, *Principles of Nuclear Magnetism*. Oxford University Press, 1967.

[3] B. Cowan, *Nuclear Magnetic Resonance and Relaxation*. Cambridge University Press, 1997, ISBN: 9780521303931.

[4] I. Rabi, J. Zacharias, S. Millman, and P. Kusch, "A new method of measuring nuclear magnetic moment," *Physical Review*, vol. 53, pp. 318–318, 1938.

[5] F. Bloch, W. Hansen, and M. Packard, "Nuclear induction," *Physical Review*, vol. 69, pp. 127–127, 1946.

[6] F. Bloch, "Nuclear induction," *Physical Review*, vol. 70, pp. 460–474, 1946.

[7] F. Bloch, W. Hansen, and M. Packard, "The nuclear induction experiment," *Physical Review*, vol. 70, pp. 474–485, 1946.

[8] E. Purcell, H. Torrey, and R. Pound, "Resonance absorption by nuclear magnetic moments in a solid," *Physical Review*, vol. 69, pp. 37–38, 1946.

[9] R. Ernst and W. Anderson, "Application of fourier transform spectroscopy to magnetic resonance," *Review of Scientific Instruments*, vol. 37, no. 1, pp. 93–102, 1966.

[10] P. Lauterbur, "Image formation by induced local interactions: Examples employing nuclear magnetic resonance," *Nature*, vol. 242, pp. 190–192, 1973.

[11] P. Lauterbur and P. Grannell, "Nmr 'diffraction' in solids?" *Journal of Physics C: Solid State Physics*, vol. 6, pp. L422–L426, 1973.

[12] G. R. Fowles, *Introduction to Modern Optics*. Dover Publications, Inc., 1989, ISBN: 9780486659572.

[13] D. Hoult, "Zeugmatography: A criticism of the concept of a selective pulse in the presence of a field gradient," *Journal of Magnetic Resonance*, vol. 26, pp. 165–167, 1977.

[14] J. D. Jackson, *Classical Electrodynamics*. John Wiley & Sons, Inc., 1999, ISBN: 9780471309321.

[15] H. Goldstein, C. Poole, and J. Safko, *Classical Mechanics*. Pearson Education, Inc., 2002, ISBN: 9780201657029.

[16] J. Pauly, P. L. Roux, D. Nishimura, and A. Macovski, "Parameter relations for the shinnar-le roux selective excitation pulse design algorithm," *IEEE Transactions on Medical Imaging*, vol. 10, no. 1, pp. 53–65, 1991.

[17] M. Shinnar, L. Bolinger, and J. Leigh, "The use of finite impulse response filters in pulse design," *Magnetic Resonance in Medicine*, vol. 12, pp. 81–87, 1989.

[18] M. Garwood and L. DelaBarre, "The return of the frequency sweep: Designing adiabatic pulses for contemporary nmr," *Journal of Magnetic Resonance*, vol. 153, pp. 155–177, 2001.

[19] M. Silver, R. Joseph, and D. Hoult, "Highly selective $\pi/2$ and π pulse generation," *Journal of Magnetic Resonance*, vol. 59, pp. 347–351, 1984.

[20] A. Tannús and M. Garwood, "Adiabatic pulses," *NMR in Biomedicine*, vol. 10, no. 8, pp. 423–434, 1997.

[21] J. Pauly, D. Nishimura, and A. Macovski, "A k-space analysis of small-tip-angle excitation," *Journal of Magnetic Resonance*, vol. 81, pp. 43–56, 1989.

[22] P. Roemer, W. Edelstein, C. Haues, S. Souza, and O. Mueller, "The nmr phased array," *Magnetic Resonance in Medicine*, vol. 16, pp. 192–224, 1990.

[23] L. Axel, J. Costantini, and J. Listerud, "Intensity correction in surface-coil mr imaging," *American Journal of Roentgenology*, vol. 148, pp. 418–420, 1987.

[24] P. Narayana, W. Brey, M. Kulkarni, and C. Sievenpiper, "Compensation for surface coil sensitivity variation in magnetic resonance imaging," *Magnetic Resonance Imaging*, vol. 6, pp. 271–274, 1988.

[25] M. Griswold, P. Jakob, R. Heidemann, M. Nittka, V. Jellus, J. Wang, B. Kiefer, and A. Haase, "Generalized autocalibrating partially parallel acquisitions (grappa)," *Magnetic Resonance in Medicine*, vol. 47, pp. 1202–1210, 2002.

[26] K. Pruessman, M. Weiger, M. Scheidegger, and P. Boesiger, "Sense: Sensitivity encoding for fast mri," *Magnetic Resonance in Medicine*, vol. 42, pp. 952–962, 1999.

[27] W. Press, S. Teukolsky, W. Vetteringly, and B. Flannery, *Numerical Recipes: The Art of Scientific Computing*. Cambridge University Press, 2007, ISBN: 9780521880688.

[28] J. Jackson, C. Meyer, D. Nishimura, and A. Macovski, "Selection of a convolution function for fourier inversion using gridding," *IEEE Transactions on Medical Imaging*, vol. 10, no. 3, pp. 473–478, 1991.

[29] J. Zhang, R. Chamberlain, M. Etheridge, D. Idiyatullin, C. Corum, J. Bischof, and M. Garwood, "Quantifying iron-oxide nanoparticles at high concentration based on longitudinal relaxation using a three-dimensional swift look-locker sequence," *Magnetic Resonance in Medicine*, vol. 71, no. 6, pp. 1982–1988, 2014.

[30] L. Hanson, "Is quantum mechanics necessary for understanding magnetic resonance," *Concepts in Magnetic Resonance Part A*, vol. 32A, no. 5, pp. 329–340, 2008.

[31] R. Shankar, *Principles of Quantum Mechanics*. Plenum Press, 1994, ISBN: 9780306447907.

[32] R. Feynman, F. Vernon, and R. Hellwarth, "Geometrical representation of the schrödinger equation for solving maser problems," *Journal of Applied Physics*, vol. 28, no. 1, pp. 49–52, 1957.

[33] M. Mullen, N. Kobayashi, and M. Garwood, "Two-dimensional frequency-swept pulse with resilience to both b1 and b0 inhomogeneity," *Journal of Magnetic Resonance*, vol. 299, pp. 93–100, 2019. DOI: 10.1016/j.jmr.2018.12.017.

[34] M. Mullen, N. Kobayashi, and M. Garwood, "Corrigendum to 'two-dimensional frequency-swept pulse with resilience to both b1 and b0 inhomogeneity' j. magn. reson. 299 (2019) 93-100," *Journal of Magnetic Resonance*, vol. 305, p. 93, 2019. DOI: 10.1016/j.jmr.2019.06.007.

[35] J. Pauly, D. Nishimura, and A. Macovski, "A linear class of large-tip-angle selective excitation pulses," *Journal of Magnetic Resonance*, vol. 82, no. 3, pp. 571–587, 1989.

[36] S. Conolly, J. Pauly, D. Nishimura, and A. Macovski, "Two-dimensional selective adiabatic pulses," *Magnetic Resonance in Medicine*, vol. 24, pp. 302–313, 1992.

[37] J. Dumez and L. Frydman, "Multidimensional excitation pulses based on spatiotemporal encoding concepts," *Journal of Magnetic Resonance*, vol. 226, pp. 22–34, 2013.

[38] M. Stehling, R. Turner, and P. Mansfield, "Echo-planar imaging: Magnetic resonance imaging in a fraction of a second," *Science*, vol. 254, no. 5028, pp. 48–50, 1991.

[39] A. Jang, N. Kobayashi, S. Moeller, J. Vaughan, J. Zhang, and M. Garwood, "2d pulses using spatially dependent frequency sweeping," *Magnetic Resonance in Medicine*, vol. 76, pp. 1364–1374, 2016.

[40] J. Dunant and J. D. U. P. 3975765, 1976.

[41] T. Holy. (2010). Generate maximally perceptually-distinct colors, [Online]. Available: https://www.mathworks.com/matlabcentral/fileexchange/29702-generate-maximally-perceptually-distinct-colors?s_tid=FX_rc1_behav. (accessed: 10.09.2018).

[42] M. Garwood, T. Schleich, M. Bendall, and D. Pegg, "Improved fourier series windows for localization in in vivo nmr spectroscopy," *Journal of Magnetic Resonance*, vol. 65, pp. 510–515, 1985.

[43] M. Mullen, "Matlab script to generate gradient and radiofrequency waveforms for a segmented 2d hs1 pulse," in. Mendeley Data, v1 http://dx.doi.org/10.17632/46DJ6BCVD4.1.

[44] S. Vannesjo, M. Haeberlin, L. Kasper, M. Pavan, B. Wilm, C. Barmet, and K. Pruessmann, "Gradient system characterization by impulse response measurements with a dynamic field camera," *Magnetic Resonance in Medicine*, vol. 69, pp. 583–593, 2013.

[45] M. Stich, T. Wech, A. Slawig, R. Ringler, A. Dewdney, A. Greiser, G. Ruyters, T. Bley, and H. Köstler, "Gradient waveform pre-emphasis based on the gradient system transfer function," *Magnetic Resonance in Medicine*, pp. 1–12, 2018.

[46] J. Duyn, Y. Yang, J. Frank, and J. van der Veen, "Simple correction method for k-space trajectory deviations in mri," *Journal of Magnetic Resonance*, vol. 132, no. 1, pp. 150–153, 1998.

[47] E. Insko and L. Bolinger, "Mapping of the radiofrequency field," *Journal of Magnetic Resonance*, vol. Series A 103, pp. 82–85, 1993.

[48] L. Panych and K. Oshio, "Selection of high-definition 2d virtual profiles with multiple rf pulse excitations along interleaved echo-planar k-space trajectories," *Magnetic Resonance in Medicine*, vol. 41, pp. 224–229, 1999.

[49] V. Stenger, F. Boada, and D. Noll, "Multishot 3d slice-select tailored rf pulses for mri," *Magnetic Resonance in Medicine*, vol. 48, pp. 157–165, 2002.

[50] C. Hardy and P. Bottomley, "31p spectroscopic localization using pinwheel nmr excitation pulses," *Magnetic Resonance in Medicine*, vol. 17, pp. 315–327, 1991.

[51] Z. Zhang, M. Lustig, and L. Frydman, "Phase-encoded xspen: A novel high-resolution volumetric alternative to rare mri," *Magnetic Resonance in Medicine*, vol. 80, pp. 1492–1506, 2018.

[52] Z. Zhang and L. Frydman, "Partial fourier techniques in single-shot cross-term spatiotemporal encoded mri," *Magnetic Resonance in Medicine*, vol. 79, pp. 1506–1514, 2018.

[53] U. Katscher, P. Börnert, C. Leussler, and J. V. den Brink, "Transmit sense," *Magnetic Resonance in Medicine*, vol. 49, pp. 144–150, 2003.

[54] Y. Zhu, "Parallel excitation with an array of transmit coils," *Magnetic Resonance in Medicine*, vol. 51, pp. 775–784, 2004.

[55] M. Mullen, A. Gutierrez, N. Kobayashi, J. Haupt, and M. Garwood, "Accelerated imaging with segmented 2d pulses using parallel imaging and virtual coils," *Journal of Magnetic Resonance*, vol. 305, pp. 185–194, 2019. DOI: 10.1016/j.jmr.2019.07.001.

[56] D. Norris, P. Koopmans, R. Boyacioglu, and M. Barth, "Power independent of number of slices (pins) radiofrequency pulses for low-power simultaneous multislice excitation," *Magnetic Resonance in Medicine*, vol. 66, pp. 1234–1240, 2011.

[57] Q. Qin, J. Gore, M. Does, M. Avison, and R. D. Graaf, "2d arbitrary shape-selective excitation summed spectroscopy (assess)," *Magnetic Resonance in Medicine*, vol. 58, pp. 19–26, 2007.

[58] W. Weber-fahr, M. Busch, and J. Finsterbusch, "Short-echo-time magnetic resonance spectroscopy of single voxel with arbitrary shape in the living human brain using segmented two-dimensional selective radiofrequency excitations based on a blipped-planar trajectory," *Magnetic Resonance Imaging*, vol. 27, no. 5, pp. 664–671, 2009.

[59] J. Schneider, R. Kalayciyan, M. Haas, S. Hermann, W. Ruhm, J. Hennig, and P. Ulmann, "Inner-volume imaging in vivo using three-dimensional parallel spatially selective excitation," *Magnetic Resonance in Medicine*, vol. 69, pp. 1367–1378, 2013.

[60] N. Korn, J. Kurhanewicz, S. Banerjee, O. Starobinets, E. Saritas, and S. Noworolski, "Reduced-fov excitation decreases susceptibility artifact in diffusion-weighted mri with endorectal coil for prostate cancer detection," *Magnetic Resonance Imaging*, vol. 33, pp. 56–62, 2015.

[61] M. Blaimer, M. Gutberlet, P. Kellman, F. Breuer, H. Kostler, and M. Griswold, "Virtual coil concept for improved parallel mri employing conjugate symmetric signals," *Magnetic Resonance in Medicine*, vol. 61, pp. 93–102, 2009.

[62] S. Orzada, S. Maderwald, B. Poser, A. Bitz, H. Quick, and M. Ladd, "Rf excitation using time interleaved acquisition of modes (tiamo) to address b1 inhomo-

geneity in high-field mri," *Magnetic Resonance in Medicine*, vol. 64, pp. 327–333, 2010.

[63] P. Robson, A. Grant, A. Madhuranthakam, R. Lattanzi, D. Sodickson, and C. McKenzie, "Comprehensive quantification of signal-to-noise ratio and g-factor for image-based and k-space-based parallel imaging reconstructions," *Magnetic Resonance in Medicine*, vol. 60, pp. 895–907, 2004.

[64] B. Hargreaves, C. Cunningham, D. Nishimura, and S. Conolly, "Variable-rate selective excitation for rapid mri sequences," *Magnetic Resonance in Medicine*, vol. 52, pp. 590–597, 2004.

[65] P. Kellman and E. McVeigh, "Image reconstruction in snr units: A general method for snr measurement," *Magnetic Resonance in Medicine*, vol. 54, pp. 1439–1447, 2004.

[66] F. Breuer, S. Kannengiesser, M. Blaimer, N. Seiberlich, P. Jakob, and M. Griswold, "General formulation for quantitative g-factor calculation in grappa reconstructions," *Magnetic Resonance in Medicine*, vol. 62, pp. 739–746, 2009.

[67] A. Jang, X. Wu, E. Auerbach, and M. Garwood, "Designing 3d selective adiabatic radiofrequency pulses with single and parallel transmission," *Magnetic Resonance in Medicine*, vol. 79, pp. 701–710, 2018.

[68] W. Grissom, C. Yip, Z. Zhang, V. Stenger, J. Fessler, and D. Noll, "Spatial domain method for the design of rf pulses in multicoil parallel excitation," *Magnetic Resonance in Medicine*, vol. 56, pp. 620–629, 2006.

[69] F. Lin, K. Kwong, J. Belliveau, and L. Wald, "Parallel imaging reconstruction using automatic regularization," *Magnetic Resonance in Medicine*, vol. 51, pp. 559–567, 2004.

[70] M. Mullen, "Accelerated imaging with segmented 2d pulses using parallel imaging and virtual coils," in. Mendeley Data, v1 http://dx.doi.org/10.17632/nr57j2fwcy.1.

[71] A. MacKay, K. Whittall, J. Adler, D. Li, D. Paty, and D. Graeb, "In vivo visualization of myelin water in brain by magnetic resonance," *Magnetic Resonance in Medicine*, vol. 34, pp. 673–677, 1994.

[72] J. Choi and G. Gold, "Mr imaging of articular cartilage physiology," *Magnetic Resonance Imaging Clinics of North America*, vol. 19, no. 2, pp. 249–282, 2011.

[73] F. Mitsumori, H. Watanabe, N. Takaya, and M. Garwood, "Apparent transverse relaxation rate in human brain varies linearly with tissue iron concentration at 4.7t," *Magnetic Resonance in Medicine*, vol. 58, pp. 1054–1060, 2007.

[74] F. Mitsumori, H. Watanabe, and N. Takaya, "Estimation of brain iron concentration in vivo using a linear relationship between regional iron and apparent transverse relaxation rate of the tissue water at 4.7t," *Magnetic Resonance in Medicine*, vol. 62, pp. 1326–1330, 2009.

[75] H. Ring, J. Zhang, N. Klein, L. Eberly, C. Haynes, and M. Garwood, "Establishing the overlap of ionp quantification with echo and echoless mr relaxation mapping," *Magnetic Resonance in Medicine*, vol. 79, pp. 1420–1428, 2018.

[76] D. Kunz, "Use of frequency-modulated radiofrequency pulses in mr imaging experiments," *Magnetic Resonance in Medicine*, vol. 3, pp. 377–384, 1986.

[77] D. Kunz, "Frequency-modulated radiofrequency pulses in spin-echo and stimulated-echo experiments," *Magnetic Resonance in Medicine*, vol. 4, pp. 129–136, 1987.

[78] J. Park and M. Garwood, "Spin-echo mri using pi/2 and pi hyperbolic secant pulses," *Magnetic Resonance in Medicine*, vol. 61, pp. 175–187, 2009.

[79] D. Youla and H. Webb, "Image restoration by the method of convex projections: Part 1 - theory," *IEEE Transactions on medical imaging*, vol. MI-1, no. 2, pp. 81–94, 1982.

[80] M. Sezan and H. Stark, "Image restoration by the method of convex projections: Part 2 - applications and numerical results," *IEEE Transactions on medical imaging*, vol. MI-1, no. 2, pp. 95–101, 1982.

[81] E. Haacke, Z. Liang, and F. Boada, "Image reconstruction using projection onto convex sets, model constraints, and linear prediction theory for the removal of phase, motion, and gibbs artifacts in magnetic resonance and ultrasound imaging.," *Optical Engineering*, vol. 29, no. 5, pp. 555–566, 1990.

[82] P. . Jezzard, S. Duewell, and S. Balaban, "Mr relaxation times in human brain: Measurement at 4t," *Radiology*, vol. 1999, pp. 773–779, 1996.

[83] F. Petzschner, I. Ponce, M. Blaimer, P. Jakob, and F. Breuer, "Fast mr parameter mapping using k- t principal component analysis," *Magnetic Resonance in Medicine*, vol. 66, pp. 706–716, 2011.

[84] C. Huang, C. Graff, E. Clarkson, A. Bilgin, and M. Altbach, "T2 mapping from highly undersampled data by reconstruction of principal component coefficient maps using compressed sensing," *Magnetic Resonance in Medicine*, vol. 67, pp. 1355–1366, 2012.

[85] T. Zhang, J. Pauly, and I. Levesque, "Accelerating parameter mapping with a locally low rank constraint," *Magnetic Resonance in Medicine*, vol. 73, pp. 655–661, 2015.

[86] C. Epstein and J. Magland, "A novel technique for imaging with inhomogeneous fields," *Journal of Magnetic Resonance*, vol. 183, pp. 183–192, 2006.

[87] K. Ugurbil, M. Garwood, J. Ellermann, K. Hendrich, R. Hinke, X. Hu, S. Kim, R. Menon, H. Merkle, S. Ogawa, and R. Salmi, "Imaging at high magnetic fields: Initial experiences at 4 t," *Magnetic Resonance Quarterly*, vol. 9, no. 4, pp. 259–277, 1993.

[88] A. Snyder, C. Corum, S. Moeller, N. Powell, and M. Garwood, "Mri by steering resonance through space," *Magnetic Resonance in Medicine*, vol. 72, pp. 49–58, 2014.

[89] R. Chamberlain, J. Park, C. Corum, E. Yacoub, K. Ugurbil, C. J. Jr, and M. Garwood, "Raser: A new ultrafast magnetic resonance imaging method," *Magnetic Resonance in Medicine*, vol. 58, pp. 794–799, 2007.

[90] Y. Shrot and L. Frydman, "Spatially encoded nmr and the acquisition of 2d magnetic resonance images within a single scan," *Journal of Magnetic Resonance*, vol. 172, pp. 179–190, 2005.

[91] A. Tal and L. Frydman, "Spatial encoding and the single-scan acquisition of high definition mr images in inhomogeneous fields," *Journal of Magnetic Resonance*, vol. 181, pp. 179–194, 2006.

[92] J. Pipe, "Spatial encoding and reconstruction in mri with quadratic phase profiles," *Magnetic Resonance in Medicine*, vol. 33, pp. 24–33, 1995.

[93] P. Shkarin and R. Spencer, "Time domain simulation of fourier imaging by summation of isochromats," *International Journal of Imaging Systems and Technology*, vol. 8, pp. 419–426, 1997.

[94] A. Chambolle, "An algorithm for total variation minimization and applications," *Journal of Mathematical Imaging and Vision*, vol. 20, pp. 89–97, 2004.

[95] J. Fessler and W. Rogers, "Spatial resolution properties of penalized-likelihood image reconstruction: Space-invariant tomographs," *IEEE Transactions on Image Processing*, vol. 5, no. 9, pp. 1346–1358, 1996.

[96] A. Beck and M. Teboulle, "A fast iterative shrinkage-thresholding algorithm for linear inverse problems," *Society for Industrial and Applied Mathematics Journal on Imaging Sciences*, vol. 2, no. 1, pp. 183–202, 2009.

[97] A. Beck and M. Teboulle, "Fast gradient-based algorithms for constrained total variation image denoising and deblurring problems," *IEEE Transactions on Image Processing*, vol. 18, no. 11, pp. 2419–2434, 2009.

[98] A. Gutierrez, D. Xiao, J. Haupt, A. Jang, S. Moeller, and M. Garwood, "Accelerated regulzerized image reconstruction in spatiotemporal mri," in *Proc. Intl. Soc. Mag. Reson. Med. 25*, (Honolulu, Hawaii), Apr. 2017, p. 1514.

[99] G. Bodenhausen, R. Freeman, and D. Turner, "Suppression of artifacts in two-dimensional j spectroscopy," *Journal of Magnetic Resonance*, vol. 27, pp. 511–514, 1977.